Elucidating Environment-Assisted Cracking of Engineered Duplex Stainless Steel Weld Microstructures

_____

A thesis submitted to the University of Manchester for the degree of Doctor of Philosophy in the Faculty of Science and Engineering

2019

Pierfranco Reccagni

School of Materials

LIST OF CONTENTS

Words count 38114

LIST OF FIGURES

LIST OF TABLES

ABBREVIATIONS AND SYMBOLS

AR	As Rececived
BCC	Body Centred Cubic
BSE	BackScattered Electrons
CA	Coarse Austenite
DSSs	Duplex Stainless Steels
EAC	Environment-Assisted Cracking
EDX,EDS	Energy-Dispersive X-Ray Spectroscopy
Ev	Electron Volt
FCC	Face Centred Cubic
FEG	Field Emission Gun
FSD	ForeScatterd Electrons
GBA	Grain Boundary Austenite
HAC	Hydrogen Assisted Cracking
HE	Hydrogen Embrittlement
HI	Heat Input
IGA	InterGranular Austenite
K-S	Kurdjumov-Sachs
PREN	Pitting Resistance Equivalent Number
PTD	Potentiodynamic
SD	Standard Deviation
SE	Secondary Electrons
SEM	Scanning Electron Microscope
SKPFM	Scanning Kelvin Probe Force Microscopy

TIG	Tungsten Inert Gas
ψ	Volta-Potential
γ	Austenite
δ	Ferrite
σ	Sigma phase
χ	Chi phase
ε	Hexagonal martensite

ABSTRACT

Environment assisted cracking (EAC) is the name used to describe a group of degradation mechanisms that cause failure of materials in service as a combined result of corrosive environment, mechanical stress and susceptible microstructure. Duplex stainless steels (DSSs) have outstanding EAC resistance, provided by the different mechanical, electrochemical and hydrogen diffusivity properties of the two phases. The optimal microstructure morphology, can be altered in the heat affected zones (HAZs) of welded components, with this region of the weldment offering lower EAC resistance.

This work presents a detailed observation on the effects of arc-welding on the austenite morphology in the HAZ of a multi-pass DSS2205 TIG weld and in thermo-mechanically simulated HAZs. Austenite morphological changes, formation of precipitates and internal galvanic activity in the simulated alloys have been evaluated using a combination of microstructure characterization techniques, scanning kelvin probe microscopy (SKPFM) potential surveys and electrochemical measurements. The relevance of these observations has been validated performing EAC testing on a real-scale multi-pass tungsten inert gas (TIG) weld.

The results showed a marked reduction in internal galvanic activity in the simulated HAZs, offering an electrochemical explanation for the enhanced SCC susceptibility of this region. Different degrees of hydrogen embrittlement resistance for different austenite morphologies were observed, with grain boundary austenite (GBA) showing the lowest resistance to crack progression. Austenite morphology showed an effect also on the anodic dissolution of ferrite - a precursor of SCC attacks – and a qualitative relationship between phase boundaries orientation, applied stress and preferred cracking paths was devised.

DECLARATION

I declare that no portion of the work referred to in the thesis has been submitted in support of an application for another degree or qualification of this or any other university or other institute of learning.

Pierfranco Reccagni

COPYRIGHT STATEMENT

The author of this thesis (including any appendices and/or schedules to this thesis) owns certain copyright or related rights in it (the "Copyright") and s/he has given The University of Manchester certain rights to use such Copyright, including for administrative purposes. Copies of this thesis, either in full or in extracts and whether in hard or electronic copy, may be made only in accordance with the Copyright, Designs and Patents Act 1988 (as amended) and regulations issued under it or, where appropriate, in accordance with licensing agreements which the University has from time to time. This page must form part of any such copies made. The ownership of certain Copyright, patents, designs, trademarks and other intellectual property (the "Intellectual Property") and any reproductions of copyright works in the thesis, for example graphs and tables ("Reproductions"), which may be described in this thesis, may not be owned by the author and may be owned by third parties. Such Intellectual Property and Reproductions cannot and must not be made available for use without the prior written permission of the owner(s) of the relevant Intellectual Property and/or Reproductions. Further information on the conditions under which disclosure, publication and commercialisation of this thesis, the Copyright and any Intellectual Property and/or Reproductions described in it may take place is available in the University IP Policy (see http://documents.manchester.ac.uk/DocuInfo.aspx?DocID=2442 0), in any relevant Thesis restriction declarations deposited in the University Library, The

University Library's regulations (see http://www.library.manchester.ac.uk/about/regulations/) and in The University's policy on Presentation of Theses

1 INTRODUCTION

Duplex stainless steels (DSSs) have become an increasingly popular choice for applications in the petrochemical industry, duo to their good mechanical properties and corrosion resistance [1–3]. Of particular interest is their outstanding resistance to environment-assisted cracking (EAC), with far superior performance than their austenitic counterparts. The high strength and lower nickel content makes them a preferred alternative in applications where their use is viable.

The corrosion properties of duplex alloys depend largely on their microstructure. Most forms of corrosion would affect differently the individual constituent phases, with the global corrosion behaviour of the alloy being the complex results of the phases interaction.

The weldability of modern duplex grade has largely improved with respect to the early stages of development [4]. However, the heat affected zone of the welds still proves to have lower resistance to stress corrosion cracking and hydrogen embrittlement. Active standards [5] define the requirements for avoidance of undesired tertiary phases and intermetallic precipitates, without providing directions on the qualification of the austenite and ferrite morphology in the heat affected zone (HAZ).

The objective of the project is to develop microstructure descriptors for the characterization of local corrosion and environment-assisted cracking behaviour of welded duplex stainless steel microstructure. The project addresses a knowledge gap in understanding the design and manufacture of microstructure-optimized duplex stainless steel welds.

Through the use of thermo-mechanical simulated microstructures and actual multi-pass tungsten inert gas (TIG) welds, fundamental properties of the HAZ is characterized and their relevance in stress corrosion cracking (SCC) and hydrogen embrittlement (HE) is tested using multiple testing methods.

1.1 AIMS AND OBJECTIVES

The main aim of this project is the development of a correlation between welding parameters, microstructure morphology in the corresponding heat affected zone and susceptibility to environment assisted cracking. In other words, this project provides a "big picture" of the interaction between welding heat input, microstructure morphology and EAC resistance.

The first objective of this work is to find microstructural descriptors of the HAZ morphology directly related to the heat input (HI) used during welding. The effects of the welding heat input on the microstructure morphology of the heat affected zone are studied on thermo-mechanically simulated microstructures. Electrochemical properties of the HAZ are also studied on these microstructure.

Secondly, the relationship between the descriptors found and their role in EAC resistance is studied on a real-scale multi-pass weld. The main corrosion mechanisms of interest are hydrogen embrittlement and atmospheric-induced stress corrosion cracking. These areinvestigated using accelerated corrosion testing and high resolution characterization techniques.

1.2 STRUCTURE OF THE THESIS

The thesis is proposed in the manuscript-based format. The experimental work carried out and the most relevant results are presented in the form of four manuscripts prepared for peer-reviewed journal publication. In details:

Chapter 2 includes a literature review aimed to serve as background introduction to the metallurgy and corrosion science topics discussed in the manuscripts. Further literature is included in the introduction of each manuscript.

Chapter 3 presents briefly the techniques used in the experimental works, with more details of less conventional techniques.

Chapter 4 consists of an in introduction to the materials produced for the project (4.1) and of four manuscripts where the experimental work and results of the research activity are presented.

Manuscript 1 – This manuscript form the basis for the description of the HAZ microstructure morphology and its relationship with the heat input used in arc welding. The microstructure evolution at different cooling times is described in this manuscript, where also the formation of precipitates and tertiary phases, with their effects on corrosion behaviour of the HAZ, is discussed.

Manuscript 2 – In this manuscript, electrochemical properties of the HAZ are studied on a simulated microstructure. This work contributes in explaining the reduced SCC resistance of this region of the weld by showing the partial loss of galvanic protection between austenite and ferrite after exposure to welding thermal cycles.

Manuscript 3 – The hydrogen embrittlement resistance of the microstructure morphologies defined in manuscript 1 is investigated on the real scale multipass weld manufactured at the beginning of the project (chapter 4.1). A quasi in-situ approach and a pre-/post- mortem crystallographic characterization of embrittled weld samples are

proposed in this manuscript. Hydrogen-induced surface damage are also discussed, with the early stages of their formation presented separately in Annex 5.1.

Manuscript 4 – This manuscript investigates the morphology of atmospheric-induced corrosion attacks on samples of the reference weld (described in chapter 4.1) exposed to salt-laden deposits in controlled humidity environment. The purpose of this chapter is to highlight the influence of strain direction and austenite distribution on the morphology of ferrite selective attacks.

2 LITERATURE REVIEW

This chapter contains a theoretical background of the main areas of interest touched in the project. The literature proposed serves as an introduction to the topics developed in the manuscripts and presents basic principles of the metallurgical and electrochemical properties investigated.

Section 2.1 introduces stainless steels, with a particular focus on duplex stainless steel metallurgy and microstructure evolution of DSS weldments.

Section 2.2 introduces the principles of corrosion and basic corrosion mechanisms, serving as a "dictionary" for the types of corrosion cited throughout the thesis. Section 2.3 extends the discussion to Environment-Assisted Cracking, which is the main area of corrosion science faced in this project. In this section, stress corrosion and hydrogen induced cracking mechanisms are summarized and the general knowledge exposed is then adapted to the specific case of duplex stainless steel alloys.

Section 3 describes the tungsten inert gas welding technique and the use of thermo-mechanical physical simulation to reproduce welding process on a laboratory scale. A review of the most significant works in the duplex weld simulations field is proposed.

2.1 STAINLESS STEELS

The terms "stainless steels" refers to all those iron-based alloys containing chromium among the alloying elements, in weigh fraction not lower than 12-13%[6]. The term stainless describe the corrosion resistance of these alloys, which is granted by the ability of chromium to form a protective chromium (III) oxide passive film when

exposed to oxygen [7][7–9]. With respect to low alloyed steel [8], the corrosion resistance is greatly improved and stainless steels show much lower corrosion rates.

Several alloying elements are found in modern stainless steel grades, but it is in particular the Fe-Cr- Ni ternary system defining the phase composition of the final alloy. The microstructure of an alloy is crucial in defining its mechanical and corrosion properties; through a balance of chemistry and thermo-mechanical treatments, several phases can be generated. According to their microstructure, stainless steels are divided in classes; austenitic and ferritic steels will be briefly described in this paragraph. A separated section will be dedicated to duplex stainless steels (DSSs) and their metallurgical aspects, being the DSS2205 grade the object of this work.

2.1.1   Ferritic Stainless Steels

Pure iron and ferritic stainless steels exhibit body centred cubic (BCC) microstructure, with one Fe atom occupying each corner of the cubic reticule and another atom in the centre. This structure shows ferromagnetic character. Chromium, typically in a 12.5% - 17% weight, is not only important

for the corrosion resistance of these alloys, but it is also the main alloying elements that stabilize the ferritic phase (δ). Other elements with this property are called ferrite stabilizers and theirs stabilizing effects on the ferrite is often expressed as a "chromium equivalent". A representation of the steel phase distribution estimated from the chromium and nickel equivalent content is summarized in the Schaeffler diagram [10][11] -Figure 1. Despite good mechanical properties and moderate corrosion resistance, these grades show limitations in weldability and a propensity to hydrogen embrittlement (HE); details of hydrogen diffusion in bcc phase will be discussed in the hydrogen section.

2.1.2 Austenitic Stainless Steel

Austenitic stainless steel alloys contain Ni (6 to 12 wt.%), Cr (16 to 26 wt.%), Mn, Mo and N as the main alloying elements; their main constituent phase is austenite (γ), which exhibits a face centred cubic reticule (FCC). This structure shows paramagnetic properties. The high nickel content, together with the presence of nitrogen and manganese, extends to lower temperatures the range of existence for austenite, *de facto* suppressing or at least minimizing the austenite to ferrite transformation upon adequate cooling. Austenitic steels have good corrosion resistance and mechanical properties, nonetheless they can suffer from stress corrosion cracking in chloride-rich environments, where localised corrosion attacks –such as pitting corrosion – can act as precursors.
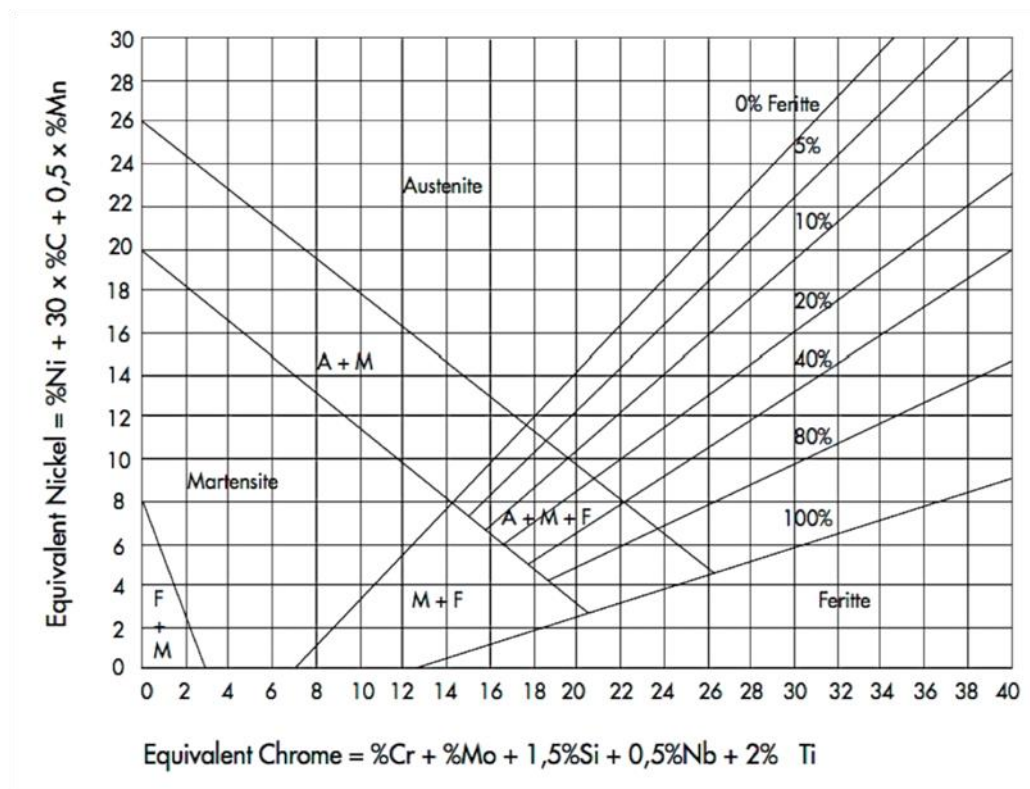
Figure 1 - Schaeffler diagram for phase fraction estimation

2.1.3 Duplex Stainless Steel

Duplex stainless steels are a family of grades characterised by a ferritic-austenitic microstructure, with approximately equal proportion of the two phases [1]. Combining some of the advantages of the austenitic and the ferritic steels, their particular microstructure provides the material with high strength [12,13] and high resistance to stress corrosion cracking (higher than corresponding austenitic steel) [14]. The lower Nickel content, with respect to completely austenitic steels, make them a convenient choice where their use is viable, attracting more interest with the increasing price of Nickel [15]. Duplex steels are generally referred as "super duplex"[3,16,17], when they have a relatively high content of Nickel (up to 7%) or "lean duplex"[18] when the amount of alloying elements is low. The duplex grade studied in this work is the UNS S32205, commonly referred to with his trade name 2205, one of the most widely used grades.

The effects of the single alloying elements on the microstructure and the corrosion resistance will be discussed in this chapter. Thermal treatments and the resulting precipitation of tertiary phases will be also described, together with some general aspects of the corrosion resistance for this class of steels.

2.1.3.1 Chemical Composition and effect of the Alloying Elements

The chemistry of the alloy plays a crucial role in determining the microstructure at the temperature of operation; the composition of the 2205 grade is listed in Table 1. The alloying elements have different effects in stabilising the ferritic or the austenitic phase and, thus, some of them tend to partition [19,20][19–21] in one of the two phases, which result in having different composition from the nominal one.

Chromium enhances the general and localised corrosion resistance by the formation of a chromium oxide/hydroxides rich passive film [22]. The passive range of potential, thus, is extended by its addition. A limitation to the amount of Cr that can be added is caused by its ability to form tertiary/intermetallic phases (σ, Cr_2N, CrN) [23] that have negative influence on the corrosion properties. The weight fraction of Cr in duplex steel is generally in the range 20.1-25.4% [24], with some superduplex grades reaching 29%. During solidification, when austenite precipitates from ferrite, this element tends to partition in the ferrite. Partitioning occurs with many of the alloying elements, even though it is much more evident for Chromium, Molybdenum, Nickel and Nitrogen [20]. Molybdenum has a beneficial effect on the pitting potential and the passive range of the alloy [25]; it is known to contribute in the formation of the oxide layer, with the outer layers of the oxide film particularly enriched with Mo oxides [26].The content of this element is usually limited to 4% because of its ability to promote formation of secondary phases. Mo tends to partition in the ferrite, with a strong raise of its weight fraction in this phase composition.

Table 1 -Standard chemical composition of different duplex stainless steel grades (wt.%)[10]*.*

UNS No.	EN No.	Common Name	C, max	Cr	Ni	Mo	Mn	Si	Co	Cu	N
S31803	1.4462	2205	0.03	21–23	4.5–6.5	2.5–3.5	2.0	1.0	–	–	0.08–0.2
S32205	1.4462	2205	0.03	22–23	4.5–6.5	3.0–3.5	2.0	1.0	–	–	0.14–0.2
S32550	1.4507	255	0.04	24–27	4.5–6.5	2.9–3.9	1.5	1.0	–	1.5–2.5	0.10–0.25
S32950	–	7Mo Plus	0.03	26–29	3.5–5.2	1.0–2.5	2.0	0.6	–	–	0.15–0.35
S32750	1.4410	2507	0.03	24–26	6.0–8.0	3.0–5.0	1.2	0.8	–	0.5	0.24–0.32
S32707	–	SAF 2707HD	0.03	27	6.5	4.8	1.0	0.3	1.0	–	0.4
S33207	–	SAF 3207HD	0.03	32	7	3.5	1.0	0.3	–	–	0.5
S32304	1.4362	2304	0.03	21.5–24.5	3.0–5.5	0.05–0.6	2.50	1.0	–	0.05–0.6	0.05–0.2
S32101	1.4162	LDX 2101	0.04	21–22	1.35–1.7	0.1–0.8	4.0–6.0	1.0	–	0.1–0.8	0.2–0.25

2.1.3.2 Tertiary Phases and Precipitates – Sigma, Chi, Nitrides and 475°C Embrittlement

Secondary phases and precipitates form in DSSs in specific ranges of temperature and show a variety of effects in the properties of the final alloy. They have great relevance on the corrosion resistance and on the mechanical properties of the alloy. During exposure of the alloy in a range of temperatures between 400°C and 950°C, several precipitates can form in the material.

Ferrite (α) can decompose in Sigma (σ), Chi (χ) and Nitrides tertiary phases following a eutectoid reaction (Equation 1) [27]

(Eq 1) $\alpha \rightarrow \sigma + \chi + Cr_2N$
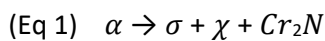
Sigma phase (σ) is nucleated at 700-950 °C [28,29] and exhibits a tetragonal structure with a high content of chromium (30%) and molybdenum (7%). Hard and brittle, it is preferentially nucleated at the ferrite-austenite and ferrite-ferrite boundaries; σ precipitation is also associated with a depletion of Cr and Mo in the adjacent grains [30]. However, the diffusion of Mo to the sigma phase from adjacent ferrite grains is

faster: the diffusion of this element is controlling step in the sigma phase growth. The diffusivity of Cr and Mo in the closed-packed FCC (Face Centred Cubic) structure of the austenite is slower than in the BCC (Body Centred Cubic) structure [23,31]; accordingly, the sigma phase nucleated at the grain boundaries grows inside the adjacent ferritic grains. When the steel is cooling through this range of temperatures, the amount of sigma phase formed depends on the cooling rate. An example of simulated Time-Temperature Transformation and Continuous Cooling Transformation curves for the 2205 grade (22-23 wt.% Cr, 3-3.5 wt.% Mo) for the precipitation of different fractions of σ phase (1, 3, 5 and 10%) is shown in Figure 2 [32].
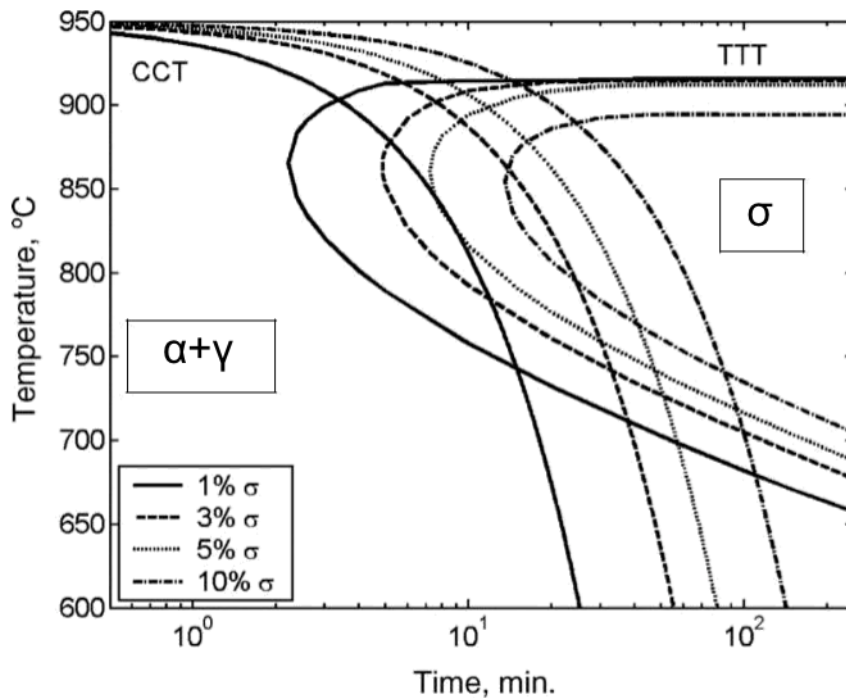
Figure 2 - CCT curves for 1, 3, 5 and 10% σ-phase fraction in DSS2205 steel [32]

Chi phase (χ) [27,28,33,34] exhibits a body centred cubic structure containing about 25% Cr, 3% Ni and 14% Mo ($Fe_{36}Cr_{12}Mo_{10}$ [33]). The Chi-phase forms at the austenite/ferrite interface but, according to its crystallographic structure, a cube-cube orientation relationship ensures the continuity of this phase with the ferrite. Another difference

related to the crystallographic structure between sigma and chi phases, is the higher solubility of Carbon in the latter.

The solubility of nitrogen in ferrite is high only at high temperature (just below the solidus, duplex steels are fully ferritic); during cooling, nitrogen partitions into the austenitic phase, while its solubility in ferrite drops considerably. As a result, the supersaturated ferrite can be exposed to the precipitation of intergranular Cr_2N needle-like nitrides [35,36].

Another transformation that occurs in ferrite, between 350°C and 550°C, is the decomposition of this phase in a Cr enriched phase (α") and a Cr-depleted phase (α'). The miscibility gap in the Fe-Cr system is the cause of the spinoidal [37,38] decomposition of ferrite; the highest rate of decomposition is found at 475 °C. Because of the effect of this decomposition on the mechanical properties of the alloy [38,39],this transformation is called "475 °C embrittlement".

2.1.3.3 Microstructure Development in a Weld

The microstructure of the metal in a weld is different from the one of its parent material, both because of the different thermal history and the different chemical composition of the weld (even when an autogenous weld is performed, nitrogen loss during heating can alter the composition [40]. Similarly to a cast microstructure, solidification starts as epitaxial growth of ferritic grains from the parent material wall, with a dendritic structure whose orientation depends on the thermal gradients in the weld pool [4,41]. Generally, the austenite precipitates between the dendritic ferrite structures by solid-state transformation; however, this process is not homogenous.

In fact, different types of austenite have been reported to form in the solidification of a weld, with intergranular austenite (or grain boundaries austenite, GBA), Widmanstatten

austenite (WA, precipitating also at the ferrite:ferrite grain boundaries [42]) and intragranular austenite (IGA)[43] all commonly found in a multi-pass weld. The precipitation of austenite is a diffusion-controlled mechanism with the cooling rate being the main variable that controls the relative amount of austenite.

The effect of the different austenite types on stress corrosion cracking propensity have been shown by Liou et al. [43] ; the time to failure of U-bend sample in 40% calcium chloride aqueous solution at 100°C has been recorded and the fracture surfaces analysed. Their results showed that the susceptibility of the microstructure towards intergranular SCC was enhanced by the presence of grain boundary austenite, while the replacement of GBA by Widmanstatten Austenite and IGA moved the corrosion mechanism to transgranular SCC. These results suggest that an in-depth understanding of the morphology of the reformed austenite in welds is a crucial step to control and prevent stress corrosion cracking.

An approximate prediction of the austenite:ferrite content in a weld can be made considering the chemical composition of the alloy. The Welding Research Council diagram from 1992 [11]] for example, gives an empirical description of the microstructure resulting from welding alloy with different compositions, improving 1974 DeLong's and 1949 Schaeffler's diagrams. The alloy elements are grouped, according to their partitioning behaviour, in nickel equivalent (elements that promotes the stability of austenite) and in chromium equivalent (conversely, elements that promotes the stability of ferrite). This diagram – see Figure 3- is used in practice to have a first approximation of the austenite fraction that can be expected in a weld; the calculation do not take into account the kinetics of the solidification in a real weld, being based on equilibrium thermodynamics only.
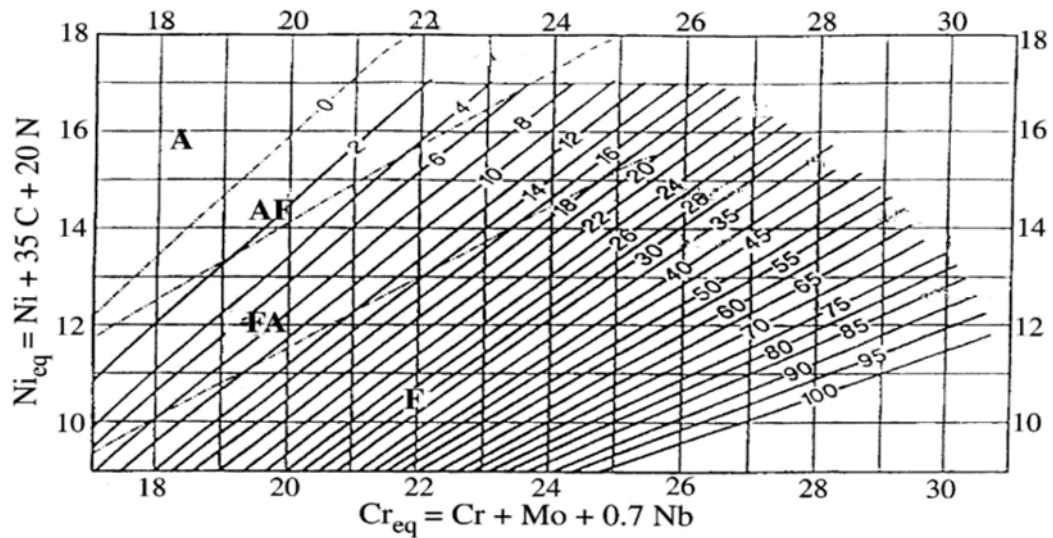
Figure 3 - WRC (Welding Research Council) diagram for phase prediction in duplex stainless steel welding[11]*.*

2.2 CORROSION AND ENVIRONMENT-ASSISTED CRACKING

This section summarizes some of the fundamentals of corrosion science, with a general introduction on the chemistry of the reduction/oxidation reactions involved in all the wet-corrosion mechanisms and a presentation of the localised corrosion types more relevant to this project.

2.2.1 Principles of corrosion and basic mechanisms

Electrochemical corrosion [44] is the name used for all the materials degradation processes that involve a spontaneous oxidation-reduction reaction (redox) causing the conversion of a refined metal, such as iron in steel alloys, into a different chemical compound (often an oxide) with a lower Gibbs free energy (thermodynamic condition). Aqueous or wet corrosion is the field of corrosion science that studies corrosion phenomena produced in aqueous solution. The electrochemical corrosion reactions can be split in two groups, anodic and cathodic. Together with the electrolyte where these reactions occur, this is called an electrochemical cell – see Figure 4.

An anodic reaction in this context is a reaction that occurs on a metal atom and raise its

oxidation state by removing electrons, this can be generalized as:

$M \rightarrow M^{n+} + ne^-$ *(anodic dissolution)*

Conversely, a cathodic reaction is a reaction that consumes electrons reducing the oxidation state of one or more of the reagents involved. Cathodic reactions in water change according to the acidity of the environment:

$2H^+ + 2e^- \rightarrow H_{2(gas)}$ *(hydrogen evolution)* [45]

$O^2 + 4H^+ + 4e^- \rightarrow 2H_2O$ *(oxygen reduction in acidic environment)*

$O^2 + 2H_2O + 4e^- \rightarrow 4 OH^-$ *(oxygen reduction in alkaline environment)*
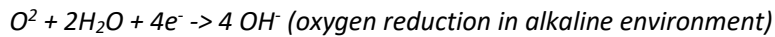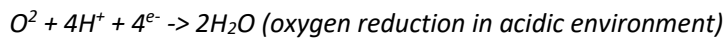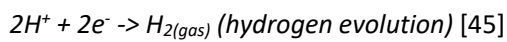
It is worth to recall that a cathodic reaction can be provided not only by water and oxygen, but also by metallic species if the reduction of a metallic cation is possible. Metallic salts dissociated in water, such as $FeCl_3$, may act as oxidising species once dissolved; their cations in this case provide the reduction reaction.

$M^{n+} + e^- \rightarrow M^{(n-1)+}$ *(metal cation reduction)*

$FeCl_{3(s)} \rightarrow Fe^{3+} + 3Cl^-$ *(Ferric Chloride dissociation in water)*
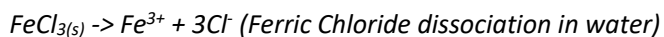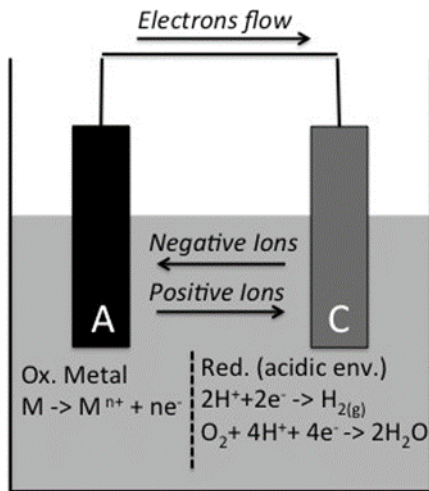
Figure 4 - Sketch of a two electrode electrochemical cell.

For the electrolytic cell to be complete, a conductive media is necessary for the ionic current flow to circulate from the anode to the cathode so that the reduced specie can combine with the oxidised metal. Also, anode and cathode need to be in electrical connection in order to transfer electrons. This condition can be satisfied by having anodic and cathodic regions on the same material or by having an external connection (galvanic coupling).

The corrosion process requires a susceptible material (anodic reaction) and a reactive environment (cathodic reactions). Removing one of the two breaks the cell and stops the corrosion process. Corrosion protection strategies addressed to the anodic reactions work on the availability of the thermodynamic conditions for metal oxidation to occur, either by selecting a material inert in the specific conditions or by conditioning its surface potential via external polarization systems (cathodic protection). Strategies addressing the cathodic reactions work by means of insulation of the active material from the environment (native passive films, coatings) or by removing oxidising species from the environment itself (de-oxygenation, pH control, corrosion inhibitors).

When a material is free to corrode in a specific environment, the anodic dissolution involves the whole surface exposed and is referred to as "generalized corrosion". This term is used to describe those corrosion attacks that produce typically a homogeneous damage.

The anodic current density determines the corrosion rate, and the mass of metal dissolving per unit of time can be easily calculated with the Faraday law .

$$CR = \frac{i\,M}{F\,z\,\rho}$$

where *CR* is the mass loss (in centimetres per second), *i* is the current (in Amperes per squared centimetres), *M* is the molar mass of the metal, *F* is the Faraday constant (96485 Coulomb per mole), *z* is the valency number of the oxidized ion and ρ is the density (in grams per centimetre cube). Due to the meaning of the corrosion rate in real applications, more common units are millimetres or microns per year.

2.2.1.1 Passive films and Evans Diagram

Corrosion resistant alloys, such as stainless steels, rely on the passivation properties of one or more of their alloying elements; these elements have the property to form a passive film that isolates the active metal from the environment. Once the passive film is established, ideally the only contact between oxidizing species and metal can happen by diffusion through the vacancies and defects of the passive film, therefore reducing the corrosion rate of the metal to negligible values. In other words, the passive film intervenes on reducing the kinetics of the corrosion process, making it so slow enough for its effects to be irrelevant in the time scale of the application the material is selected for. However, in practical application, passive films are both prone to defects [9] from processing and susceptible to attack and local degradation from specific chemical species.

Passive films composition is determined by several factors. In modern alloys, the chemical composition of the metallic system determines the types of metal oxides that

can be found in the passive film in first place. Further, condition of the environment such as temperature, pH and presence of halide ions can influence the film composition. The passive film is in constant interaction with the environment and the dynamic equilibrium of passive film dissolution and new film formation is crucial for its protective effects on the bare metal.
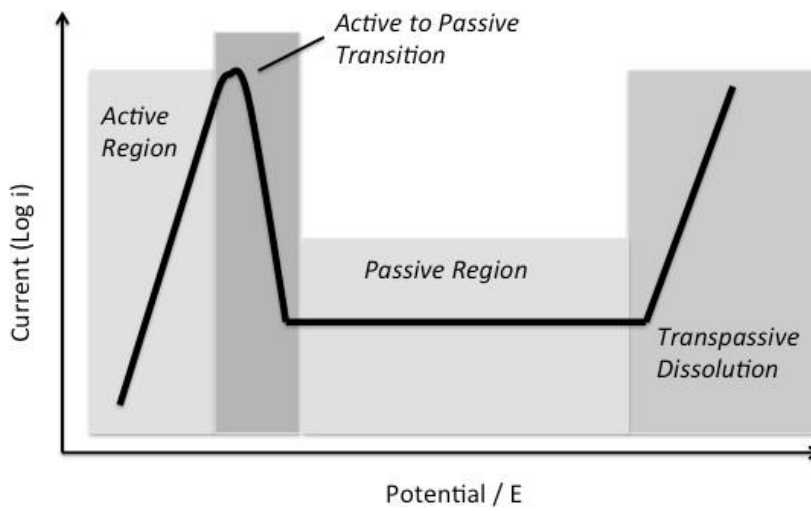
Figure 5 - Evans diagram (Potential vs. current density) for a passive material.

Two different regimes of passive film growth can be identified. An initial passive film readily forms on the bare metal surface upon exposure of the metal to the oxidizing environment. Once the film reaches sufficient coverage and thickness to insulate the bare metal from the environment, the growth rate of the film is limited by either ions diffusion through vacancies and defects in the passive film or by charge transfer through the film. In this second regime, the film growth can happen either at the metal/oxide or the oxide/environment interface. For the film to be protective, the dissolution of the film in the environment needs to be readily compensated by further passive film growth. The passive region in the Evans diagram identifies this balance, with the small anodic current in this region being the current used to sustain the passive film.

The corrosion behaviour for materials forming a passive film can be divided in distinct regions. An example of the anodic part of the Evans diagram (potential vs. logarithm of the corrosion current) is shown in. The effects of the passive film can be see Figure 5 at the active to passive transition potential (passivation potential), when the passive film forms and the corrosion current therefore drops of several orders of magnitude. The established passive film is stable in a range of potential called passive region before the condition for the breakdown of the passive film is reached and the protective oxide layer deteriorates, leaving the metal exposed to the environment and free to corrode.

This representation does not keep into account for localised ruptures of the passive film, which can occur at potentials lower than the breakdown potential when particularly aggressive ions are in contact with the surface. In particular, chloride ions are particularly detrimental for chromium (III) oxide passive films and their effects have been reported and studied for decades now, despite the mechanism of the chlorides attack on the passive film is not completely explained.

2.2.1.2 Localised Corrosion

Passive metals are far from immune from corrosion attacks. In fact, despite the passive film can assure protection against general corrosion (or, more accurately, reduce its kinetics to acceptable levels), some corrosion forms can attack the passive film locally and produce substantial damage to the entire material. Because of their nature, involving initial damages on a small scale, localised corrosion attacks can be difficult to spot and to mitigate at early stages. The local rupture of the passive film is normally the initial step of any localised corrosion attack. This rupture can be facilitated by features of the microstructure - such as metallic inclusions and precipitates – or from

design flaws – such as crevices in assemblies. In the following paragraphs, some of the most relevant localised corrosion forms are introduced.

2.2.1.2.1 Pitting Corrosion

Pitting corrosion is the name used for an extremely localised corrosion attack that after local depassivation produces a small anodic area of active metal couples with the rest of the material that, being still protected from the passive film, act as a cathodic surface. The result of this galvanic coupling is an autocatalytic process that leads to the formation of small holes in the metal (pits), growing in depth – see Figure 6. The environment inside a pit undergoes modifications that make the attack progressively more aggressive. In particular, the reaction of the oxidised metallic ions with the environment produces a strong increase in acidity, as a result of a chemical reaction called 'metal ion hydrolysis'[46]. Further, the local excess of positive charge in the pit volume tends to attract negative charged ions to maintain the electrical neutrality, such as Cl^-. Another aspect of the pit environment, which makes the attack particularly aggressive, is the progressive depletion of oxygen whose diffusion is impaired by the pit geometry itself which limits the convection; the depletion of reducing species inside the pit and the progressively more acidification make the attack able to progress to considerable depths.
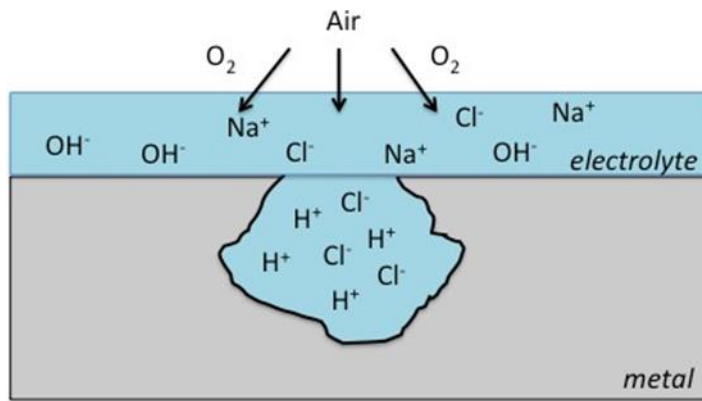
Figure 6 - Environment change within a pit.

The pits growth is facilitated in depth by the locally more aggressive environment, while the hole on the surface may remain relatively small and therefore difficult to identify; similarly, the weight loss due to pitting is generally moderate, because of the small volume interested.

The pitting potential (EP) is the lower value of potential for which a stable pit can form. At lower potentials, pits are metastable and passive film breakdown and repairs are equally possible. At lower potentials, pitting corrosion cannot occur. In order to stop a pitting attack once initiated, the material need to be polarized at the repassivation potential (ERP). This value of potential can be individuated with cyclic voltammetry, following the hysteresis cycle that bring the metal back into the passive region.

2.2.1.2.2 Crevice Corrosion

Crevice corrosion is the name given to all those corrosion attacks that occurs in a narrow gap between two adjacent surfaces (sketch in Figure 7), irrespective of whether they are both metallic or just one of the two is. In fact, crevice attacks on a metal surface can be found also under deposits, damaged coatings or plastic parts. The evolution of the environment within a crevice follows similar route as the development of the environment within a pit. The biggest difference is that the geometry for local deterioration of the environment is already provided [47]; therefore the initiation of a crevice attack is

facilitated and for this reason, the potential for crevice corrosion is always lower than the pitting potential for the same conditions.
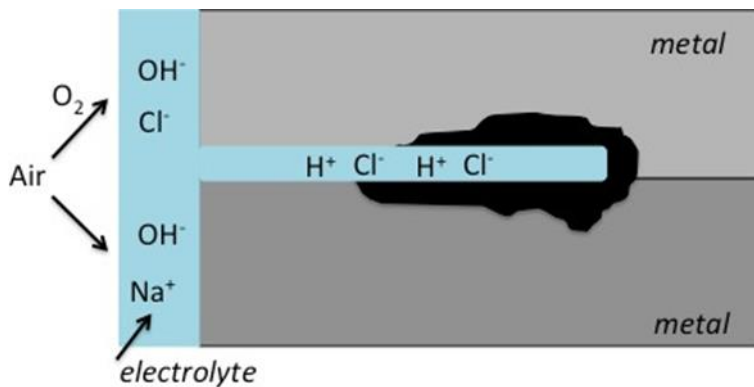
Figure 7 - Crevice geometry and local environment

2.2.1.2.3   Galvanic Coupling

On a metal in free corrosion regime, anodic and cathodic regions are distributed on the surface, with the corrosion rate dependent from the combination of material and environment. This balance can be altered when the material is put in connection with a dissimilar alloy with higher or lower nobility in the same environment. In particular, the cathodic reactions concentrate on the more noble material while the anodic reactions on the less noble. The difference in electrochemical potential between the two metals determines the properties of the galvanic couple – see Figure 8.
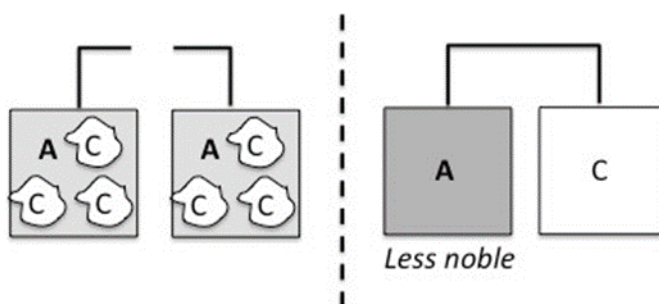
Figure 8 - formation of net anodes and cathods in a galvanic couple.

Particularly detrimental is the couple between a small anode and a large cathode (a good example can be a large structure of some corrosion resistant alloy assembled using less

resistant metallic nuts and bolts). In this case, the balance of cathodic and anodic reaction causes a concentrated and therefore deep attack on the anodic spots, while the entire surface act as a net cathode. The corrosion current is, in fact, proportional to the ratio between cathodic and anodic areas. It is worth to mention that this corrosion mechanism can be also used as a protection system. Cathodic protection of a structure can be achieved by electrical connection with a less noble material, which will behave as a sacrificial anode preventing corrosion attacks on the cathode.

2.2.1.2.4 Intergranular Corrosion and Sensitization

Corrosion attacks that interest the grain boundaries of the metal grains are described as intergranular corrosion. Corrosion at the grain boundaries is often the result of compounds precipitation at the grain boundaries and local depletion of the chemical species involved in the precipitation from the surrounding matrix [48,49].

A frequent case of intergranular corrosion is the precipitation of chromium carbides at the grain boundaries in stainless steels and it is referred to as sensitisation. The affinity of chromium for carbon can lead, especially during welding or other thermal treatments, to the formation of chromium carbides. The alloy surrounding the precipitates is therefore depleted in chromium (see diagram in Figure 9), exposing the risk of the chromium content to drop below the amount necessary to form a passive layer (12%). As a result, the regions adjacent the grain boundary may be no longer protected, leaving the metal in active conditions.
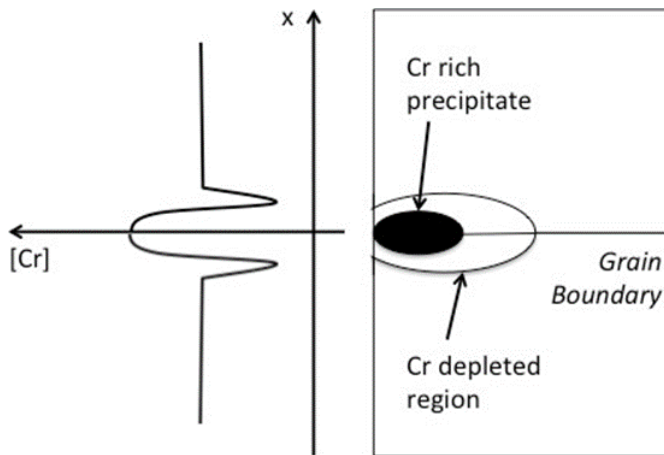
Figure 9 - Sketched of the chromium distribution caused sensitization at the grain boundaries.

2.2.1.2.5 Atmospheric Corrosion

The exposure of metals to air containing both pollutants and humidity can promote a corrosion form called atmospheric corrosion. The chemical composition of the thin film of electrolyte, which is exposed to oxygen and pollutant, depends not only on the availability of salts but also on the relative humidity. A dry surface contaminated with hygroscopic salts is virtually immune to atmospheric corrosion until the relative humidity is enough to hydrate the salt and form a thin film electrolyte [50]. The relative humidity for the salt to absorb water and form droplets of saturated solution is called the "deliquescence relative humidity (DRH)" and represents the most aggressive thin film conditions. The lowest the deliquescence point for a salt, the lower the relative humidity needed to reach the most aggressive conditions. In seawater environment the salts with the lowest DRH are $MgCl_2$ and $CaCl_2$, which are therefore often used to study atmospheric corrosion in chlorides rich environment.

The atmospheric corrosion attacks, coupled with the stress applied to the material, can cause what is referred to as atmospheric-induced stress corrosion cracking.

2.2.2   Environment Assisted Cracking

Environment Assisted Cracking (EAC) is the name commonly used to identify all the failure mechanisms that involve the growth of a crack in a material under a mechanical stress (applied or residual) lower than the ultimate tensile stress and in presence of a reactive environment. The driving force for the crack propagation is both chemical and mechanical in EAC, as the material in the same conditions would not fail with just one of the two contributes.

Chloride induced stress corrosion cracking is one of the most common failures in stainless steels [51–53]. Even though the beneficial effect of the duplex microstructure has been evident since DSSs earlier application and their resistance to SCC is greater than corresponding austenitic grades, this type of corrosion still occurs. The conditions under which cracks generate and grow are still matter of discussion; their understanding calls for considerations about the role of localised corrosion and hydrogen embrittlement in the crack initiation and progression, which is discussed in this chapter. A review of different proposed mechanisms is also included.

2.2.2.1 Stress Corrosion Cracking

In an active/passive alloy, the initiation of a crack in the material requires the rupture of the passive film that protects the grains. In fact, one of the most likely initiation site for SCC is where localised corrosion phenomena, such as pitting or crevice corrosion, are happening. All the defects that can weaken the passive film as inclusions, local de-alloying and anodic precipitates can be possible initiation points for SCC. However, the progression of a crack would be impossible without further reactions - between the environment inside the crack and the alloy - happening at the crack tip. Some of the most likely mechanisms studied in the years are reported in the following section.

2.2.2.2 Mechanisms of Stress Corrosion Cracking

Film-rupture mechanism. This mechanism, proposed at first in the '70s by Vermilyea [54] involves the rupture of the passive film when the crack tip intersect slip bands in the grains. According to this model, the metal is dissolved at the crack tip in a direction perpendicular to the stress, with a moderate dissolution of the material behind the crack tip. Once the passive film is damaged, the dissolution proceed till the passive film reforms, following preferential paths – see Figure 10.
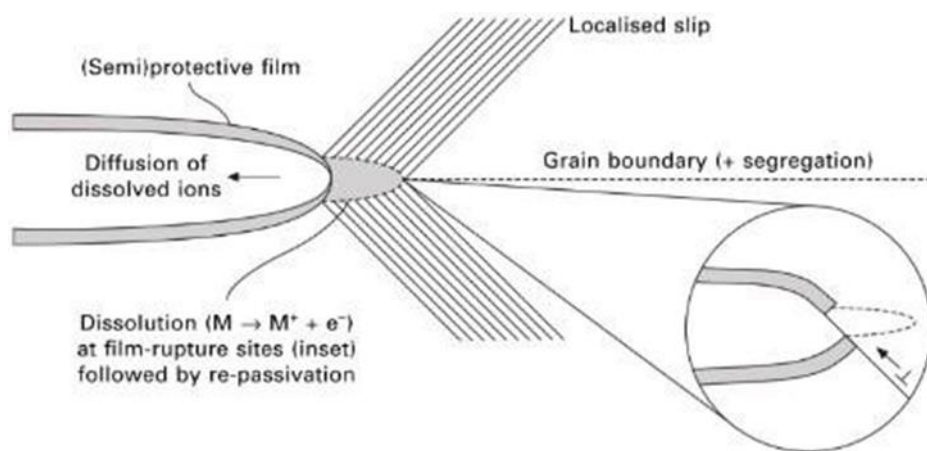
Figure 10 - Schematic representation of the film-rupture mechanism[54]

Selected-dissolution vacancy creep[55]*.* Vacancy generation in the surface layer of a metal has been proposed to occur as the effect of different processes such as the active dissolution of the metal surface in acidic environment, the growth of the passivating oxide film or the absorption of hydrogen in the metal. A mechanism that keeps into account the role of vacancies is the selective- dissolution vacancy-creep (SDVC) - first proposed by Hänninen et al. in 1996 [56]. According to this model, vacancies are injected into the metal as a result of the oxidation process; the cation vacancies forming at the interface between the passive film and the solution, when rupture of the passive film has not occurred yet, are thought to be transported through the oxide film to the metal surface beneath; here, they are injected into the metal

45

lattice and interact with the existing defects. In particular, vacancies can interact with dislocation in the plastic zone ahead of the crack tip – resulting in locally enhanced plastic flow in this region and in facilitated cracking by localised shear. Vacancies can also collect in voids, enhancing also in this case the susceptibility to crack by localized shear. As a consequence, the passive film break- down at the crack tip occurs.

Surface-mobility mechanism (SMM). This mechanism, proposed by Galvele [57] suggests that the growth of a crack may be assisted by the diffusion of superficial atoms from the highly-stressed region around the crack tip to fill vacant lattice position behind the crack, leaving new vacancies at the crack tip. The rate of migration of vacancies to the crack tip is the controlling step for this mechanism. This mechanism requires the diffusion rate of vacancies at the surface to be higher than the diffusion rate in the volume. In fact, even though the concentration of vacancies in a tensile-stressed material is higher than its equilibrium concentration, the diffusivity of vacancies at the temperatures typical for SCC - at least below half of the melting temperature, which is approximately 1450°C for a 2205 duplex stainless steel - is still very slow. Thus, an abnormal diffusivity at the surface is required for this model to match. The presence of contaminant on the surface, which is almost unavoidable in real conditions, provides the material with low melting-point build ups that explain the enhanced diffusivity, as demonstrated by the same author.

Film-induced Cleavage (FIC). This mechanism, developed by Sieradzki and Newman [53], introduces the concept that thin films can promote a brittle behaviour in a normally ductile material on a microscopic scale. The innovative aspect of this theory is that the high anodic dissolution rates required by other theories to justify the speed of progression of the crack are no longer required. In fact, the role of the anodic reaction is required just to produce a cleavage-initiating film that will undergo a brittle fracture

followed by a brittle fracture of the substrate itself covering a much longer distance (up to 1000 times the thickness of the film). Finally, obstacles (as pre-existing or deformation-generated defects) lead to crack arrest and blunting. A schematic diagram for the FIC mechanism is given in Figure 11.
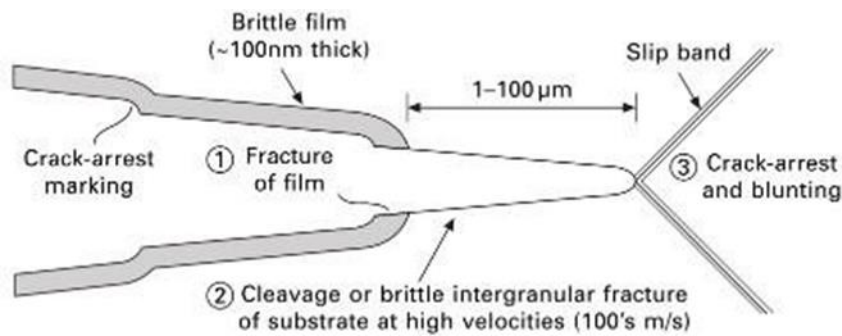
Figure 11 - Schematic diagram for the Film-Induced Cleavage mechanism [53]*.*

2.2.2.3 Mechanics of Stress Corrosion Cracking

By a macroscopic point of view, the production of a SCC attack results in a strong reduction of the Ultimate Tensile Strength (UTS) or, in other words, results in failure of the material when the applied stress is far lower than the yield stress for the material. When considering the fracture mechanics at the tip of a crack, a stress intensity factor, K (MPaVm), is introduced to keep into account the effect of a remote stress on this particular region. When the mode of fracture is tensile, the parameter is called K_I.

The upper limit of the stress intensity factor for a crack to propagate further, is called the critical stress intensity factor, K_{Ic}. When SCC occurs, the stress intensity required for the crack propagation drops to lower values as the stress on the materials is no longer the only driving force for the crack to advance. The threshold stress intensity

factor required for the crack to propagate in presence of stress corrosion cracking is indicated as K_{ISCC}, and can be as lower as a few % of K_{Ic} only [58].

The velocity of a crack progression in the stress regimes below K_{Ic} does not follow a linear relation with the stress intensity. In particular, just above the K_{ISCC} the crack initiate and the propagation velocity increase (region "I" in Figure 12) until the crack reaches a stable velocity (plateau in region "II" in the same figure) where further increase of the stress intensity factor have almost no effect on the propagation, suggesting that the controlling mechanism is the electrochemical dissolution. The crack velocity starts to increase again when K is approaching K_{Ic} and the mechanical contribution to the propagation is greater.
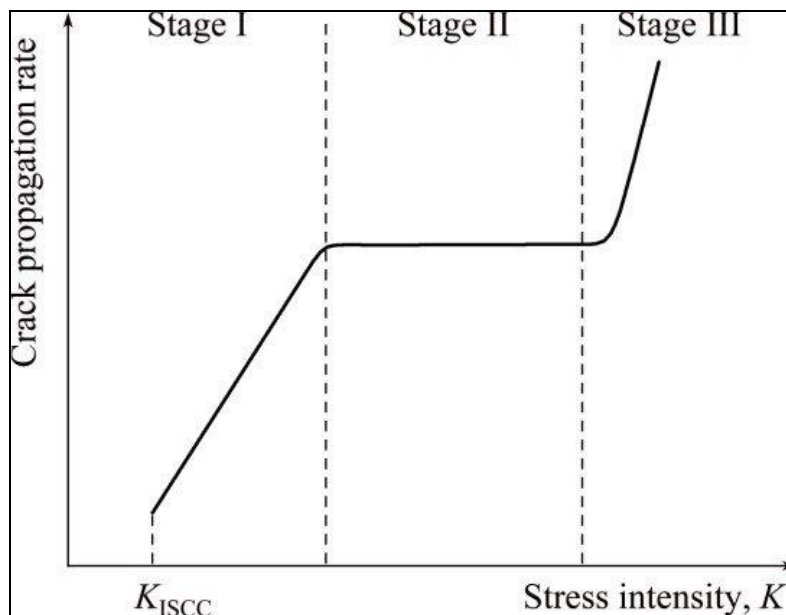
Figure 12 - Stress corrosion crack propagation velocity versus stress intensity factor.

2.2.2.3.1   Slow Strain Rate Tests

A type of test used to evaluate the resistance to stress corrosion cracking of a material is

the slow strain-rate test (SSRT) – sometimes referred to also as constant extension rate tensile test (CERT) . In this test, a constant increasing elongation is applied using a low strain rate. The selection of the strain rate is based upon the material and the environment; in ASTM guidelines, the strain rate suggested for the area of interest of this project, stainless steel in chlorides environment, is $1x10^{-6}s^{-1}$. This test is considered to be quite severe while being faster than long-term atmospheric exposure tests [59].

2.2.2.4 Hydrogen Embrittlement

Mechanisms of SCC based on hydrogen adsorption have many similarities with the mechanisms proposed for Hydrogen Embrittlement. A review of the HE mechanism is given in this chapter.

2.2.2.5 Mechanisms of Hydrogen Embrittlement

Hydrogen-enhanced localised plasticity (HELP)[60]*.* The principle underlying this mechanism is that hydrogen assisted cracking occurs because the solute hydrogen facilitates the movement of dislocations. The hypothesis of this mechanism is that, as high hydrogen concentrations are localised near the crack tips - because of hydrostatic stress recalling hydrogen from within the material or hydrogen entry at the crack tip - the deformation is localised around the crack tip. A comparison between the plastic zones with and without hydrogen is shown in Figure 13.
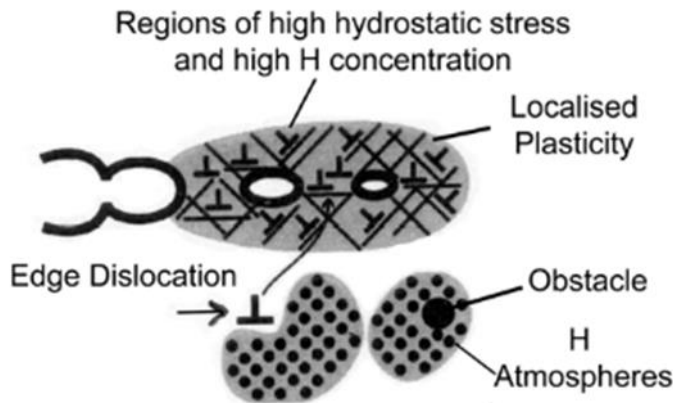
Figure 13 - Schematic diagram illustrating the HELP mechanism[60]*.*

Hydrogen-enhanced decohesion (HEDE). The decohesion hypothesis requires the hydrogen to induce weakening of the interatomic bonds making the tensile separation of atoms more favored than the slip. The weakening of the metal-metal bond is thought to be the consequence of the reduced charge-density due to the presence of high concentrations of atomic hydrogen in the metal [61]. High concentrations of hydrogen can occur in a variety of locations in proximity of the crack tip but a common requirement which is thought to be necessary for the hydrogen concentration to raise to sufficiently high levels is the presence of high elastic stresses [61]. Explaining the fracture purely as a sequence of atoms tensile separation after reaching a critical crack-tip opening displacement (CTOD) is not sufficient. Because of the constraining effect of the other atoms surrounding the crack tips, the separation process is likely to be more complex, with shear movements of atoms probably involved in reaching the CTOD of the crack tip.

Adsorption-Induced Dislocation Emission (AIDE) [62]*.* The AIDE mechanism is based upon the hydrogen-induced weakening of the atomic bonds, similarly to the HEDE mechanism, and the crack growth by localised slip, as for HELP. The "dislocation emission" is referred to both the nucleation and the subsequent movement of dislocation, with the hydrogen adsorption facilitating the first. In fact, the nucleation stage involves the formation of a

nucleation core and a surface step, which is generated by the shearing of atoms; in this stage hydrogen, weakening the interatomic bonds over several atomic distances, facilitates the process. When a crack grows in a ductile material in an inert environment (not considering hydrogen), growth appears to proceed by egress of dislocation (nucleated in the plastic zone ahead the crack tip) and little or no emission of dislocation from the crack tip occurrs. When dislocations are not emitted from the crack tip and are, instead, emanating from near-crack-tip sources, only a fraction of these dislocation intersect exactly the crack tip. The most of them contribute to blunting of the tip and straining of the region ahead. The crack growth by microvoids coalescence in these conditions requires large strains and the nucleation of large voids requires at the same time the nucleation of small voids between them. As a result, a surface fracture with small dimples within larger and deeper dimples develops (see Figure 14).
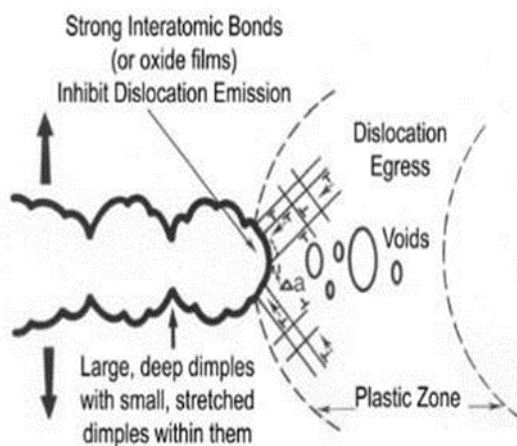
Figure 14 - Ductile crack growth by egress of dislocation nucleated from near-crack-tip sources and no emission of dislocations from the crack tip [62]*.*

On the other end, when hydrogen weakens the interatomic bonds - promoting the emission of dislocations from the crack tip - the dislocation activity is more relevant for the progression of the crack. Dislocation emission on inclined slip plans around the crack tip give rise to both crack-advance and crack-opening. Voids coalescence still occurs, but smaller strains are required. As a result, dimples on the crack surface are smaller and shallower (see Figure 15).
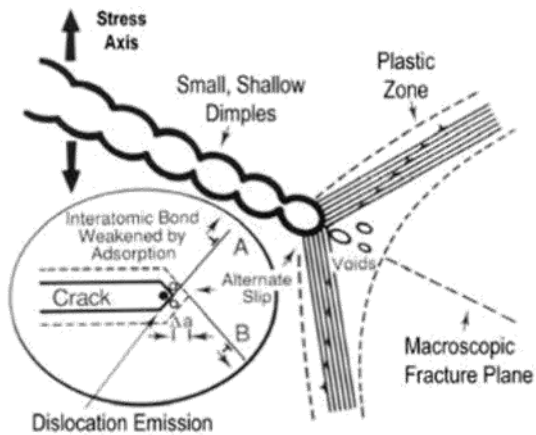
Figure 15 - Schematic illustration of AIDE mechanism, involving crack growth by alternate slip (intergranular path in this example)[62]*.*

2.2.2.6 Localised corrosion and Environment Assisted Cracking in Duplex Stainless Steels

This section contextualizes some of the corrosion mechanisms discussed till now in the frame of a dual-phase microstructure. Characteristic aspects of SCC and HE for duplex grades are summarized.

2.2.2.6.1 Pitting Resistance in Duplex Stainless Steels

The presence of Cr, Mo and N in duplex stainless steels provides them with good resistance to pitting in chlorides containing environments [63]. The Pitting Resistance Equivalent Number (PREN) is often used to rank the pitting resistance of an alloy; however, in this family of alloys, the two phases show different compositions. The tendency of the alloying elements to partition in one of the two phase suggests that a PREN [21,64] number should be calculated for each of the two phases. Cr and Mo provide ferrite with good pitting resistance, while the same result is achieved in austenite by the N and Ni additions.

$$PREN = wt.\% \, Cr + 3.3wt.\%Mo + 16wt.\%N$$

The amount of alloying elements is balanced to avoid formation of tertiary phases and precipitates, with excess of Cr promoting the formation of σ-phase [65,66] and N promoting the precipitation of Nitrides because of its low solubility in metals. However, incorrect thermal cycles or complex welding procedures can alter the phase balance. σ and χ [27,33] phases are known to have detrimental effects on the corrosion resistance of the alloy and nitrides has been shown to act as pitting initiation sites when their formation in ferrite occurs [63].

2.2.2.6.2   Stress Corrosion Cracking in Duplex Stainless Steels

The presence of two phases in duplex steels has a great positive impact on the SCC resistance of these alloys. In fact, if at least one of the phases is resistant to both corrosion and cracking in the specific environment and the phases are distributed with good connectivity, the progression of a crack is strongly impeded.

The effect of the duplex microstructure in blocking the progression of a crack can be appreciated by considering the behaviour of the single constituent phases individually. Newman and Cottis [67] compared the threshold stress to failure for a duplex grade with the individual ones for the austenite and ferrite phases (i.e. austenitic and ferritic steels with a similar composition to the one of the constituent phases in the studied duplex grade). The results showed that, in magnesium chloride solution at 153°C, the stress required for the duplex grade to fail was close to its yield stress, σ_y, while it was approximately 50% of σ_y for the austenitic alloy and only 20% of σ_y for the ferritic.

This outcome can be explained by considering what happens inside a crack, where an acidic environment is developed (being the metal ion hydrolysis the main mechanism) [46,68,69]. In chlorides-rich acidic environments, ferrite has a lower corrosion potential

than austenite. When a crack in ferrite reaches an island of austenite, then, the mixed potential inside the crack drops, thus not favouring further cracking of austenite. The protective effect of ferrite on austenite, relies on the difference in the corrosion potentials of the two phases [69][69–71].

2.2.2.7 Hydrogen Diffusion in Duplex Stainless Steels

The effect of the hydrogen dissolved in the grains, both austenitic and ferritic, can play a role in the cracks progression when considering EAC. Transgranular cracking through the austenite grains can occur and hydrogen may be part of the process.

The diffusion coefficient and the solubility of atomic hydrogen in ferrite and in austenite are strongly different. The higher diffusivity in ferrite ($\sim 10^4$ times more than in austenite [72–75]) makes the contribution of the diffusion through austenite negligible.

The diffusivity of hydrogen in duplex steel, though, is not comparable with the one in fully ferritic steels. A direct observation of this difference has been purposed by Turnbull et al. [72,76] who measured the diffusivity of hydrogen in a duplex alloy – UNS S32404 with 44% of austenite - and the diffusivity in the same alloy but solidified in a fully ferritic microstructure by heating at 1350°C and quenching in oil. They found the diffusivity to be 400 times lower in the duplex phase microstructure. At least two aspects can explain this difference. The first is the different solubility of hydrogen in austenite and in ferrite. Hydrogen in austenite has higher solubility, so the islands of austenite in the ferritic matrix act as hydrogen traps, retaining part of the diffusing hydrogen (the solubility of hydrogen in austenite increases when residual stress is left [77], which is a practical situation found in welds. In second instance, the interfaces

between austenite and ferrite also act as hydrogen traps. They show to have higher binding energy, becoming than the main obstacle to hydrogen diffusion .

The global diffusion coefficient for a duplex stainless steel is related also to the dimension and the distribution of the phases. In particular, the tortuosity of the interfaces has a significant effect on the diffusivity [45] - a "tortuosity factor" is usually introduced in the calculation of the diffusion coefficient to keep the effect of the microstructure morphology into account [72]. The matrix of ferrite embeds islands of austenite with low hydrogen solubility; as a result, the effective diffusion path of hydrogen is no more linear across the whole thickness of the material – see Figure 16).
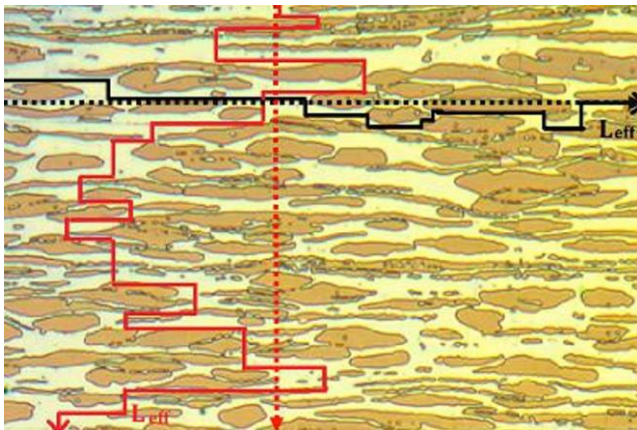
Figure 16 - 2D sketch of the effective diffusion path (Leff) of hydrogen in the rolling (black) and the transversal (red) directions. The tortuosity factor keeps in account the effect of austenite – darker in the image - with respect to a purely ferritic alloy (dotted paths).

2.2.2.8 Hydrogen Embrittlement and Hydrogen-Induced Microstructural Changes

The hydrogen embrittlement resistance of a DSS is strongly influenced by the microstructure. Being the low solubility/high diffusivity phase, ferrite is the most susceptible of embrittlement and the increased susceptibility to HE with increasing ferrite content is known [77]. More in depth, also the dimensions of the ferritic grains have an effect on the HE resistance. In particular, Chou et al [78] have shown how the

increasing grain size is detrimental on the mechanical properties of the DSS2205 alloy. Further, also tertiary phases such the sigma-phase can have a role in crack progression, as shown for example from Toshio et al. [79] for DSS2205 and 2507. Increased grain size, higher ferrite content and precipitation of tertiary phases have in common to be frequent features found in the heat affected zones of DSS welds. Consistently, HAZ are normally the preferential location for embrittlement failures initiation, as reported by Woollin et al. [80,81].

However, one of the aspects that are often associated with hydrogen uptake in DSS but not normally discussed in the frame of hydrogen embrittlement is the effect of hydrogen on a microscopic scale. In between the reduction in ultimate tensile strength and the effects at the scale of a crack tip, effects of hydrogen on the microstructure of the DSSs have been considered in this section.

Hydrogen has been reported to have two effects on austenite. Observing the phase evolution during cathodic charging of an alloy with residual stresses inside (such as the ones introduced by welding), it is possible to see that new slip bands appear in the austenite grains [82,83]. One possible explanation is that the presence of hydrogen in the grains causes a reduction in the shear modulus, which is the stress to overcome in order to generate new dislocations by multiplication. Being a source of dislocation already present (the residual stress in the material), the hydrogen stored in the grain could facilitate the whole process. For a Frank-Read type of source, the critical shear for multiplication of an existing dislocation can be expressed as [61,84]:

$$\tau_{CRIT} = k\frac{2Gb}{l}$$

where τ_{crit} is the critical shear stress for the dislocation emission, G is the shear modulus of the material, l is the distance between the two pinning sites locking the dislocation and b is the Burgers vector of the dislocation. This explanation has lot in common with the "AIDE" mechanism described in the "Hydrogen Embrittlement" section and could play a role in EAC, where hydrogen is locally generated in a crack tip and stress/strain fields are developed around the tip.

However, hydrogen in the austenite can also promote the transformation of austenite into martensite. It has been shown [85] that the γ phase can undergo transformations to γ* (face centred cubic hydrides), and then to ε (hexagonal close packed martensite) before finally evolve in α' martensite (body centred cubic). The possibility for the generation of martensite inside the austenite phase has been confirmed in literature both with AFM (Atomic Force Microscope) and EBSD (Electron Back-Scattered Diffraction) [82]. Further, the generation of slip bands can be observed also with common metallographic inspections.

Transformations are supposed to occur in both the two phases. Together with the martensite formation, needle-like relieves on the ferrite has been shown to form – see Figure 17. The nature of this modifications in ferrite is not yet elucidated; a proposed explanation that needs further investigations is that the microstructural change in ferrite – where the hydrogen solubility is low – is the result of new hydride phase formation within the ferrite grains [85].
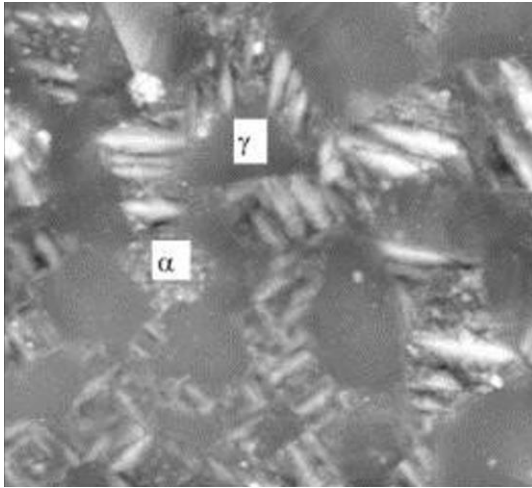
Figure 17 - AFM topography map of a duplex stainless steel sample after hydrogen cathodic charging. Adapted from ref [82]*.*

2.2.2.9 Role of Hydrogen in Stress Corrosion Cracking

Hydrogen embrittlement and stress corrosion cracking have been historically studied as two separate corrosion mechanism and theories for both mechanisms have been devised individually [86]. Oxidation of a metal, however, is always accompanied by a cathodic reaction that, in acidic environments such as inside a stress-corrosion crack, provides a source of hydrogen that can be reduced and diffuse into the metal, resulting in a local source of hydrogen. Hydrogen has the potential to diffuse into the crack tip and interact with the stress field at the crack tip [86,87].

When the stress at the crack tip is sufficiently high to activate dislocation source, dissolved hydrogen easily diffuse in this region, due to the large binding energy with sites in the strain field surrounding a dislocation and even more so with the dislocation core [87,88]. The theoretical hydrogen enhanced diffusion at the crack tips have been shown experimentally using secondary ion mass spectroscopy (SIMS), which allowed to observe higher concentrations of hydrogen in the region surrounding the tip. [86,87,89]

The presence of hydrogen in this region can facilitate stress corrosion mechanisms by promoting faster anodic dissolution rates of the metal [88,90]. At the same time, hydrogen

can enhance the plasticity of the metal [84,91,92], following the same mechanisms described for cathodic hydrogen embrittlement and rendering the progression of the crack in the metal easier.

2.3 WELDING AND THERMO-MECHANICAL SIMULATION

In this section, the welding technique used for this project is introduced. In particular, the main interest of this chapter is to describe the theory behind the welding process with a particular attention to the selection of the welding parameters. The simulation of the welding thermal history is also introduces in this chapter, with reference to previous work in DSS2205 heat affected zones simulations.

2.3.1 Tungsten Inert Gas Welding

One of the most used techniques for welding thin sheets, pipes and foils is the Tungsten Inert Gas (TIG) welding, also called Gas Tungsten Arc Welding (GTAW) [93]. TIG is an arc welding technique, which means that relies on the generation of an electric arc between the working piece (anode) and the electrode in the welding torch

(cathode). The electrode is a non-consumable tungsten electrode [94]. A column of highly ionized gas carries the electrical energy applied with a power supply between the two electrodes, which is isolated from atmospheric contamination by the use of an inert shielding gas. A TIG weld can be either autogenous (the material of the working piece itself is melted and used for the joining) or with a filler material, melted in between the arc and deposited in the weld pool [6,77,95]. A sketch of a typical set-up is shown in Figure 18.
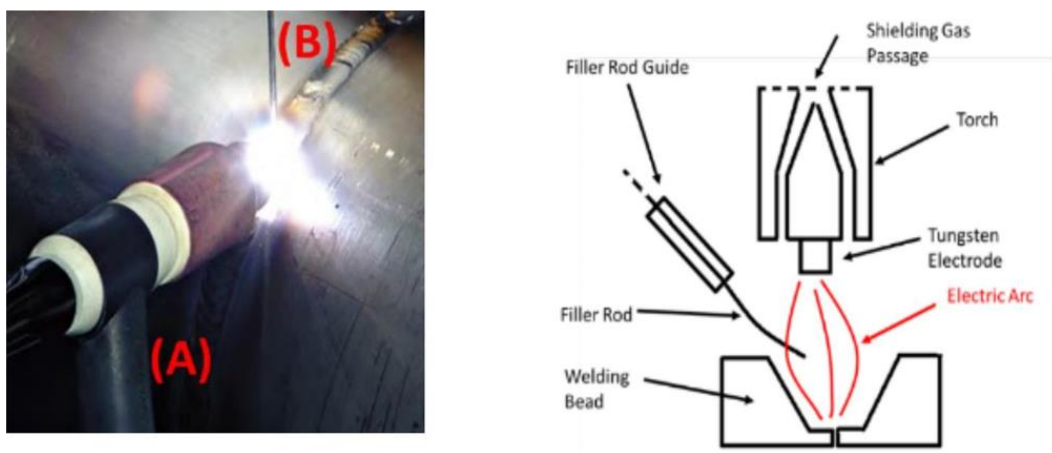
Figure 18 - Sketch of a TIG welding set-up. Welding torch (A) and Filler rod (B).

Different shielding gases can be used during welding. In particular, the choice of the gas is mainly oriented by the desired interaction of the gas itself with the chemistry of the weld [64,93]. Addition of nitrogen in the shielding gas, for the duplex grades, results in increased content of nitrogen in the weld, favouring the precipitation of austenite during cooling [64,93][96]. Irrespective of the gas used, when two completely separated pieces are welded together, the gas must be purged both around the welding torch and beneath the welding bead, at least until the base of the weld connecting the two pieces (called weld root) is completely solidified (backing gas).

2.3.1.1 Welding Parameters

When designing the welding procedure, the most important parameter to define is the heat input delivered to the material by the welding process. The amount of heat transferred is a result of the current applied to the torch and the travel speed of the torch across the welding piece. The relation between these parameters is defined by Equation 2, contained in the BS 4515-2-1999 standard [5], where Q (kJ/mm) is the heat input, V the voltage and I the current applied by the welding torch, v (mm/min) the travel speed of the torch:

$$Q = \frac{V \text{ x } I}{1000 \text{ x } v}$$

The ideal condition for a welded microstructure is to reproduce the 50:50 balance of austenite and ferrite of the solution annealed 2205 grades [97]. Practically, this result is difficult to achieve. Slow cooling rates (high H.I.) promote the formation of austenite but also the precipitation of intermetallic compounds, while fast cooling rates (low H.I) prevents the diffusion-controlled formation of austenite in the desired fraction. The optimal cooling time between 1200°C and 800°C, $\Delta t_{12/8}$ lies between 4 s and 15 s [4][6,98]. The corresponding heat input can be only estimated as the geometry of the weld and the thickness of the material, which acts as a heat sink, require to be considered. Nomograms as the one shown in Figure 19 are used to have an estimation of the heat input.
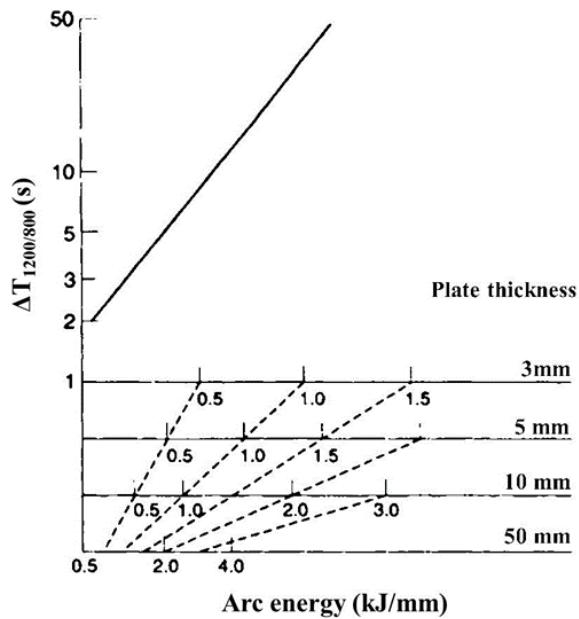
Figure 19 - Nomogram for the conversion of the Cooling rate in a heat input for a single pass weld on a large plate of known thickness. Adapted from [99].

Another parameter that can influence the final phase balance is the chemical composition of both the shielding and backing gas. The main purpose of these gases is to isolate the welding region from atmospheric gases and humidity, in order to prevent oxidation and formation of other defects. However, the addition of nitrogen in the shielding gas can be used to raise the concentration of nitrogen in the weld and, so, promote the austenite formation [64,93].

2.3.1.2 Weld Simulation and Corrosion Properties

Several authors have used physical simulations of DSS welding and subsequent corrosion testing. The effect of the chromium nitride in simulated HAZ and the beneficial effect of increasing reformed austenite has been shown with this method from Liou et al. [43,99,100]. In their work, corrosion testing was performed by means of polarization in 3.5% NaCl solution at different temperatures and exposure of U-Bend samples in 40% $CaCl_2$ solution at 100°C. They found that the higher nitrogen and cooling rates are beneficial to

avoid nitride formation. Further, in their work, SCC cracks in the HAZ progressed intergranularly when grain boundary austenite (GBA) was present, while they progressively assumed transgranualar character whit increasing amount of intergranular austenite (IGA) and Widmanstaetten austenite (WA). In particular, they have shown how the latter have beneficial effects in blocking and deviating the crack progression (see Figure 20).
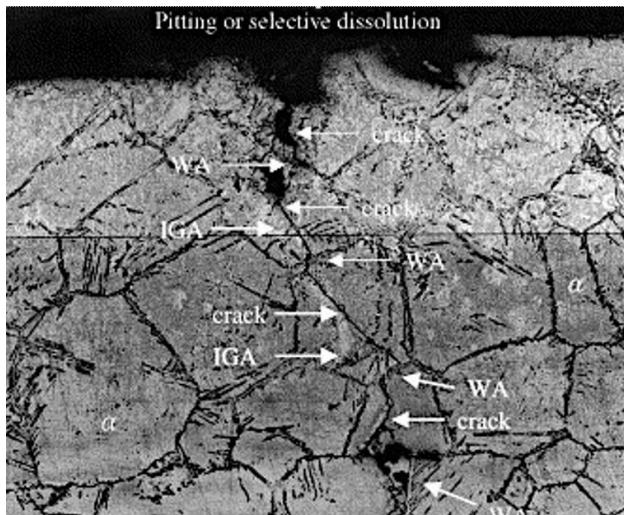
Figure 20 - Effect of IGA and WA on the crack deviation. SCC test in 100C CaCl2, cross section (image from[43]*l).*

The most extensive correlation of the Δt800/500 cooling intervals with the pitting resistance of the HAZ has been proposed by Yang et al [101], who compared the effects of cooling with the type and fraction of austenite reformed and, for each condition, measured the pitting resistance of the different microstructures. Their results have shown a direct increase in pitting resistance with the content of reformed austenite but, in particular, with the progressive replacement of grain boundary austenite with intergranular and Widmanstaetten austenite. This result is achieved by longer cooling times and the effect reflects on the pitting potentials as shown in Figure 21.
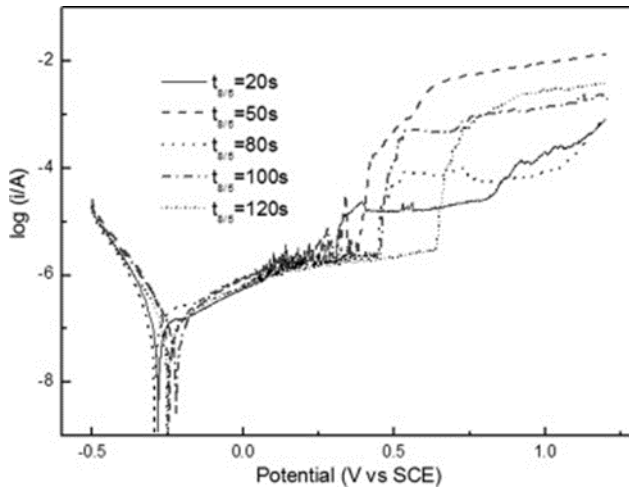
Figure 21 - Polarization curves in 3.5%NaCl at 30C for different simulated heat affected zones, distinguished by the 800-500C cooling time [101]*.*

Combining the results of the previous two studies, the detrimental effect of grain boundary austenite seems recurrent. Considering the thermal route that causes the formation of GBA, it seems important to highlight that the fast cooling has effects also on the chemical composition of the austenite in this morphology.

An extensive study of the chemical partitioning in the different austenite forms has been proposed by Yang et al [101] and by Zhang et al [21], who have characterized by means of energy-dispersive X- ray spectrometry the local chemical composition of the GBA and compared it with the IGA and the WA [42]. They have consistently found increased amount of Cr in the GBA and WA that showed therefore higher PREN number, while the IGA shows lower PREN (see Table 2).

Table 2 - Chemical composition of Ferrite, GBA, WA and IGA with different cooling time [101].

$\Delta t_{8/5}$	Phase	Cr	Ni	Mo	N[a]	PREN
20	GBA	21.86	5.71	2.26	0.19	35.02
	WA	21.78	5.76	2.12		34.48
	IGA	20.01	5.82	1.95		32.15
	Ferrite	21.85	4.57	2.71	0.05	32.29
50	GBA	21.79	5.72	2.25	0.19	34.92
	WA	21.68	5.68	2.09		34.28
	IGA	20.02	5.85	2.02		32.39
	Ferrite	21.92	4.56	2.79	0.05	32.63
80	GBA	21.81	5.74	2.23	0.19	34.87
	WA	21.7	5.63	2.11		34.36
	IGA	19.99	5.88	2.03		32.39
	Ferrite	21.88	4.48	2.7	0.05	32.29
120	GBA	21.79	5.69	2.28	0.19	35.01
	WA	21.66	5.61	2.32		35.01
	IGA	19.98	6.01	2.03		32.38
	Ferrite	21.85	4.41	2.68	0.05	32.19

The effects of hot deformation in cast duplex have been studied by Fan et al. [102], who correlated the ferrite and austenite recrystallization in the case of large deformations (ε=50%) and slow strain rates, which is a situation often encountered in metals forming [103–106]. The resistance to deformation drops with the processing temperature, as shown in Figure 22.
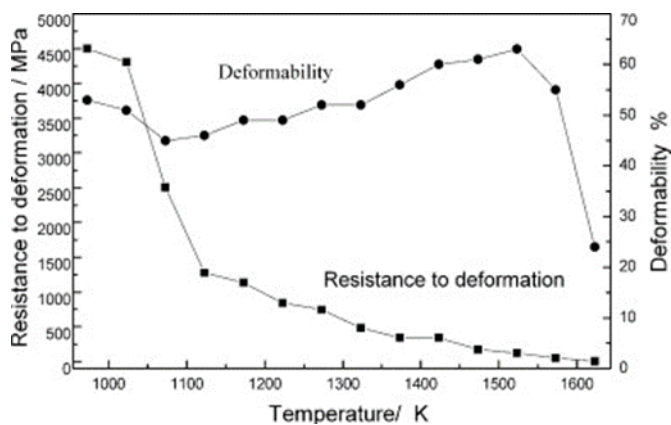
Figure 22- Resistance to deformation and deformability change with temperature.

When large hot deformation occurs, phase boundaries need to deform in order to assure the continuity of the material. An extensive study on the phase boundaries character before and after hot deformation has been proposed by Piñol-Juez et al. [107], who described the δ/γ boundaries mobility at 1000C with torsion tests. Their work, however, is not correlated with stress corrosion cracking properties of the deformed material.

One of the aims of this project is to develop microstructural descriptors and correlate them to the SCC/HE behaviour. In order to understand not only the role of the thermal history but also of the residual stress on the welded microstructure, thermo-mechanical simulations can be performed. An example of physical thermo-mechanical simulator the Gleeble[®] system. The same principles described for welding apply in the simulation. However, not only the local control of the temperature during the simulation is more accurate, but also external stress can be more easily applied.

In fact, two parameters can be controlled with the Gleeble[®] system: the time/temperature profile and the stress applied to the sample. It is known that stress has a great influence on recrystallization in metals and on grain boundaries energy and mobility [105]. The stress applied in this system can be either tensile or compressive and an example of the sample geometry is shown in Figure 23.

3 EXPERIMENTAL TECHNIQUES

This chapter offers an overview of the research techniques used throughout the project. Details of how these techniques have been used are presented in the manuscripts, while this chapter describes their working principles and the theory behind.

3.1.1 Characterization techniques

3.1.1.1 SEM based techniques

The scanning electron microscope (SEM) is a type of microscope that uses a focused beam of electrons to produce an image of the investigated surface. Different electron sources can be used in a SEM and field emission guns (FEG) equipped all the SEMs used for the work presented in this thesis. This type of emitters present several advantages with respect to thermoionic sources, with the higher beam intensity and the smaller beam diameter being the most notable [108][109]. As a result, FEG-SEMs can achieve higher imaging resolution while providing higher beam current when elemental and diffraction techniques are used.

The interaction between the electron beam and the atoms in the sample produce a variety of signals, which can be used to gather information on the sample topography and on its chemical composition. Backscattered electrons (BSE) are high energy electrons (i.e. >50eV) resulting from the elastic interaction of the primary electrons forming the beam (PE) with the atoms in the sample. Images acquired in this mode have contrast dependent on the atomic number of the elements forming the sample. Secondary electrons (SE) are low-energy electrons (<50eV) generated by inelastic scattering of the primary electrons with the electrons of the atomic shell. The emission intensity of these electrons is strongly

influenced by the topography of the sample surface. The ejection of a secondary electron from the inner shell of an atom leaves a vacancy in the electronic structure, which is readily filled by an electron from an outer shell. The difference of energy between the outer and the inner shells is released in the form of an X-Ray, which has unique energy and wavelength characteristic of the emitting element and transition level (Characteristic X-Ray) [110].

3.1.1.1.1   SEM-EDX

Energy-Dispersive X-Ray spectroscopy (EDX) is an analytical technique used for elemental characterization of samples in the SEM. Characteristic X-Rays are collected in a dedicated detector and their energy and intensity used to provide a semi-quantitative chemical analysis of the sample. In a conventional EDX setup, the detector is protected by a beryllium film (window), used to maintain the vacuum and to prevent contamination [111][112]. Low energy X-Rays emitted from light elements are absorbed by the window, rendering the quantification of these elements less accurate. Further, accurate quantification of light elements is limited by the presence of adventitious carbon and oxygen in the SEM chamber. The detection limit of light elements is partially overcome by the development of "Window-less" detectors, that allow for low voltage SEM operation and identification of light elements (such as, lithium and nitrogen).

3.1.1.1.2   SEM-EBSD

EBSD (Electron Backscatter Diffraction) is a microstructural-crystallographic technique used for microstructure characterization of crystalline materials. Incident electrons diffracted by the sample surface are intercepted by a phosphorus screen, where the figure of diffraction – called Kikuchi pattern – is recorded by a camera [113][114,115]. The bands visible in the

pattern correspond to electrons that escaped the material close to the Bragg condition and their relative position is used to determine the crystallographic structure of the diffracting material – see Figure 23.
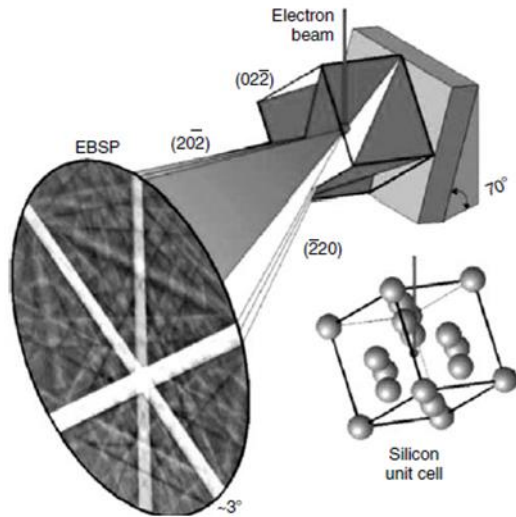
Figure 23 - Sketch showing the Kikuchi pattern formed by beam diffraction [113]*.*

The Kikuchi patterns corresponding to each spot investigated on the surface contain information on the lattice parameters and orientation of the grains forming the surface investigated. EBSD scans are conventionally shown as color-coded 2D maps, where the resolution of the map is determined by the spot-size parameters used in the EBSD acquisition.

3.1.1.2 Electrochemical techniques

3.1.1.2.1   Galvanostatic polarization

Galvanostatic polarization [116] is a two electrodes technique, where the electrochemical reactions occurring in the cell are controlled by a constant applied current. The setup consists of a direct current power supply connected to the sample (cathodic polarization) and to a platinum electrode (anodic polarization). The cell is completed by the electrolyte,

where both electrodes are immersed. During galvanostatic measurements, the electrochemical potential of the sample is free to change according to the reactions developing in the cell.

3.1.1.2.2   Potentiodynamic polarization and micro-cell

Potentiodynamic (PTD) polarization is a technique performed in a three-electrodes cell where the electrochemical potential of the sample investigated (working electrode) is varied with respect to a reference electrode of known potential and the current developing on the sample is measured. The potential/current diagrams produced with this technique are often referred to as Evan's diagrams and they contain useful information on the corrosion behaviour of the metal analysed. The polarization curved used in this project have been acquired using a microcell that was preferred over a conventional setup due to the ease of perform measurements over a small area. A sketch of the microcell is shown in Figure 24.
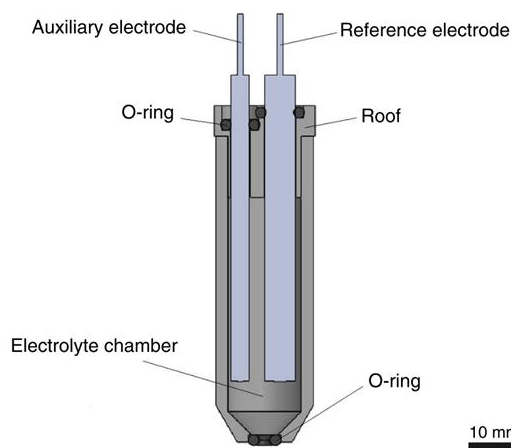
Figure 24 - Sketch of the microcell used for electrochemical measurements [117]*.*

3.1.1.2.3   Scanning – Kelvin Probe Force Microscopy (SKPFM)

Scanning Kelvin Probe Force Microscopy (SKPFM) is an AFM-based characterization technique used for local measurements of the Volta potential (ψ) at the surface of the

70

investigated samples [118,119]. The potential measured [120] provides an indication of the practical nobility of different regions of a surface, with the values measured as the difference in Fermi level between the electrons from the sample surface and the ones at the tip of the platinum-coated scanning probe (which effectively acts as a reference electrode). A diagram of the SKPFM setup is shown in Figure 25.
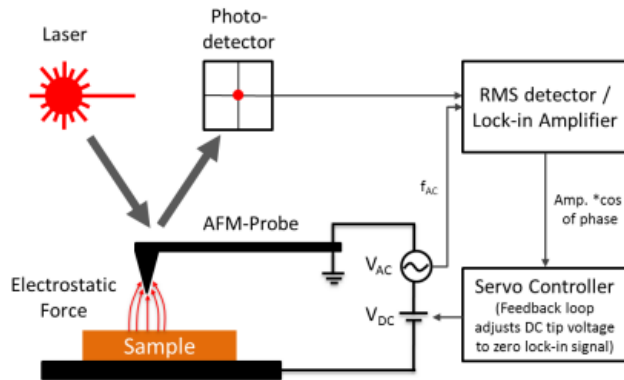
Figure 25 - Sketch of the AFM-SKPFM with electrical equivalent circuit [121]*.*

A quantitative correlation between SKPFM measurements and electrochemical potential of metals requires a careful calibration for each electrolyte investigated [122]; qualitatively, the relative nobility of features measured in the SKPFM reflects the scale of electrochemical potentials, allowing for identification of corrosion susceptible areas. From a semi-quantitative point of view, the difference in ψ function ($\Delta\psi$) between metallic phases or inclusion provides a local estimation of the anodic/cathodic character and, as a result, the different corrosion propensity [39,123].

4 EXPERIMENTAL RESULTS

4.1 PRODUCTION AND CHARACTERIZATION OF A REFERENCE WELD

The reference weld has been produced with at the TWI (The Welding Institute) facilities in Cambridge. Following the principles discussed in the literature review, the welding procedure specifications (WPS shown in Table 3) have been formulated for the purpose of this project and it is therefore slightly different from the industry practise. Some details of the welding procedure:

- Shielding/backing gas – the weld was performed in Argon environment, in order to avoid absorption of nitrogen from the environment in the weld [64]. This choice was motivated by the need to observe the spontaneous austenite reformation as driven by the thermal history rather than by the addition of nitrogen;
- Filler metal – the filler metal used was a 2205grade supplied from Metrode. The choice of a filler of the same metal was dictated by the need to compare the microstructure of the weld with the thermo-mechanical simulations, where additional nickel from an over-alloyed filler material would not be reproducible;
- Heat input – different heat input was used for the root pass and the intermediate passes, with the root performed at 1.5kJ/mm and the intermediate passes at 1.2kJ/mm;
- Pre-heating – the pipe sections were not pre-heated before welding;

The reference weld has been performed between two sections of a grade 2205 duplex stainless steel seamed pipe with wall thickness of 9.2 mm and internal diameter of 406.4 mm (16 inches) – see Figure 26. The composition of the 2205 duplex stainless steel alloy is listed in Table 3. Tack welding (intermittent welding of small pins between the two welding pieces) has been manually made to keep the two pipe sections in place. A semi-automated set up has been used, with the torch hold in a fixed position and the pipe sections in rotation.
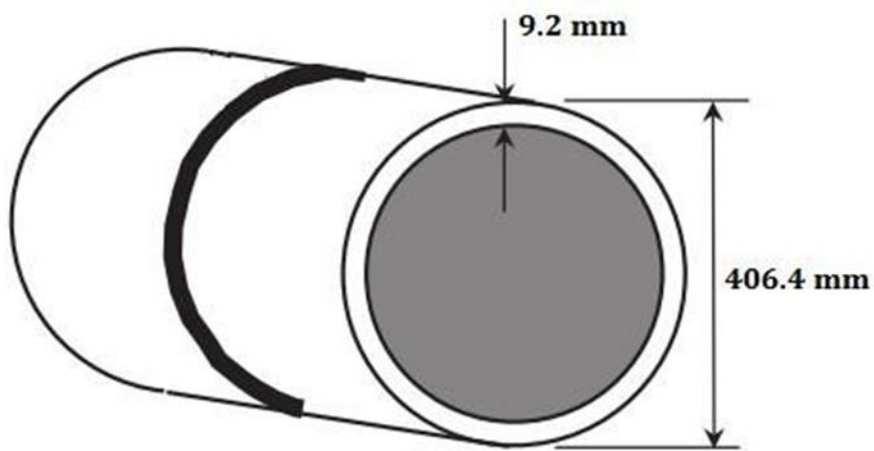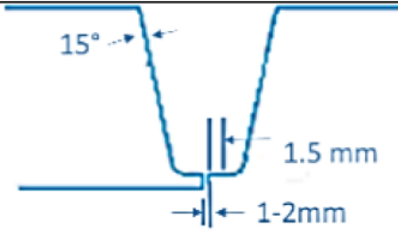
Figure 26 - Sketch of the girth weld used for the project with dimensions.

Table 3 - Welding procedure specifications.

	The Welding Institute		
TWI	**EN 15614 - pWPS - Details of weld test**		
	Weldspec		
Material Specification			
Pipe material and geometry	**Duplex Stainless Steel**	**Thickness**	**Diameter**
	2205	9.2 mm	406.4mm
Joint Secification			
Groove angle Root opening Root face	30 deg. 1-2mm 1.5	15° 1.5 mm 1-2mm	
Filler Metal			
Type	2205 DSS (Metrode)		
Diameter	1.2 mm		
Thickness deposited	9.2 mm		
Preheat			
Preheat	20 °C		
Max. Interpass	150 °C		
Gas			
Shielding gas	Argon	8-10 l/min	
Backing gas	Argon	5-10 l/min	
Electrical			
Amperes	80-200		
Volts	10-12		
Travel Speed	80-150 mm/min		
Maximum Heat Input	1.5 kJ/mm		

4.1.1 Microstructure Characterization

The initial steps of the characterization have been done using optical microscopy and chemical or electro-chemical etching. A section of the pipe has been cut with an automatic saw and smaller samples of the weld and heat affected zone cut from it with a cutting wheel. The reference weld with the welding passes numbered from 0 to 6, is shown in Figure 27. Pass "0" is commonly called "root pass". This is the pass that closes the bottom of the welding bead and provides the joining of the two welding pieces. Pass "6" is called "weld cap", this is the pass that closes the welding process. It shows macroscopic differences, due to the different cooling route – the molten material is more exposed than in the inner passes – and to the single thermal cycle – there is no reheating, as there are not further passes over it.
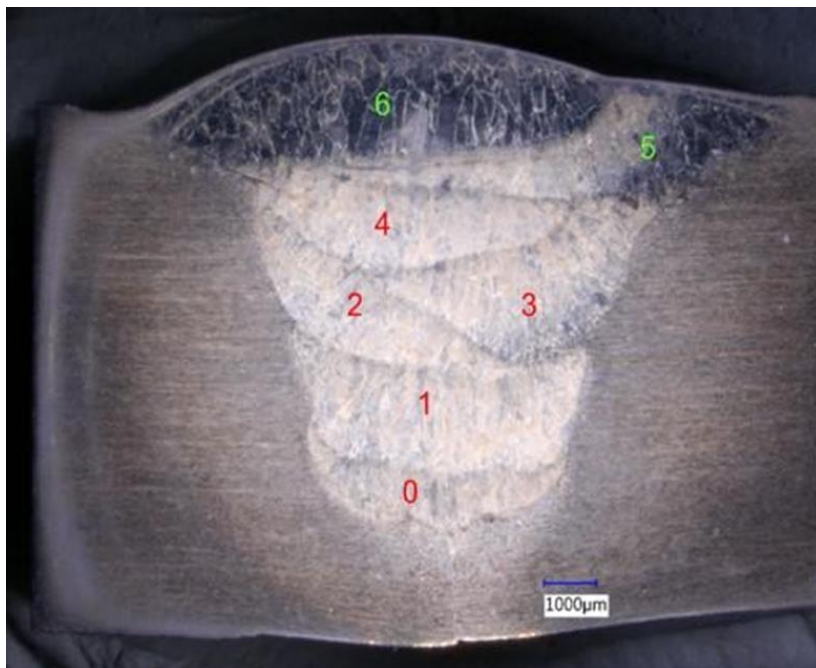
Figure 27 - Cross section of the reference weld, the seven different passes are labelled in the picture. Material etched in Glyceregia.

4.1.1.1 Etching Procedures used in the project

In order to observe the microstructure using optical microscopy, different etching techniques [124] have been applied on specimens cut from a section of the pipe. The different etching conditions highlight different features of the material and they will be used in different situations throughout this work. Details of the three etching procedures are defined in Table 4.

Table 4 - Etching methods for duplex stainless steels.

Name	Type of Etching	Electrolyte Composition	Etching Condition	Features Highlighted
Oxalic Acid (ASTM A-262 [125])	Electroetching	10% wt. $H_2C_2O_4$	5V, 6-60s RT	σ-phase , carbides (15–30 s), grain delineation (45–60 s)
Sodium Hydroxide (ASTM A- 923 [126])	Electroetching	20wt.% NaOH	1-3V, 3-8s RT	Ferrite, σ-phase
Glyceregia[124]	Chemical	HCl 15mL Glycerol 10mL HNO_3 5mL	1-3 min RT	Grain Delineation, σ-phase, Carbides

4.1.1.2 Austenite:Ferrite Ratio Measurements

One of the most important descriptor for characterizing a weld is the austenite:ferrite ratio inside the weld, with a target ferrite content below 70% . This can be measured by considering a range of methods. In industry, the ferro-magnetic response of material is measured, for example, by using the magnetic induction method. This method relies on the different magnetic properties of the ferrite, ferromagnetic, and the austenite, paramagnetic [17], and provides an instantaneous measurement.

Another test method which is widely used is the one proposed by the E-562 ASTM standard [127], which describes a manual point-counting technique. This method requires the preparation of a test grid, made of equally spaced points in either a circular or a square array, and the preparation of some materials micrographs on which the grid is superimposed (see Figure 28). Counting the points falling in each phase or in the grain boundaries, the average percentage of grid points on the features of interest provides an unbiased statistical estimation.

When duplex stainless steel is electrolytically etched in NaOH or KOH – or any other etching method that stains one of the two phases - a clear contrast between the two phases is visible in optical microscopy observations. This effect can be easily used to estimate the austenite:ferrite ratio by means of image analysis. A first attempt has been done using a common imaging software – ImageJ® [128].By converting the image in a black and white binary format, the contrast between the two phases is enhanced and the ratio of the image occupied by each of the two colours can be easily calculated by the software. A colour threshold in terms of RGB (red, green, blue) values must be imposed on the image in order to convert the brightest phase in white and the darker in black. However, the value imposed differs for each specific image. In fact, the

variability of the differences in colour, brightness or relative contrast between the phases need to be addressed each time.
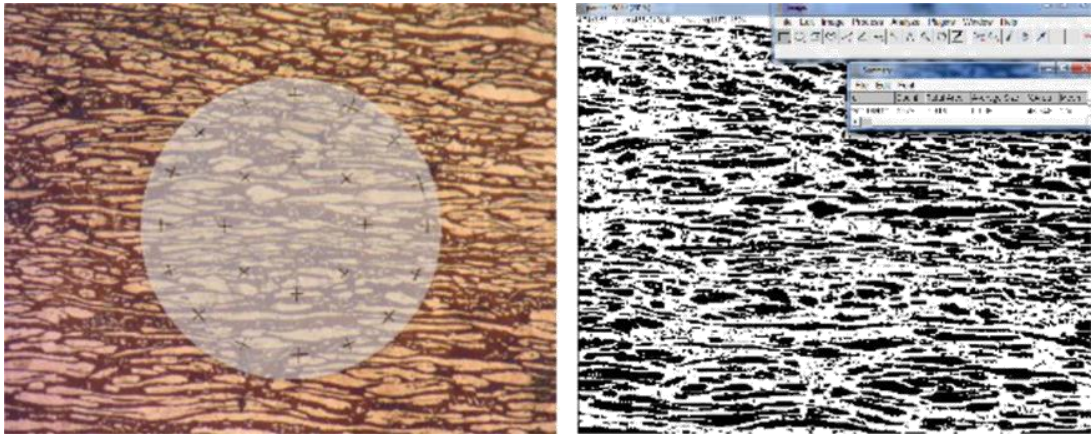
Figure 28 - Comparison of point counting and image analysis methods.

The ASTM-E562 points counting method and the image analysis method will be used to estimate the phases fractions of specific parts of the weld in the following paragraphs. Three regions have been chosen to show how these two methods can be used on different microstructures in the weld. The three regions are, namely, the parent material, the heat affected zone and an intermediate pass inside the weld, pass 1. The results of both the two methods are summarized in Table 5.

The pipe used for the reference weld is a seamed pipe. This type of pipe is manufactured from a flat plate, bended in a cylindrical shape and then welded at the extremities. So, the rolling lines from previous fabrication processes are maintained – see Figure 29. The austenite fraction and the distribution are homogenous, with thin elongated plates occupying 43 to 47% of the volume according to the different estimation methods
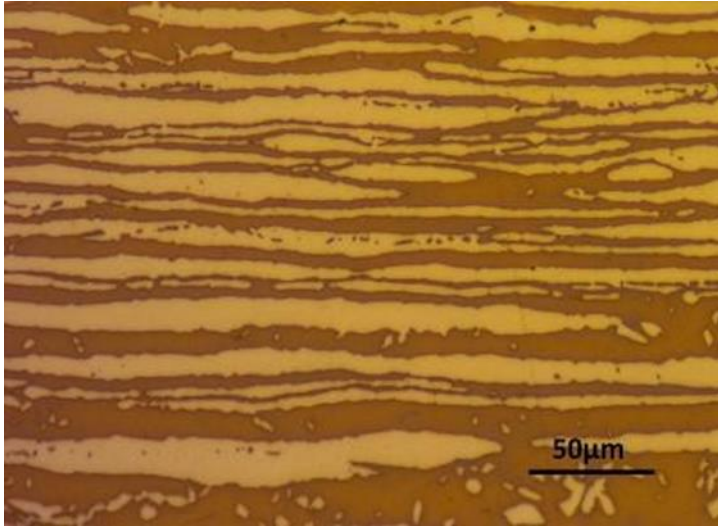
Figure 29 - Micrograph of the parent material after KOH etching.

The austenite:ferrite ratio in the heat affected zone, shows an increase in the ferrite content with respect to the parent material. The thermal cycle experienced by the alloy in this position causes the growth of the ferrite grains with the dissolution of the austenite when the A4 temperature is approached, followed by austenite re-precipitation – see Figure 30.
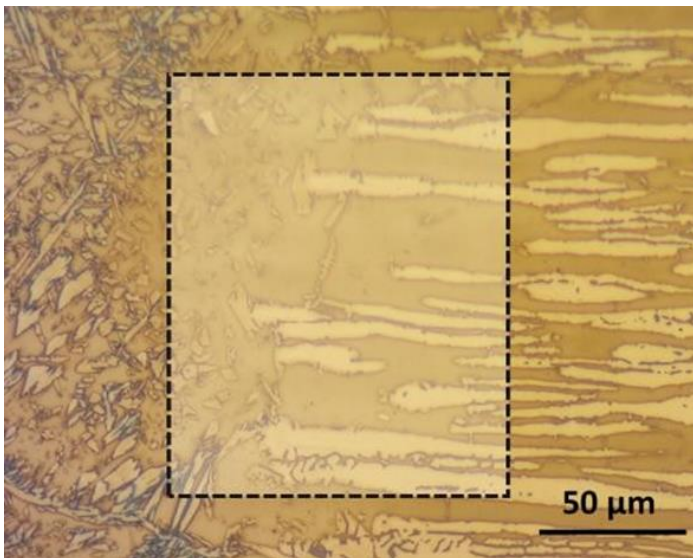
Figure 30 - Micrograph of the HAZ after KOH etching.

The root and the intermediate welding passes experience a complex thermal history during the welding process. In fact, after the first solidification of the filler material, the same

material will be heated again during the welding as the consecutive passes are performed. As a result, the microstructure in the weld is strongly inhomogeneous even though an orientation that follows the thermal gradient – from the root to the weld cap -is visible (circled in Figure 31).

Figure 31 - Micrograph of the weld pass 1 after KOH etching.

More in depth, the austenite in the intermediate passes shows a variety of morphologies. The microstructure can be simplified in elongated plates following a dendritic-like solidification with smaller austenite plates growing in between.

The small dimensions – an average of 11 x 12 μm^2 – of the austenite plates within the dendrites make the phase ratio estimation more difficult with the imaging software. In fact, the phase boundaries – dark after etching – occupy a relevant part of the picture. According to the ASTM E-562 method for the phase ratio estimation, in the points counting procedure this limit is overcome by considering the points falling on the phase boundaries as equally shared between the two phases.

With the imaging software procedure, the space occupied by the phase boundaries in the binary optical images has been treated in a similar way. The image has been converted in black and white considering the phase boundaries belonging once to the austenite and

once to the ferrite. This give two different phase ratios - with the boundaries attributed in one to the ferrite and in the other to the austenite; the average of the two austenite:ferrite ratios is then considered as the result of this measurement. The binary image in the two cases is reported, for the purpose of clarity in Figure 32.
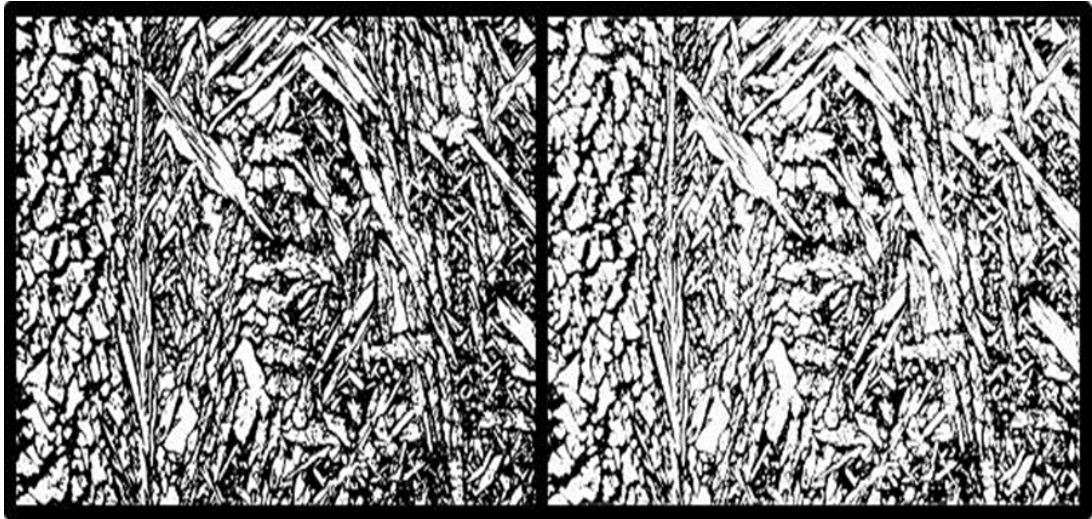
Figure 32 - Binarized images of the weld microstructure for phase ratio estimation with different colour threshold.

Table 6 summarizes the results of the two methods for the three regions discussed. For the ASTM E- 562 points counting technique, an average of three measurements has been considered, with the maximum and minimum values also reported.

Table 5 - Ferrite:austentie ratio in different regions of the weld measured with different techniques.

Method	Region		
	Parent Material	Heat Affected Zone	Intermediate pass
ASTM E-562	43:57	62:38	58:42
(average of 3 meas.)	(max 53:47, min 59:41)	(max 65:35, min 59:41)	(max 60:40, min 56:44)

| Image Analysis | 55:45 | 64:37 | 56:44 |

4.1.1.3 Micro-Hardness

The Vickers microhardness has been measured with a CSM instrument's Micro-Indenter (MHT) tester, equipped with a Vickers indenter, on a section of the weld ground up to 4000 grit emery paper and polished with diamond paste up to 1 μm. Measurements have been taken in different regions and repeated four times with a minimum distance between two measurements of 250 μm. Results are summarized in Table 6. The load time was 10 seconds and the load 10 N. This technique has been preferred over a macrohardness measurement because of the possibility to position the indenter on specific regions of the weld. In particular, the regions measured are the cap weld, the heat affected zone, the parent material and inside the weld on an intermediate pass (see Figure 33).
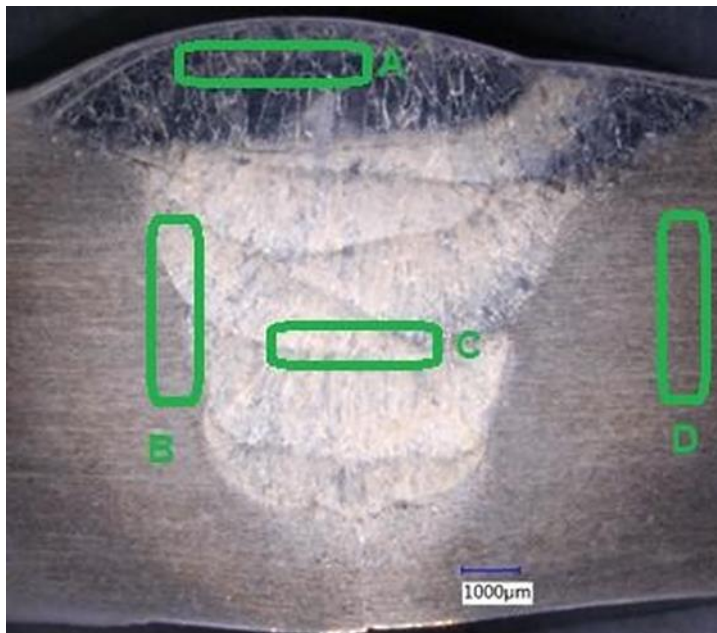
Figure 33 - Weld cross section with region labelled.

Table 6 - Microhardness of different regions of the weld.

Region		A (Weld Cap)	B (HAZ)	C (Weld centre)	D (Parent mat.)
Hardness	**(avg.)**	**269**	**212**	**215**	**252**
(HV$_{10N}$)	(max.)	285	242	223	258
	(min.)	252	197	203	241.

The microhardness measurements showed little variation in the different regions of the weld, with lower values in the weld and slightly increased hardness in the weld cap. In particular, hardening in the HAZ was not revealed. In order to verify these results, the hardness across the HAZ has been measured also with nanoindentation [129–131], providing higher resolution of the hardness profile by using a 100 nm spacing.
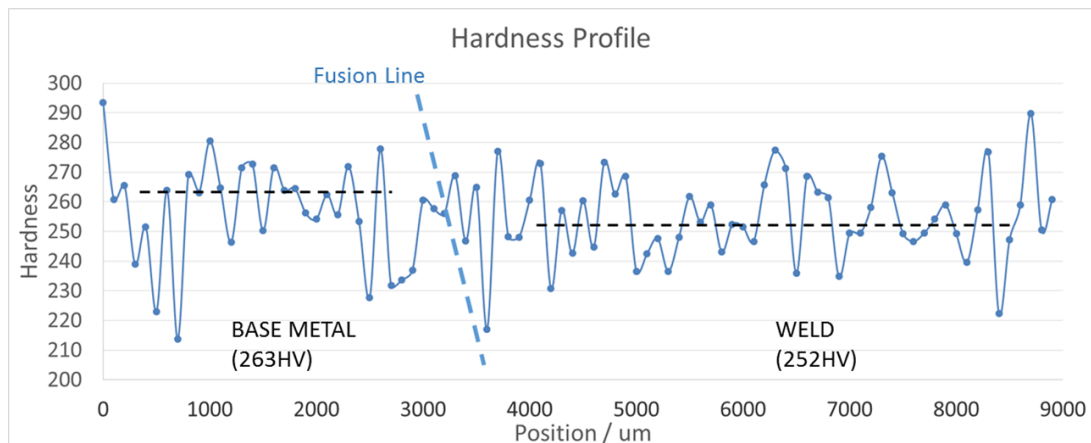
Figure 34 - Nanohardness profile across the weld HAZ.

Similarly to what noticed with micro-hardness, there was no noticeable hardness increase in the HAZ. Slightly lower hardness was notice inside the weld also in this case – the nanohardness profile is shown in Figure 34.

4.1.1.4 XRD Residual Stress

Residual stress is often present in the materials after manufacturing. Stress can have different origins and in duplex steels the different mechanical properties of the two phases

give rise to an inhomogeneous stress distribution [132]. When the alloy is welded, also thermal stress are generated in the weld pool and in the heat affected zone and the stress distribution takes into account the influence of both the two contributes [133].
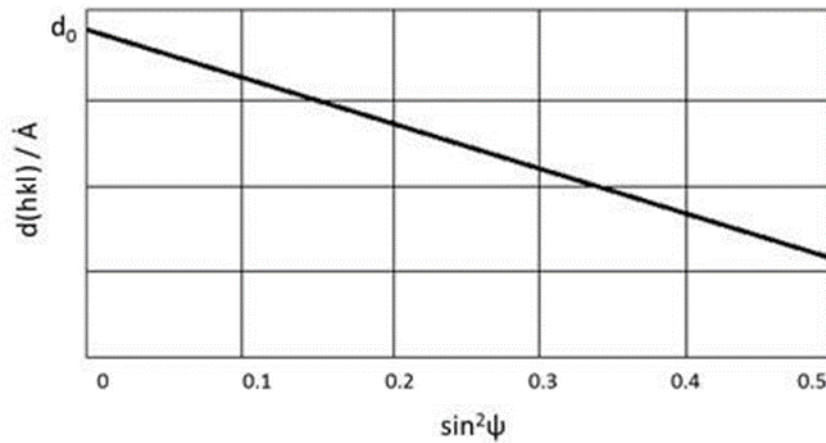
Figure 35 - sin2ψ method for residual stress estimation. Sketch of the lattice distance for the plane (hkl) against sin2ψ.

The principle for measuring the residual stress with XRD is based upon the distortion of the lattice parameters with respect to non-stressed conditions. In fact, when residual tension (or compression) is present in a metal, the atomic lattice spacing "d" increases (or decreases). To calculate a bi-axial (X, Y) stress – which means that the stress in direction out of plane (Z) is not described – in a point, the diffraction pattern in that point is collected for different angles of incidence "ψ". In what is commonly referred to as "sin2ψ method", the lattice distance is calculated according to the Bragg's law for each diffraction pattern recoded [133–135].The slope of the line describing the variation of the lattice distance d with sin2ψ – see Figure 35 - is related to the stress causing the deformation and the residual stress can be calculated.

4.1.1.4.1   Residual Stress in the Reference Weld

XRD has been used on a section of the weld to measure the residual stress in the weld and in the parent material. The information about the residual stress in the parent material will be used for the generation of the simulated microstructures with the Gleeble machine. In fact, this instrument allows not only to apply a variety of thermal histories to the alloy, but also to apply a stress – compressive or tensile – during the solidification. The entity of the residual stress will be used as a starting point to design different stress history during the treatments, with the aim to induce microstructural changes. The sample has been cut, grinded and polished with diamond paste. A further polishing with OP-S has been performed for 45 minutes in order to relief part of the mechanical stress caused by the surface preparation, which tends always to leave compressive stress in the near-surface layers. The diffraction patterns has been produced with a Proto18 diffractometer and then analysed with the ProtoXRDWin software. Because of the different interplanar spacing, patterns for the austenite and the ferrite have been formed separately using different X-rays sources, namely Mn, (λ=2.103) for austenite and Cr (λ= 2.291) for ferrite [135].
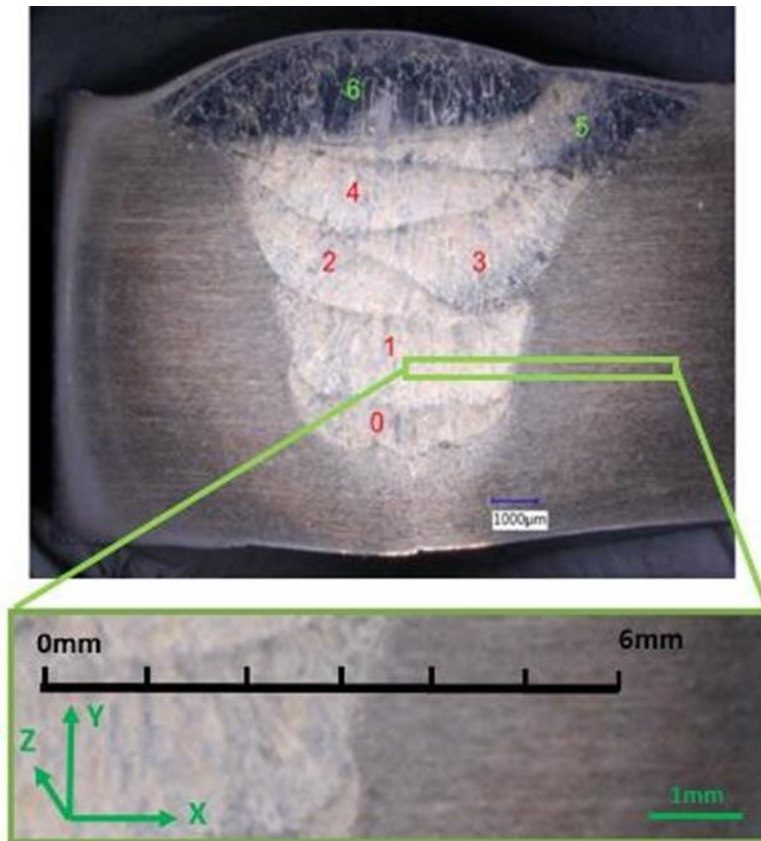
Figure 36 - Detail of the points used for the residual stress estimation with XRD. Stress is expressd with respect to the direction system reported in this picture.

With this set-up, the diffraction patterns have been produced for seven points across a 6mm long line with a 1mm spacing between each point. Points start from the centre of pass "1" and extend to the parent material – see Figure 36. The aim of these measurements was to compare the residual stress in a weld and in the parent material, so the measurement follow a line from the centre of the weld in pass "1" to the parent material. For each point, the diffraction pattern are collected for both for the (X,Z) and the (Y,Z) plans, which means that residual stress can be calculated in the X and Y direction – which are described in Figure 36.

The points in the right part of the graphs in Figure 37 and Figure 38 – 4, 5 and 6 millimetres – describe the residual stresses in the parent material – which, according to the micrographs produced, is rolled in the X direction. In the Y direction, for this region, the

stress in the ferrite and in the austenite is complementary and balanced, with residual tensile stress in the ferrite and compressive in the austenite. Among the rolling direction X, residual stress in the austenite seems to be null in the austenite while a compressive state of stress is measured in the ferrite. The measurements inside the weld are less consistent. Namely, the error bars in some point are comparable or even bigger than the actual calculated intensity – making many of the values comparable to zero – and some other values are below the accuracy of the technique itself (100 MPa). On average, it seems that the multi-pass welding, where a welding pass is subject to multiple thermal cycles, leave a microstructure with less mainly compressive residual stress.
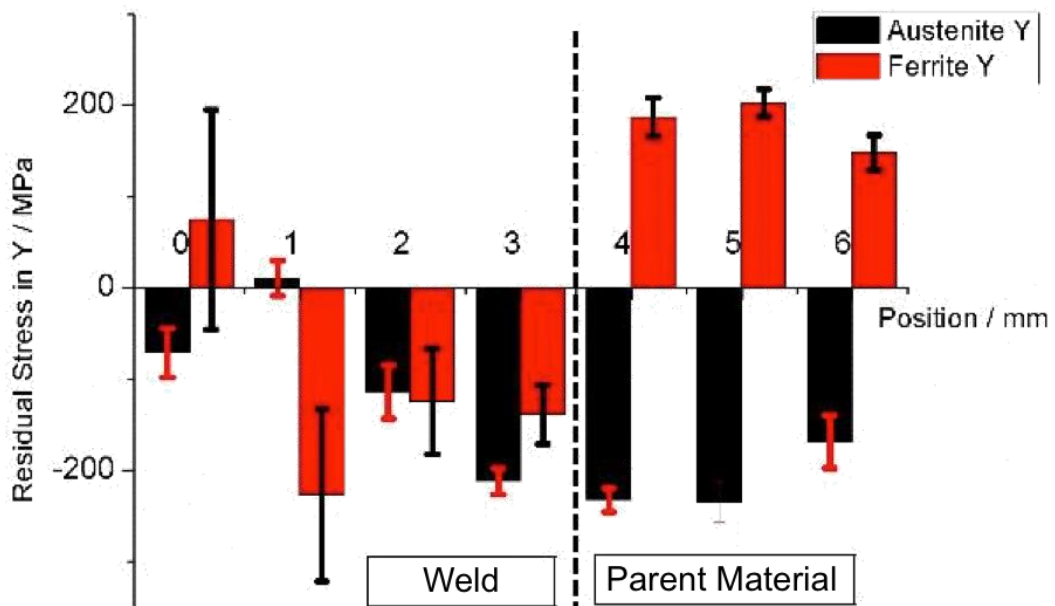
Figure 37 - Residual stress in austenite (black) and ferrite (red) in the weld and in the parent material.
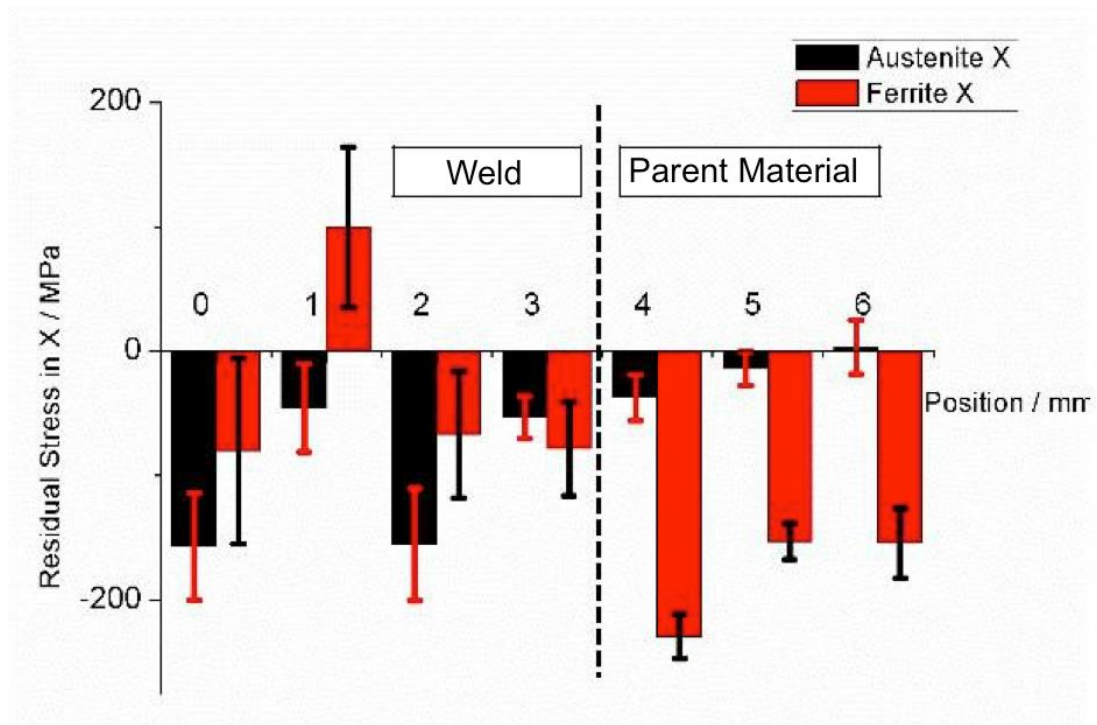
Figure 38 - Residual stress in austenite (black) and ferrite (red) in the weld and in the parent material.

The plots suggest that in the X direction, a shift from the general compression state in the parent material and an almost stress-free microstructure in the weld occurs in the heat-affected zone. The HAZ experiences high temperatures, with a maximum peak of 1300-1350°C. Further, the microhardness measurements have indicated a reduction in the hardness of this region, while optical micrographs show growth of the ferrite grains in the HAZ, with reduction of the austenite content. This information suggest that the compressive stress in the ferrite and the thermal stress from the welding process and the melt solidification, are balanced in the HAZ by the dynamic recrystallization of the ferrite grains, even though this aspects need further observations. An extensive mapping of the ferrite grains size in the HAZ will be possible with the EBSD maps, while the reduction in hardness- which is expected as a consequence of the reduction in dislocations and other defects due to the recrystallization – will be confirmed with nanohardness map in the same region.

4.1.1.5 Conclusions

The welding procedure used for the production of the reference weld had peculiar requirements, aimed to provide an HAZ microstructure comparable with the thermo-mechanical simulation that have been used in other parts of the project.

The resulting weld showed significant defects, with the incomplete closure of the weld root being the most notable. The samples used throughout the project were cut in order to avoid this region of the weldment.

The thermal parameters were selected with the intention to avoid sigma- and chi-precipitation. The absence of tertiary phases was verified on the tensile samples used in the project by means of optical microscopy on polished samples and, where possible, EBSD.

4.2 Manuscript 1 – "Effect of Large Heat Inputs on the Austenite Morphology in Gleeble Simulated Heat Affected Zones"

Journal proposed: Welding in the World

P. Reccagni[a], Q. Lu[b], M. Gittos[b], D.L. Engelberg[a]

a Corrosion and Protection Centre, University of Manchester, UK

b The Welding Institute TWI, Cambridge, UK

4.2.1 Abstract

Duplex stainless steels (DSSs) , characterized by a microstructure with equal fractions of austenite and ferrite, are widely used for structural applications in the oil and gas industry, where high strength and corrosion resistance are required. Arc welding is often used for joining large structures, such as the pipelines; the process affects the microstructure morphology and the composition of the duplex alloy, reducing the SCC resistance in the heat affected zone (HAZ) of the weld. This paper addresses the influence of arc welding on the austenite morphology in the HAZ.

Thermo-mechanical simulations of the HAZs corresponding to single-pass welds performed using different heat inputs (HI) have been produced using a GLEEBLE3500 furnace. Austenite in the HAZ has been characterized using Electron Back Scattered Diffraction (EBSD) and the fraction of grain boundary austenite (GBA), intergranular austenite (IGA) and coarse austenite grains clusters (CA) measured as a function of the HI. The results showed a significant fraction of GBA at lower heat inputs, leaving place to CA at longer cooling rates where precipitation of tertiary phases was also observed.

4.2.2 Introduction

Duplex stainless steel (DSS) grade 2205 is widely used in the energy industry because of its high strength and remarkable corrosion resistance [1-3]. The dual phase microstructure, a balanced ratio of austenite (γ) and ferrite (δ), provides this grade with outstanding resistance to environmentally-assisted cracking (EAC). Arc Welding can alter the original phase balance and produce further crystallographic phases, such as sigma (σ) and chi (χ) phases, and precipitates, for example chromium nitrides, CrN/Cr_2N [4,5].

Further, the morphology of the constituent phases in the welds heat affected zone shows great differences compared to the parent material as a result of the applied thermo-mechanical history [6,7]. This region often shows increased ferrite fraction and larger ferritic grains, while the reformed austenite is distributed as a combination of grain boundary austenite – forming at the grain boundaries between adjacent ferrite grains, GBA – and intragranular austenite – forming within individual ferrite grains, IGA [8].

The aim of this paper is to provide a description of the austenite morphology changes associated with increasingly large heat inputs in the case of single-pass TIG welds. To do so, simulated heat affected zones for different heat inputs have been produced using a GLEEBLE 3500 thermo-mechanical simulator [6,8,9] on a DSS2205 grade. Electron backscattered diffraction (EBSD) was used to characterize the microstructure in the HAZs and to quantify the fraction of different austenite types for each heat input. Chromium (II) Nitrides were observed for the larger heat inputs and their corrosion behaviour was characterized using a combination of Scanning Kelvin Probe Force Microscopy (SKPFM) and accelerated atmospheric corrosion tests.

4.2.3 Methodology

4.2.3.1 Thermal treatments

The material used was a grade 2205 duplex stainless steel ((22.0Cr, 5.1Ni, 2.48Mo, 1.77Mn, 0.022C %wt. and Fe to balance) in the form of 100 mm long cylinders with 10mm diameter EDM cut from a 40 mm thick pipe wall. The thermal cycles were applied using a GLEEBLE3500 thermo-mechanical simulator, with both the heating and the cooling performed in air. Temperature was controlled with a thermocouple spot-welded at the centre of the samples. For each treatment, the material was heated to a peak temperature of 1350 °C, with a 135 °C/s heating rate, and the peak temperature was held for 1 s. The cooling rate was varied to represent different heat input, as summarized in Table 1. The cooling intervals were calculated following the relation shown in the following equation:

Equation 1

$$\frac{Q}{d} = k(\Delta t_{8-5)})^{1/2}$$

Where Q is the heat input (kJmm^{-1}) d is the plate thickness (mm), and k is the thermal coefficient (25.52 Jmm^{-2}s$^{-1/2}$ for DSSs). Three values of H.I. were used, namely 1, 1.5 and 2 kJ/mm.

Table 1 - Cooling intervals used to simulate the HAZ of welds with different heat inputs.

$\Delta t_{1200/800}$ (s)	$\Delta t_{800/500}$ (s)	Heat Input (kJ/mm)
11.5	20	1
23	40	1.5

40	70	2

The purpose of the simulations is to investigate austenite evolution approaching the upper limit of acceptable heat inputs for duplex. To do so, the CCT curves for sigma and chi precipitation were calculated with JMatPro® and the treatments selected to reproduce both precipitates free microstructures and a microstructure with potential chi precipitation. The CCT curves for sigma and chi formation are shown in Figure 39, where the applied thermal treatments are also shown for reference.
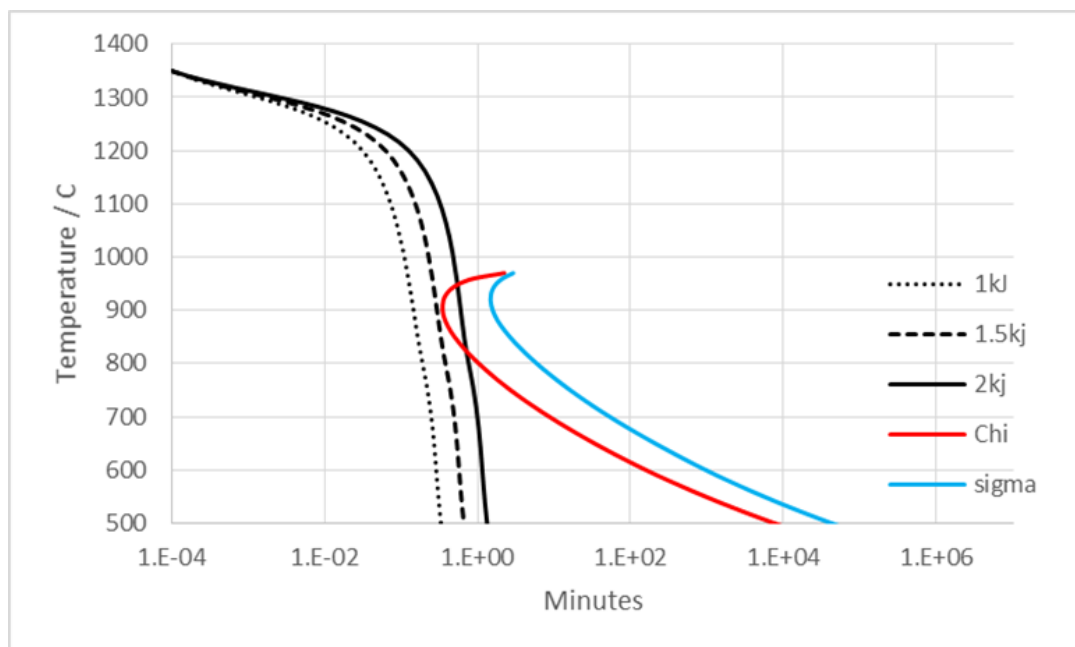
Figure 39 - Cooling profiles of the simulated heat affected zones and CCT curves for sigma and chi phases formation (1% fraction).

4.2.3.2 Microstructure Characterization

The microstructure of the as-received (AR) and treated samples has been characterized by means of Optical Microscopy (OM) and Electron Back-Scattered Diffraction (EBSD). Samples have been cut and wet-ground with silicon carbide papers (up to 4000 grit) and polished with diamond paste (up to 0.25um) followed by 30 minutes fine polishing in OP-S alkaline

colloidal silica solution from Struers (20-40 nm particles size, 45 minutes). EBSD maps have been produced in a FEI Sirion FEG-SEM (Field emission gun scanning electron microscope) equipped with a HKL Nordlys EBSD detector from Oxford instruments, using 500nm step size and 20kV accelerating voltage, over a 0.6 x 0.6 mm area. Data were analysed with HKL Channel 5 software from Oxford instrument. Semi-quantitative EDX (Energy-Dispersive X-Rays spectroscopy) measurements of the individual phases chemical composition were performed in a Zeiss Sigma VP FEG-SEM equipped with a X-Max SDD (Silicon Drift Detector) EDX detector with a 150mm2 window from Oxford Instruments. 15 Spectra for each phase (106counts) were acquired in different locations of the sample at 15kV accelerating voltage.

4.2.3.3 Austenite Morphologies

Different austenite morphologies have been grouped in three categories according to their relation with the neighbour ferrite grains. I) Intragranular austenite (IGA) has been defined as austenite plates grown within an individual ferritic grain;ii) Grain boundary austenite (GBA) was the name used for elongated austenite plates growing continuously along a ferrite:ferrite boundary and separating completely the two grains;iii) Coarse austenite (CA) was the name used for larger austenite plates growing across multiple ferrite grains and not following any specific grain boundaries. An example of this classification is reported in Figure 40 where the austenite is shown in red and the ferrite in IPF colours.

In order to quantify the fraction of each type, a modified version of the points counting technique has been used. A 11x11 points squared grid was overlapped on the EBSD maps allowing for unbiased identification of the austenite type, due to the crystallographic information on the surrounding ferrite.
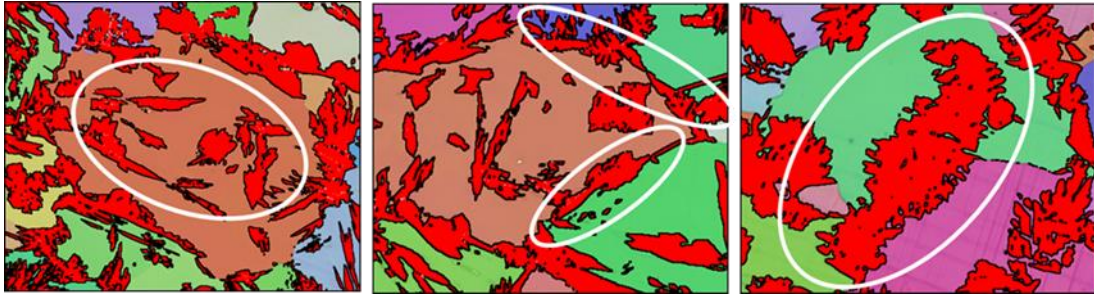
Figure 40 - Examples of the classification proposed using the EBSD maps. To enhance the contrast, austenite phase is shown in solid red and ferrite grains in IPF colours.(A) intragranular austenite (IGA), (B) grain boundary austenite (GBA) and (C) coarse austenite (CA).

4.2.3.4 Precipitates Characterization

Sign of precipitates at the ferrite:ferrite boundaries in the 1.5kJ/mm and 2kJ/mm treatments were investigated. Elemental analysis was performed using low-voltage (2kV) windowless EDX; spectra were acquired in a Zeiss Merlin FEG-SEM equipped with a X-Max Extreme detector from O.I. SKPFM Volta-potential surveys were used to inform on the relative nobility of the precipitates; map were acquired using a Dimension D3100 AFM from Brucker with OSCM-PT Platinum coated tips (<25nm tip radius). Data were analysed using Nanoscope v1.5 software, from Bruker.

Atmospheric corrosion under chloride bearing deposits has been used as a corrosion test to correlate the relative nobility information gathered with SKPFM with performance in a specific corrosion environment of practical interest. The samples, ground and polished (up to 0.25 um) have been exposed for 48 hours to droplets (1 µL) of 0.1M $MgCl_2$, resulting in a deposition density of 400 µg/cm2. The samples were kept for two days in a furnace at 80 °C enclosed in an air-tight container with a reservoir of saturated $MgCl_2$, providing approximatively 30% relative humidly (i.e. the deliquescence humidity of $MgCl_2$). After exposure, the samples have been washed with deionized water and then polished for 15 minutes with OP-S colloidal silica solution. SEM micrographs have been used to

characterize the corrosion attack and EDX was used for phase discrimination during imaging.

4.2.4   Results

4.2.4.1 Microstructure Characterization and Austenite morphology

The EBSD phase maps for the as received material and for the three simulated HAZ are shown in Figure 41. The austenite content, as expected increased with the increasing heat input due to the longer cooling time in the 1200-900°C interval, where most of primary austenite reformation occurs.
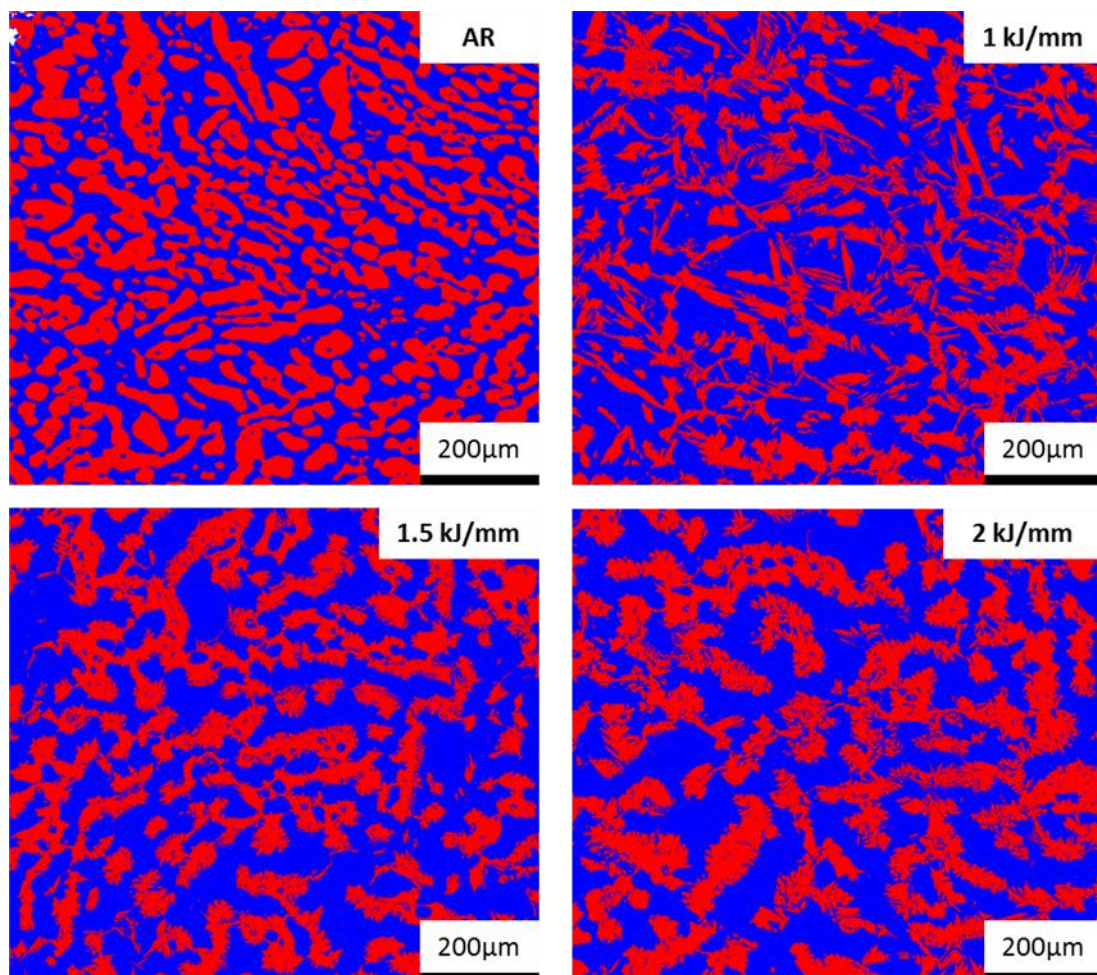
Figure 41 - EBSD phase maps for the as-recevied material and for the thermal treatments applied. Ferrite in blue, austenite in red.

The effect of the thermal treatments is also observed in the chemical composition of austenite and ferrite for the different thermal treatments. With respect to the AR metal, the partitioning of bcc and fcc forming elements in their preferential phases occurs to a lesser extent, due to the relatively fast cooling. As a result, the time spent by the alloy in the temperature regime where diffusion of substitutional alloying elements occur is shorter. This effect is more marked for the 1 kJ simulation, where the fastest cooling rate in the 1200-900 °C is applied. The results of the EDX elemental analysis are summarized in Table 7.

Table 7 - Chemical composition of austenite and ferrite for the different microstructures. ZAF corrected EDX quantification.

	FERRITE					AUSTENITE			
Wt. %	**AR**	**1 kJ/mm**	**1.5 kJ/mm**	**2 kJ/mm**	**Wt. %**	**AR**	**1 kJ/mm**	**1.5 kJ/mm**	**2 kJ/mm**
Cr	24.1 ±0.1	22.7 ±0.6	23.2 ±0.5	23.2 ±0.3	**Cr**	21.1 ±0.1	21.3 ±0.6	20.8 ±0.5	20.9 ±0.5
Mo	3.7 ±0.1	3.5 ±0.2	3.6 ±0.2	3.6 ±0.2	**Mo**	1.8 ±0.1	2.7 ±0.2	2.6 ±0.2	2.5 ±0.2
Ni	4.2 ±0.1	4.9 ±0.4	4.7 ±0.4	4.8 ±0.4	**Ni**	6.7 ±0.1	6.2 ±0.4	6.8 ±0.4	6.7 ±0.4
Mn	1.6 ±0.1	1.6 ±0.1	1.5 ±0.1	1.6 ±0.2	**Mn**	1.8 ±0.1	1.7 ±0.1	1.7 ±0.1	1.7 ±0.1

The distribution of austenite in the treated microstructures shows significant differences depending on the cooling time applied. Austenite in the 1kJ treatment is characterized by significant austenite formation at the ferrite:ferrite grain boundaries (GBA) and intragranular austenite formation (IGA). Some of the intragranular austenite, growing as side plates from the GBA, can be categorised as "widmanstaetten" austenite (see Figure

42); this particular austenite type is characterized by a Kurdjumov-Sachs orientation relationship with the surrounding ferrite and it is easily highlighted in the EBSD maps as shown in Figure 42. For the purpose of this estimation, WA has been assimilated to IGA, with the fraction of K-S boundaries for each microstructure shown in for indication.
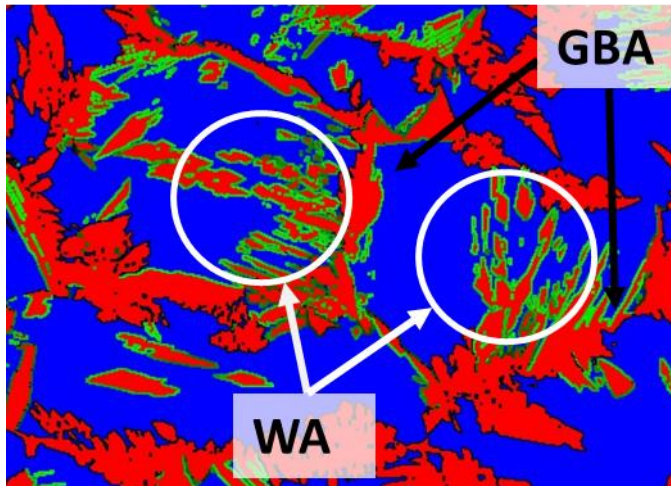
Figure 42 – K-S phase boundaries (in green) between austenite (red) and ferrite (blue) .

The 1.5 and 2 kJ/mm treatments showed a progressively reduced content of grain boundary austenite and intragranular austenite, with the relative frequency of K-S boundaries also reduced. Coarser austenite becomes the predominant form of austenite, with the larger fraction found in the 2kJ/mm microstructure. Results of the quantification are summarized in Table 8.

Table 8 - Fraction of the different types of austenite in the simulated heat affected zones.

(from EBSD)	1 kJ	1.5 kJ	2 kJ	Parent Material
Austenite:Ferrite	38:62	40:60	43:57	51:49
CA	11%	52%	62%	88%

GBA	39%	24%	15%	--
IGA	50%	24%	23%	12%
K-S rel. freq.	17%	8%	9%	5%

4.2.4.2 Precipitates

EDX elemental maps for N and Cr were acquired over the precipitates observed in the 1.5 and 2 kJ/mm microstructures. An example referred to the 1.5kJ/mm microstructure is shown in Figure 43. The SEM image shows clearly the discrete nature of these precipitates, decorating the grain boundaries between ferritic grains. The EDX quantification showed a N:Cr weight ratio of 8:92, suggesting the precipitates are Cr_2N (stoichiometric weight ratio 12:88).
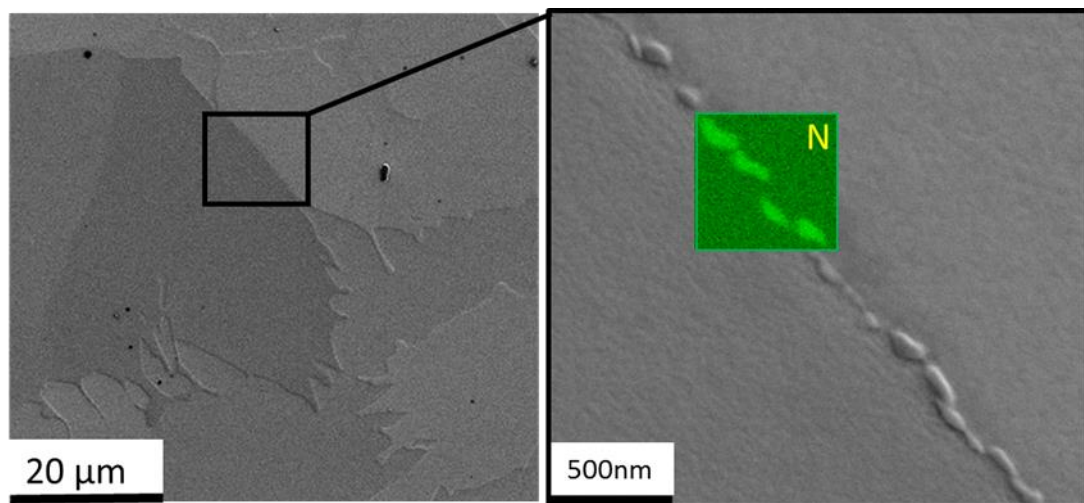
Figure 43 - SEM image of the chromium nitrides at the ferrite:ferrite grain boundaries of the 1.5kJ/mm microstructure. Low-voltage EDX elemental map of nitrogen shown in the detail.

The electrochemical character of the nitrides with respect to the surrounding ferrite and austenite was estimated using SKPFM – see Figure 44. Potential maps were acquired and the nitrides showed cathodic character with respect to the ferrite ($\Delta\Psi$ = 15-20mV). The

austenite, consistently with other works, also showed cathodic character with larger potential difference with the ferrite ($\Delta\Psi$ = 35-40mV).
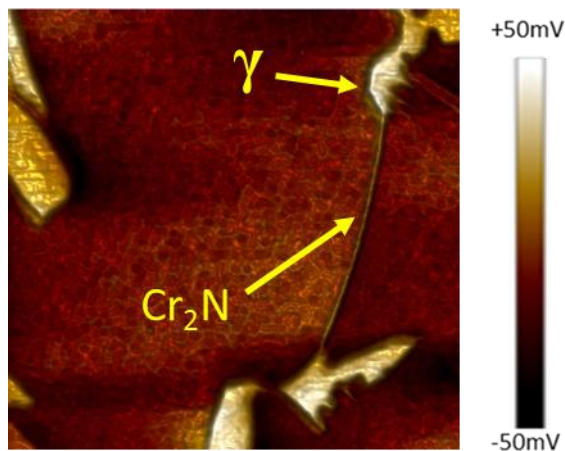
Figure 44 - SKPFM Volta-Potential map of the chromium nitrides at the ferrite:ferrite grain boundaries of the 1.5kJ/mm microstructure.

The atmospheric corrosion confirmed the anodic character of the ferrite with respect to both austenite and Cr_2N. Selective dissolution of ferrite was found in the exposed area, with the austenite confining the corrosion attack. The nitrides also showed cathodic character, with ferrite dissolution surrounding - rather than dissolving - the precipitates at the delta:delta boundaries, as shown in Figure 45.
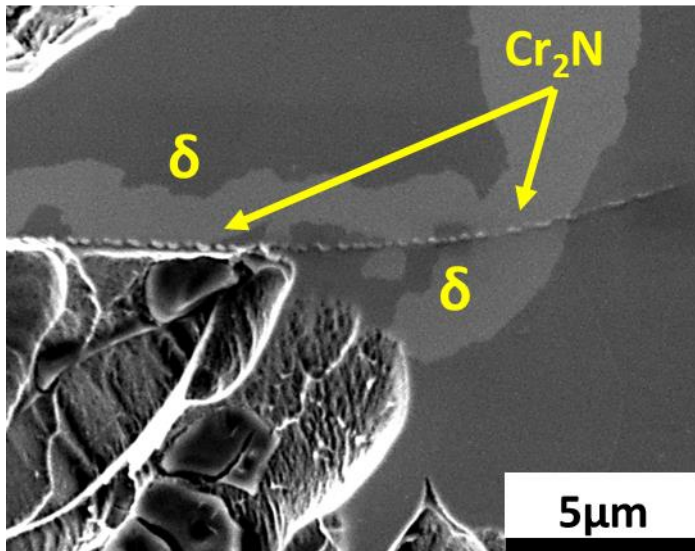
Figure 45 - Atmospheric corrosion attack on the 1.5 kJ/mm microstructure, showing the dissolution of the ferrite surrounding the chromium nitrides.

4.2.5   Discussion

In welding practise, duplex stainless steel welds are in first instance qualified upon their austenite fraction and the occurrence of tertiary phases precipitation. While reduced austenite fraction is somehow expected in the HAZ, the morphology of the austenite found is not routinely assessed [10]. Microstructure morphology, however, also has a significant impact on DSSs environment assisted cracking resistance. The phase boundaries between ferrite and grain boundary austenite, in particular, have been shown to potentially act as preferred cracking path for stress corrosion cracking [8].

GBA formation has been shown to be promoted by short cooling rates and a potential for the GBA phase boundaries to act as a preferred SCC cracking path has been reported. Large heat inputs, instead, promote coarser austenite, suggesting that the use of longer cooling time could be beneficial. Longer cooling intervals however pose a threat. Excessive cooling time can favour the formation of sigma and chi phases. This is a significant concern in multi-pass welds, where the heat affected zone is subjected to multiple re-heating during the subsequent passes [11]. The temperatures reached during re-heating are lower than

the welding peak temperatures, yet sufficient to potentially cause formation of –sigma and –chi phases. Larger heat inputs increase the time the HAZ is kept in the sigma/chi formation temperature region, explaining why also an upper limit of heat input is prescribed in welding guidelines.

This work provides a quantitative method for estimation of the phase morphology fractions in simulated heat affected zone with increasing heat input [10,12]. In particular, the main interest was exploring the changes in the microstructure that occur with the progressive transition from a GBA+IGA morphology to a CA dominated microstructure. The purpose of this work was to evaluate the effects of the thermal history alone, without changes in the chemical composition of the metal, such as nitrogen pick-up from the welding environment [13,14] and without external strain applied on the sample during heating/cooling. This is a significant difference with actual welds, where tensile stress develops in the HAZ due to the thermal history experienced by the adjacent weld pool. Tensile stress has an effect on the degree of recrystallization occurring in the microstructure [15–17], which, due to the experimental setup, was not considered in this work as the mechanical constraint was constant in all simulations. Residual stress and its partitioning in the phases are also different in the two phases upon rapid cooling, such as in the case of welding [18]. The effects of residual stress on SCC are not addressed in this work.

Detrimental effects of large heat inputs were visible already at 1.5kJ/mm heat input. While forming beneficial coarser austenite plates, this treatment caused precipitation of isothermal Cr_2N at the ferrite:ferrite phase boundaries [19-21]. The Cr_2N showed cathodic character with respect to the ferrite, potentially acting as corrosion initiation points [4].

4.2.6 Conclusions

- The formation of grain boundary austenite (GBA) is progressively reduced by increasing welding heat input;

- Widmanstatten austenite fraction in the HAZ also decreases with higher HI;

- The formation of coarser austenite plates in the simulated HAZ of a single pass weld caused formation of chromium (II) nitrides at the ferrite:ferrite phase boundaries;

- The cathodic character of the nitrides was confirmed with SKPFM and atmospheric corrosion tests;

-

4.2.7 References

[1]   R.N. Gunn, Developments, grades and specifications, Duplex Stainl. Steel. Microstruture, Prop. Appl. (1997) 1–13. doi:10.1533/9781845698775.1.

[2]   R.A. Cottis, R.C. Newman, Stress Corrosion Cracking Resistance of Duplex Stainless Steels, Health and Safety Executive - Offshore Technology Report, 1993.

[3]   F. King, Corrosion Resistance of Austenitic and Duplex Stainless Steels in Environments Related to UK Geological Disposal, A Report to NDA RWMD, (2009) 1–58.

[4]   E. Bettini, U. Kivis??kk, C. Leygraf, J. Pan, Study of corrosion behavior of a 22% Cr duplex stainless steel: Influence of nano-sized chromium nitrides and exposure temperature, Electrochim. Acta. 113 (2013) 280–289. doi:10.1016/j.electacta.2013.09.056.

[5]   E. Bettini, U. Kivisäkk, C. Leygraf, J. Pan, Study of corrosion behavior of a 2507 super duplex stainless steel: Influence of quenched-in and isothermal nitrides, Int. J. Electrochem. Sci. 9 (2014) 61–80.

[6]   R.-I. Hsieh, H.-Y. Liou, Y.-T. Pan, Effects of Cooling Time and Alloying Elements on the Microstructure of the Gleeble-Simulated Heat-Affected Zone of 22% Cr Duplex Stainless Steels, J. Mater. Eng. Perform. 10 (2001) 526–536. doi:10.1361/105994901770344665.

[7]   H.Y. Liou, R.I. Hsieh, W.T. Tsai, Microstructure and pitting corrosion in simulated heat-affected zones of duplex stainless steels, Mater. Chem. Phys. 74 (2002) 33–42. doi:10.1016/S0254-0584(01)00409-6.

[8]   H.-Y. Liou, R.-I. Hsieh, W.-T. Tsai, Microstructure and stress corrosion cracking in simulated heat-affected zones of duplex stainless steels, Corros. Sci. 44 (2002) 2841–2856. doi:10.1016/S0010-938X(02)00068-9.

[9]   Y. Guo, T. Sun, J. Hu, Y. Jiang, L. Jiang, J. Li, Microstructure evolution and pitting corrosion resistance of the Gleeble-simulated heat-affected zone of a newly developed

lean duplex stainless steel 2002, J. Alloys Compd. 658 (2016) 1031–1040. doi:10.1016/j.jallcom.2015.10.218.

[10]   BS-EN-ISO, Specification and qualification of welding procedures for metallic materials — Welding procedure test —, (2012) 1–32.

[11]   R.N. Gunn, Welding metallurgy, in: Duplex Stainl. Steels, w, Abington, England, 1997: pp. 110–132. doi:10.1533/9781845698775.110.

[12]   J. Verma, R.V. Taiwade, Effect of welding processes and conditions on the microstructure, mechanical properties and corrosion resistance of duplex stainless steel weldments—A review, J. Manuf. Process. 25 (2017) 134–152. doi:10.1016/j.jmapro.2016.11.003.

[13]   Z. Zhang, H. Jing, L. Xu, Y. Han, L. Zhao, C. Zhou, Effects of nitrogen in shielding gas on microstructure evolution and localized corrosion behavior of duplex stainless steel welding joint, Appl. Surf. Sci. 404 (2017) 110–128. doi:10.1016/j.apsusc.2017.01.252.

[14]   P. Sathiya, S. Aravindan, R. Soundararajan, a. Noorul Haq, Effect of shielding gases on mechanical and metallurgical properties of duplex stainless-steel welds, J. Mater. Sci. 44 (2008) 114–121. doi:10.1007/s10853-008-3098-8.

[15]   R. Badji, B. Bacroix, M. Bouabdallah, Texture, microstructure and anisotropic properties in annealed 2205 duplex stainless steel welds, Mater. Charact. 62 (2011) 833–843. doi:10.1016/j.matchar.2011.06.001.

[16]   R.D. Doherty, D. a. Hughes, F.J. Humphreys, J.J. Jonas, D. Juul Jensen, M.E. Kassner, W.E. King, T.R. McNelley, H.J. McQueen, a. D. Rollett, Current issues in recrystallization: A review, Mater. Today. 1 (1998) 14–15. doi:10.1016/S1369-7021(98)80046-1.

[17]   W. Reick, M. Pohl, A.F. Padilha, Recrystallization-Transformation Combined Reactions during Annealing of a Cold Rolled Ferritic-Austenitic Duplex Stainless Steel., ISIJ Int. 38 (1998) 567–571. doi:10.2355/isijinternational.38.567.

[18]   J.M. Cabrera, A. Mateo, L. Llanes, J.M. Prado, M. Anglada, Hot deformation of duplex stainless steels, J. Mater. Process. Technol. 143–144 (2003) 321–325. doi:10.1016/S0924-0136(03)00434-5.

[19]   A.J. Ramirez, S.D. Brandi, J.C. Lippold, Secondary austenite and chromium nitride precipitation in simulated heat affected zones of duplex stainless steels, Sci. Technol. Weld. Join. 9 (2004) 301–313. doi:10.1179/136217104225021715.

[20]   V.A. Hosseini, K. Hurtig, L. Karlsson, Effect of multipass TIG welding on the corrosion resistance and microstructure of a super duplex stainless steel, Mater. Corros. 68 (2017) 405–415. doi:10.1002/maco.201609102.

[21]   N. Sathirachinda, R. Pettersson, S. Wessman, J. Pan, Study of nobility of chromium nitrides in isothermally aged duplex stainless steels by using SKPFM and SEM/EDS, Corros. Sci. 52 (2010) 179–186. doi:10.1016/j.corsci.2009.08.057.

4.3 Manuscript 2 – "Reduction of Austenite-Ferrite Galvanic Activity in the Heat-Affected Zone of a Gleeble-simulated grade 2205 Duplex Stainless Steel (DSS) Weld"

P. Reccagni[a,*], L.H. Guilherme[b], Q. Lu[c], M. F. Gittos[c], D.L. Engelberg[a]

[a] Corrosion and Protection Centre, University of Manchester, UK

[b] Engineering Department, Soudap Engineering Company, Araraquara, SP, Brazil

[c] TWI, Cambridge, UK

*Corresponding author. Email address: pierfranco.reccagni@postgrad.manchester.ac.uk, pierfranco.reccagni@gmail.com

4.3.1 Abstract

Duplex stainless steels (DSSs) have outstanding resistance to stress corrosion cracking (SCC), provided by their peculiar microstructure consisting of two phases with different chemical composition and electrochemical nobility. Arc welding is often used for joining large structures, such as the pipelines; this process affects the microstructure morphology and the composition of the duplex alloy, reducing the SCC resistance in the heat affected zone (HAZ) of the weld. This paper addresses the influence of arc welding on the galvanic activity between the main constituent phases in the HAZ.

Changes in galvanic activity are measured on a 2205 DSS grade as-received and after thermo-mechanical simulation of a single weld pass, reproducing the microstructural changes typical of the HAZ. The relative nobility of the two phases in both conditions is measured using scanning kelvin probe force microscopy (SKPFM-AFM) and using electrochemical polarization in 2M H_2SO_4 + 0.5M HCl electrolyte, which has the property of showing ferrite and austenite passivation peaks individually in the polarization curves.

Results show a marked reduction in electrochemical nobility difference between the two phases in the simulated HAZ, which contributes to explain the reduced resistance to stress corrosion cracking of this region.

4.3.2 Introduction

Duplex stainless steels (DSSs) have been increasingly used in the energy and chemical industries due to their excellent combination of mechanical strength and corrosion resistance, with far superior stress corrosion cracking (SCC) performance in chloride-containing environments than comparable austenitic grades [1,2] . The properties of DSSs rely on a microstructure with equal proportions of γ-austenite and δ-ferrite [3]. The partitioning of austenite-forming (Ni, N) and ferrite-forming (Cr, Mo) elements results in different chemical compositions and corrosion properties for the two phases [3,4]. The consequent galvanic activity between austenite and ferrite is recognised as a key property for the SCC resistance of DSSs, with the ferrite cathodically protecting the austenite in acidic, chloride-containing environments [5].

Arc welding is widely used to join and fabricate structures via fusion welding processes [6]. As a consequence of the welding process, the heat-affected zone (HAZ) surrounding DSSs welds normally shows an increased ferrite fraction and the compositions of the two phases are modified with respect to those in the base metal [7]. Due to the microstructural changes, this region of the weld shows increased susceptibility to localised corrosion and SCC [8]. Even when an acceptable phase balance is achieved and third phase (e.g. σ-sigma, χ-chi, $Cr_{1,2}N$) precipitation is avoided [7,9], a better understanding of the SCC susceptibility in the HAZ is required [10].

The effect of welding on the austenite-ferrite galvanic activity in the HAZ is investigated in this work. A microstructure representative of an HAZ was produced using thermo-mechanical simulation and the HAZ microstructure was characterized with energy-dispersive X-ray (EDX) spectroscopy and electron backscatter diffraction (EBSD). Changes in

110

austenite:ferrite galvanic activity caused by the applied thermal treatment were investigated by measuring the Volta-Potential difference of the two phases using scanning Kelvin probe force microscopy (SKPFM) [11,12]. Measurements showed that the two phases reached closer surface potential values in the HAZ. The passivation behaviour of the individual phases in the wrought alloy and the simulated HAZ was also investigated, using electrochemical potentiodynamic polarization in an H_2SO_4/HCl electrolyte [13,14].

4.3.3   Methodology

The wrought material used was a solution annealed DSS grade 2205 (UNS S1803) in the form of a pipe (38mm wall thickness) with chemical composition (in %wt.) of 22.0Cr, 5.1Ni, 2.48Mo, 1.77Mn, 0.022C and Fe (bal). Cylindrical samples (100mm length and 10mm diameter) were extracted longitudinally from the pipe wall, by EDM cutting, and a thermal treatment to produce a simulated HAZ was applied using a GLEEBLE3500 thermo-mechanical simulator. The simulation was designed to correspond to the HAZ of a single-pass TIG weld made at a heat input of 1.0kJ/mm and was performed by heating the sample to 1350°C for 2 seconds followed by controlled cooling [15] the cooling rate was selected to avoid formation of sigma and chi phases, for which CCT curves were produced using JMatPro® - see Figure 46.
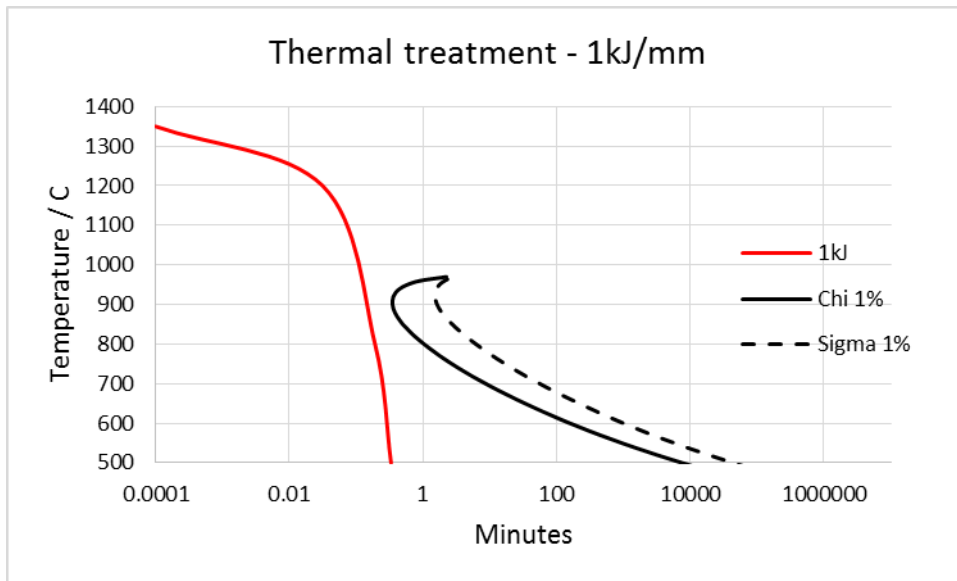
Figure 46 - Thermal history of the simulated HAZ (red) with 1% Sigma and Chi theoretical CTT curves.

The wrought material, which was in a solution annealed condition (i.e. as-received (AR)), and the material subjected to thermal simulation (i.e. the simulated HAZ) were cut into 10mm diameter coupons and mounted in conductive epoxy resin. After wet-grinding to 2400 grit, diamond paste polishing to 1 µm and colloidal silica finishing (20-40nm, 30 minutes), the microstructure was characterized using EBSD. Maps with a typical dimension of 1.0mm x 0.8mm were acquired using 600nm step size in a FEI Quanta 650 FEG-SEM equipped with a Nordlys EBSD detector from Oxford Instruments. The data were processed using HKL Channel 5 software from the same manufacturer. EDX data for local chemical compositions were acquired using X-Max detector of $80mm^2$, collecting 10^6 counts for each point. EDX spectra were quantified using Aztec software for ZAF correction. In the wrought material (AR), 5 spectra were acquired for each phase. In the simulated HAZ, where the chemical composition shows larger local variations, 30 spectra were collected.

The same surface preparation was used for Volta-Potential surveys. Measurements were performed in a Dimension D3100 AFM, using platinum-coated tips (OSCM-PT) with 25nm tip radius. Measurements were performed in amplitude modulation with 50nm scan lift height and maps were acquired over 80µm X 80µm regions at 0.2kHz scan frequency,

112

acquiring 512 lines per scan and 512 points per line, giving a theoretical resolution of approximatively 150nm per pixel. Measurements were performed at room temperature and humidity.

The same materials (i.e. the wrought alloy and the simulated HAZ) were used for electrochemical measurements. The surfaces were prepared by wet grinding to a 1200 grit finish followed by cleaning in ethanol and de-ionized water. A custom-built three-electrode miniature set-up was used in a micro-cell, as described elsewhere [16], with an exposed circular region of 1.5mm diameter (1.77mm^2 area) and a solution volume in the cell of 3ml. All measurements were performed at room temperature using an Ag/AgCl reference electrode and a Ivium Compactstat.e potentiostat. The electrolyte used was 2M H_2SO_4 + 0.5M HCl [17] and the scan rate used was 0.1mV/s.

4.3.4 Results

4.3.4.1 Microstructure

Phase maps of the AR and the simulated HAZ microstructures are shown in Figure 47. The austenite:ferrite ratio in the AR sample was 51:49 while in the simulated HAZ sample the austenite content was reduced and the phase ratio was 38:62. Sigma and chi phases were not observed.
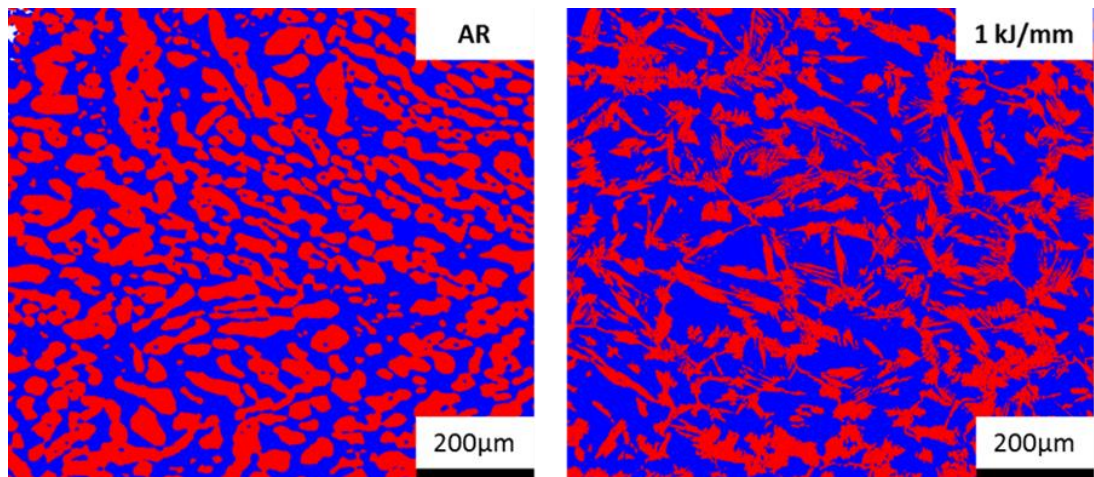
Figure 47 - EBSD phase maps of base metal (a) and simulated HAZ (b). austenite in red, ferrite in blue

An expected consequence of the thermal treatment is the change in chemical composition of austenite and ferrite. While isothermal annealing enables redistribution of austenite and ferrite-forming elements to the respective favoured phases, the fast cooling cycle in the HAZ inhibits this re-distribution. In particular, the differences in Cr, Mo, Ni and Mn contents between austenite and ferrite become smaller. Further, spectra acquired in different grains show larger composition variance in the HAZ, as summarized in Table 9.

Table 9 - Chemical compositions of the phases in the wrought metal and simulated HAZ (EDX ZAF corrected).

Element/ PREN formula	Average EDX analyses, normalised wt% (SD)					
	Wrought metal			Simulated HAZ		
	Ferrite	Austenite	Difference between phases	Ferrite	Austenite	Difference between phases
Cr	24.1 (<0.1)	21.1 (<0.1)	3	22.7 (0.6)	21.3 (0.6)	1.4
Mo	3.7	1.8 (<0.1)	1.9	3.5 (0.2)	2.7 (0.2)	0.8

	(<0.1)				
Ni	**4.2** (<0.1)	**6.7** (<0.1)	**2.5**	**4.9** (0.4)	**6.2** (0.4)	**1.2**
Mn	**1.6** (<0.1)	**1.8** (<0.1)	**0.2**	**1.6** (0.1)	**1.7** (0.1)	**0.1**

SD = standard deviation

Of particular interest is the variation of Cr and Mo concentrations in the two phases. Ferrite is depleted in both elements in the HAZ, with Cr reduced by 1.4% and Mo by 0.2%. Conversely, HAZ austenite shows higher contents of both SKPFM measurements

Volta potential (Ψ) measurements were used to investigate the change in galvanic activity between austenite and ferrite on a local scale. A map of the wrought base metal (BM) was compared with four maps from different locations of the simulated HAZ. A set of typical maps is given in Figure 48, where line scans measuring the volta-potential difference between austenite and ferrite ($\Delta\Psi_{\gamma:\delta}$) are also shown.
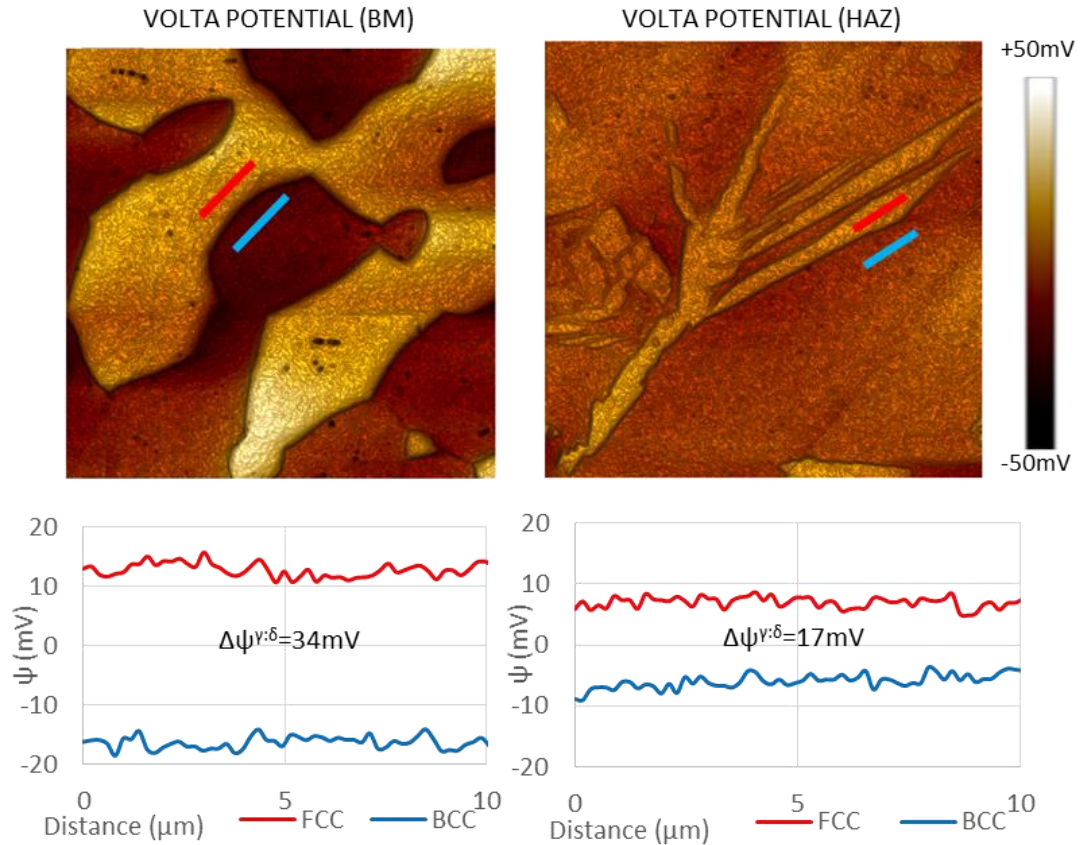
Figure 48- SKPFM measurements on the wrought metal/base metal (BM) (left) and the simulated HAZ (right) with a corresponding heat input of 1.0kJ/mm. From top to bottom: height map, Volta-Potential map, example of line scans in austenite (red) and ferrite (blue).

In order to avoid effects of the different austenite:ferrite ratios on the measured potential difference in the two microstructures, the potential has been measured within the individual phases using the average value of 10μm long line scans. An example of these measurements can be seen in Figure 48. Line-scan measurements showed a great variation across different positions within individual phases, reflected in the standard deviation (SD) of the average values. Measurements were acquired for each map in five different positions for both austenite and ferrite. While austenite in both conditions showed consistently cathodic character with respect to ferrite, the average austenite-ferrite Volta potential difference was found to be reduced in the simulated HAZ. The average difference found in the wrought/base metal sample was 47mV, while an average value of 24mV was

measured in the four maps acquired from the HAZ. The results of the austenite-ferrite Volta potential difference on the simulated HAZ have been normalized with respect to the difference in the wrought/base metal, and the decreased galvanic activity expressed as fraction of the value of the wrought/base metal. The results are summarized in Table 10. The measurements showed consistently that the potential contrast between the two phases was reduced in the simulated HAZ, showing a potential difference of approximately 50% of that measured in the base metal.

Table 10 - Summary of the SKPFM Volta-Potential measurements.

$\Delta\psi^{\gamma:\delta}$		$\dfrac{\Delta\psi_{HAZ}^{\gamma:\delta}}{\Delta\psi_{BM}^{\gamma:\delta}} x100$
Base Metal	Simulated HAZ	
47 (SD 4.4) mV	24 (SD 2.3) mV	51 %
	26 (SD 3.5) mV	55 %
	22 (SD 4.1) mV	47 %
	24 (SD 2.1) mV	51 %

4.3.4.2 Polarization Test in H2SO4 + HCl

Polarization scans were initially performed over a wide potential range in order to identify the locations of the austenite and ferrite activation peaks. Scans were then carried out over a narrower potential range, focusing on the activation peaks. The potential range selected was from -50mV vs. OCP to -100mV and the results are shown in Figure 49.
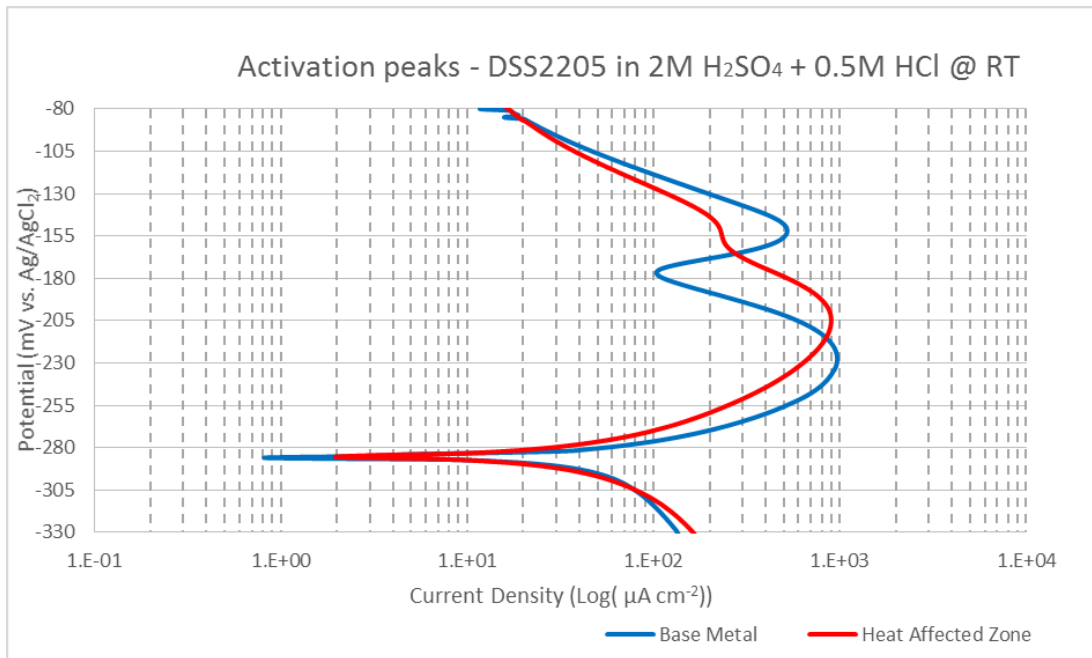
Figure 49 - PTD polarization curves in the activation region. Wrought/base metal in blue, simulated HAZ in red.

The activation peaks for austenite and ferrite were clearly separated and easy to identify for the wrought/base metal sample. In the simulated HAZ, the activation peaks for ferrite were still easy to identify. The activation curves for austenite, instead, were partially hidden or, in other words, the activation curves for the two phases were not completely resolved. While the activation peaks for austenite in the HAZ were not evident, both times the polarization curves showed a change of trend in the region corresponding to the austenite activation.

In order to highlight the austenite contribution in the activation curve for the HAZ, gaussian deconvolution of the peaks has been performed. Reasonable fitting of the activation curve was possible including a second activation curve accounting for the austenite dissolution – see Figure 50.
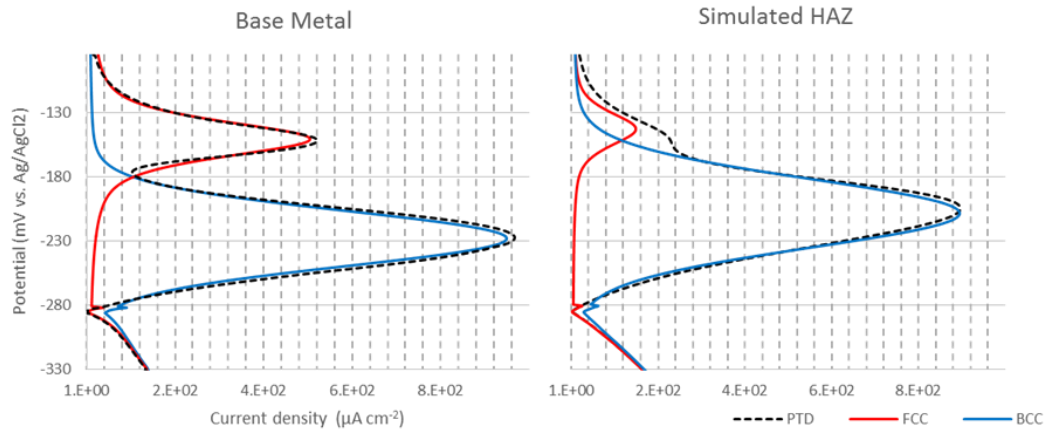
Figure 50 - Deconvolution of the PTD polarization curve in the activation regions for the wrought/base metal (left) and the simulated HAZ (right). Austenite activation curves in red, ferrite in blue.

The difference between austenite and ferrite passivation potential was 80mV in the wrought/base metal, while this difference reduced to 60mV in the simulated HAZ. Despite this variation in passivation behaviour of the two phases, in both measurements the free corrosion potential was found to be unchanged (-285mV) with or without the applied heat treatment. Another difference observed was the difference in relative current contribution of austenite and ferrite to the global activation current. Integration of the polarization curve in the activation region showed similar values of charge for the alloy components oxidation for both materials of ≈50μC. However, while in the wrought base metal 76% of the charge was provided by the ferrite and 23% from the austenite, in the simulated HAZ ferrite oxidation contributed for 92% of the total activation current, while austenite contribution was reduced to 8%. Two factors are likely to have caused this change in the simulated HAZ. In first place, the ferrite fraction in this microstructure is higher: 62% in the simulated HAZ compared to 49% in the wrought base metal. Secondly, the differences in the Cr and Mo contents of the two phases is reduced compared with respect to the wrought base metal, potentially causing changes in the electrochemical passivation reactions.

4.3.4.3 Discussion

DSS welds show the high susceptibility to SCC in the HAZ. One of the most noticeable consequences of the welding process on this region is the reduction of austenite content. SCC resistance of DSSs is greatly affected by the phase ratio, with values approaching the ideal 50:50 distribution showing the best performance [19]. The thermal treatment experienced in the HAZ causes several alterations in the alloy microstructure. Even when acceptable phase balance is achieved, the chemical composition for austenite and ferrite in the HAZ shows great variation with respect to individual phase composition in the wrought alloys in the annealed state.

Within the HAZ, partitioning of the austenite and ferrite-forming elements between the phases is reduced compared to the wrought base metal, due to the initial transformation to ferrite of the microstructure and the relative fast cooling that allows diffusion of heavy elements only over a short distance (i.e. a few microns) [20]. As a result, the chemical compositions of the austenite and the ferrite become more similar, with marked reduction of chromium content in the latter. Similar findings have been reported by [21], who also correlated the chromium depletion of the ferrite with enhanced localised corrosion susceptibility in this phase.

The different corrosion properties of austenite and ferrite are of paramount importance for the outstanding SCC resistance of DSSs. In modern grades, in which austenite is present in the form of dispersed islands and ferrite is the continuous phase, cracking in chloride-containing environments initiates in the latter. The ability of austenite to stop the crack progression relies on its higher corrosion potential. When a crack in ferrite reaches an austenite island, the anodic activity at the crack tip is suppressed by the difference potential/pH conditions required for austenite to corrode [19]. The different condition required for austenite corrosion forces the crack to stop, unless ductile tearing or

(hydrogen) embrittlement of austenite occurs. For this protective mechanism to work, a difference in chemical composition, resulting in different corrosion potentials for the two phases, is needed.

While the change in ferrite composition and its higher susceptibility to localised corrosion can explain the increased likelihood of crack nucleation sites in this phase, clarifying the relation with SCC susceptibility requires an understanding of changes in the global electrochemical properties of the thermally altered alloy (i.e. the simulated HAZ in the current study). In particular, the evolution of austenite and ferrite relative nobility could give an indication on the mechanism behind the reduced SCC resistance of the HAZ. The SKPFM measurements and the electrochemical polarization in chloride-containing environments constitute two different ways to investigate the quality and the formation of the passive film on austenite and ferrite in the different microstructures.

The Volta-Potential difference highlights the relative nobility of the austenite-ferrite native passive films. The passivation of the alloys in this case occurs in air, once the polishing is completed, and the potential measured relates to the native passive film, after 2 days ageing at ambient temperature and humidity. These observations reveal the localised passive film nobility and show the Volta-Potential difference of austenite and ferrite as an intrinsic property of the two phases. These measurements are not influenced by the different phase ratios in the wrought base metal and in the HAZ, and they are independent from the austenite morphology and distribution. As a result, the reduction in Volta-Potential difference of the phases in the HAZ is a direct consequence of the different chemical composition of the two phases after the thermal cycle applied by the welding process.

Potentiodynamic polarization was used to understand the consequences of these changes on the global electrochemical behaviour of the alloy. When using the mixture of sulphuric

and hydrochloric acid, the difference in electrochemical nobility between austenite and ferrite results in the existence of two distinct anodic peaks in the active-to-passive region of the polarization curve, with the austenite activation potential being higher than that of ferrite. In the simulated HAZ, this effect is reduced, due to the similar chemical composition of the two phases upon the thermal treatment. With the increased ferrite content, the activation peak for this phase occupies a larger area of the active-to-passive region in the potentiodynamic curve. As a result, the austenite activation peak is hidden and deconvolution is needed to identify it. The electrochemical potential difference between the phases (i.e. activation peaks) is smaller in the HAZ, confirming that the reduction in relative nobility of the two phases is determined by the different passivation mechanism of the microstructure in the two conditions.

4.3.5   Conclusions

The galvanic activity between austenite and ferrite has been investigated using samples prepared from wrought 2205 DSS base metal in the solution annealed condition and an HAZ, simulated in the same material using a Gleeble thermo-mechanical simulator. The simulated HAZ was designed to correspond to that of a single pass TIG weld. The following conclusions can be drawn:

•   The Gleeble-simulated microstructure shows a significant reduction in volta-potential difference between austenite and ferrite compared to similar measurements on the base metal;

•   Polarization measurements conducted in H2SO4/HCl electrolyte showed that the simulated weld HAZ thermal cycle affects the alloy passivation behaviour, reducing the difference in activation potentials between the two phases in the HAZ;

• The chemical partitioning, caused by the simulated welding thermal cycle, reduced the galvanic activity between the two phases in the HAZ with potential effects on the SCC resistance of the DSS.

4.3.5.1 Acknowledgments

4.3.6 References

[1]   R.N. Gunn, Developments, grades and specifications, Duplex Stainl. Steel. Microstruture, Prop. Appl. (1997) 1–13. doi:10.1533/9781845698775.1.

[2]   W.-T. Tsai, M.-S. Chen, Stress corrosion cracking behavior of 2205 duplex stainless steel in concentrated NaCl solution, Corros. Sci. 42 (2000) 545–559. doi:10.1016/S0010-938X(99)00105-5.

[3]   Z. Zhang, H. Jing, L. Xu, Y. Han, L. Zhao, J. Zhang, Influence of microstructure and elemental partitioning on pitting corrosion resistance of duplex stainless steel welding joints, Appl. Surf. Sci. 394 (2017) 297–314. doi:10.1016/j.apsusc.2016.10.047.

[4]   S. Atamert, J.E. King, Elemental partitioning and microstructural development in duplex stainless steel weld metal, Acta Metall. Mater. 39 (1991) 273–285. doi:10.1016/0956-7151(91)90306-L.

[5]   R.C. Newman, Stress corrosion cracking, Shreir's Corros. (2010) 864–901. doi:10.1016/B978-044452787-5.00035-4.

[6]   S. Edition, Metallurgy Second Edition Welding Metallurgy, Structure. 822 (2003) 466. doi:10.1016/j.theochem.2007.07.017.

[7]   R.N. Gunn, Welding metallurgy, in: Duplex Stainl. Steels, w, Abington, England, 1997: pp. 110–132. doi:10.1533/9781845698775.110.

[8]   W.-T. Tsai, S.-L. Chou, Environmentally assisted cracking behavior of duplex stainless steel in concentrated sodium chloride solution, Corros. Sci. 42 (2000) 1741–1762. doi:10.1016/S0010-938X(00)00029-9.

[9]   BS-EN-ISO, Specification and qualification of welding procedures for metallic materials — Welding procedure test —, (2012) 1–32.

[10]   H.Y. Liou, R.I. Hsieh, W.T. Tsai, Microstructure and pitting corrosion in simulated heat-affected zones of duplex stainless steels, Mater. Chem. Phys. 74 (2002) 33–42. doi:10.1016/S0254-0584(01)00409-6.

[11]   C. Örnek, D.L. Engelberg, Correlative EBSD and SKPFM characterisation of microstructure development to assist determination of corrosion propensity in grade 2205 duplex stainless steel, J. Mater. Sci. (2015). doi:10.1007/s10853-015-9501-3.

[12]   Y. Guo, T. Sun, J. Hu, Y. Jiang, L. Jiang, J. Li, Microstructure evolution and pitting corrosion resistance of the Gleeble-simulated heat-affected zone of a newly developed lean duplex stainless steel 2002, J. Alloys Compd. 658 (2016) 1031–1040. doi:10.1016/j.jallcom.2015.10.218.

[13]   I.H. Lo, Y. Fu, C.J. Lin, W.T. Tsai, Effect of electrolyte composition on the active-to-passive transition behavior of 2205 duplex stainless steel in H2SO4/HCl solutions, Corros. Sci. 48 (2006) 696–708. doi:10.1016/j.corsci.2005.02.004.

[14]   W.T. Tsai, J.R. Chen, Galvanic corrosion between the constituent phases in duplex stainless steel, Corros. Sci. 49 (2007) 3659–3668. doi:10.1016/j.corsci.2007.03.035.

[15]   R.-I. Hsieh, H.-Y. Liou, Y.-T. Pan, Effects of Cooling Time and Alloying Elements on the Microstructure of the Gleeble-Simulated Heat-Affected Zone of 22% Cr Duplex Stainless Steels, J. Mater. Eng. Perform. 10 (2001) 526–536. doi:10.1361/105994901770344665.

[16]   L. Guilherme, A. Benedetti, C. Fugivara, A portable electrochemical microcell for weld inspection of duplex stainless steel tanks, Corrosion. (2018) 3004. doi:10.5006/3004.

[17]   S. Aoki, H. Yakuwa, K. Mitsuhashi, J. Sakai, Dissolution Behaviour of Alpha and Gamma Phases of a Duplex Stainless Steel in a Simulated Crevice Solution, ECS Trans. 25 (2010) 17–22.

[18]   T.H. Chen, J.R. Yang, Microstructural characterization of simulated heat affected zone in a nitrogen-containing 2205 duplex stainless steel, Mater. Sci. Eng. A. 338 (2002) 166–181. doi:10.1016/S0921-5093(02)00065-5.

[19]   R.A. Cottis, R.C. Newman, Stress Corrosion Cracking Resistance of Duplex Stainless Steels, Health and Safety Executive - Offshore Technology Report, 1993.

[20]   A.J. Ramirez, S.D. Brandi, J.C. Lippold, Secondary austenite and chromium nitride precipitation in simulated heat affected zones of duplex stainless steels, Sci. Technol. Weld. Join. 9 (2004) 301–313. doi:10.1179/136217104225021715.

[21]   C.M. Garzón, C.A. Serna, S.D. Brandi, A.J. Ramirez, The relationship between atomic partitioning and corrosion resistance in the weld-heat affected zone microstructures of UNS S32304 duplex stainless steel, J. Mater. Sci. 42 (2007) 9021–9029. doi:10.1007/s10853-007-1881-6.

4.4 MANUSCRIPT 3 – "HYDROGEN ENHANCED CRACKING BEHAVIOUR OF DIFFERENT AUSTENITE MORPHOLOGIES IN THE HEAT AFFECTED ZONE OF A MULTI-PASS DSS2205 TIG WELD"

P. Reccagni[a], Q. Lu[b], M. Gittos[b], D.L. Engelberg[a]

[a] Corrosion and Protection Centre, University of Manchester, UK

[b] The Welding Institute TWI, Cambridge, UK

4.4.1 Abstract

Duplex stainless steels (DSSs) microstructure morphology shows significant variation in the heat affected (HAZ) zone of arc-welded components. Welding procedures are assessed upon the resulting austenite fraction and the avoidance of tertiary phases precipitation, while the austenite morphology in this region is not part of the evaluation. Even acceptable welds, however, show enhanced propensity to hydrogen-assisted failure mechanisms in the HAZ.

The effects of dissolved hydrogen on the cracking behaviour of different austenite morphologies have been studied in this work. Hydrogen pre-charged mini-tensile samples machined from a multi-pass 2205 TIG weld have been used for tensile strain to failure. The behaviour of the austenite in the hydrogen assisted cracking path has been investigated on the surface using quasi in-situ SEM straining and correlative post-mortem EBSD. Fractography has been used to gather in-depth information on the failure mode of austenite.

The results shows a lack of beneficial effects from grain boundary and intragranular austenite types in influencing the crack progression path, with phase boundary decohesion and brittle failure interesting this phase in addition to ductile tearing.

4.4.2 Introduction

Duplex stainless steels (DSSs) are an interesting choice for application in the petrochemical and energy industries [1-3] . The outstanding resistance to environment-assisted cracking (EAC) , combined with high strength and low nickel content, makes them an attractive choice for all those applications where stress corrosion cracking (SCC) [4-6] and hydrogen assisted cracking (HAC) [7,8] are a concern. Modern grades have also good weldability and multi-pass arc welding is often used to fabricate structures. Welding procedure specifications (WPS) are designed to avoid tertiary phases precipitation and excessive ferrite content in the heat affected zone (HAZ) [9-11]. Nonetheless, the HAZ always shows enhanced environment assisted cracking (EAC) susceptibility.

Hydrogen sources, such as the cathodic reactions at the surface of cathodically protected components, can pose a threat to DSSs integrity when significant hydrogen uptake in the material occurs [12,13]. Relatively small amounts of hydrogen are sufficient to cause embrittlement of the ferritic matrix, which is characterised by low hydrogen solubility [14]. Austenite conversely is less easily embrittled and its ability to stop crack progression – until stress level causing ductile tearing are reached– explains the superior behaviour of duplex over purely ferritic steels.

Welding affects the microstructure in the HAZ by producing larger ferritic grains [15,16] and increased ferrite content [17], partially explaining why this region is the more susceptible to HAC [15]. Welding also affects austenite morphology and a combination of intragranular austenite, Widmanstatten plates and grain boundary austenite characterise this region [18]. The role of austenite morphology, rather than austenite fraction, in the context of HAC in the HAZ has received less attention.

The purpose of this work is to directly observe the ability of different types of austenite to block or deviate cracks in the hydrogen embrittled HAZ. To do so, mini-tensile samples have been extracted from a multi-pass TIG weld and their microstructure characterized. Cathodic polarization in acidic environment has been used to introduce hydrogen in the microstructure, with the charging routine validated initially on the base metal where the surface defects caused by hydrogen charging have been characterized. The pre-charged specimens containing all regions of the weld have been used for quasi in-situ SEM straining and the images of the crack initiation correlated with post-mortem EBSD and fractography. Before and after cracking EBSD maps have also been used, on a larger scale, to describe the relation between cracking path and austenite morphology.

4.4.3 Methodology

4.4.3.1 Materials Characterization

The material used was a 2205 duplex grade in the form of a seamed pipe with 406 mm internal diameter and 9.2 mm wall thickness. Two sections of the pipe were joined with a TIG girth weld performed in 7 passes. Different heat inputs were selected for the root weld and the subsequent passes, while pure Argon was used as shielding/backing gas in order to avoid contamination from the environment. Mini-tensile samples exposing both the weld and the parent material were machined along the transversal direction using EDM (Electric Discharge Machining) – a sketch of the geometry is shown in Figure 51.
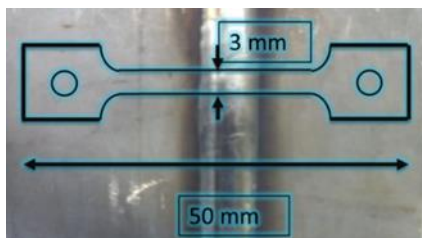
Figure 51 - Mini-tensile samples geometry.

Samples were wet ground with SiC paper (up to 4000 grit) and then polished with diamond paste (2, 1 and 0.25 micron) followed by finer polishing in colloidal silica suspension for 30 minutes. The microstructure was investigated by means of Electron Back-Scatter Diffraction (EBSD), using a FEI Sirion FEG-SEM equipped with a Nordlys EBSD detector from Oxford Instruments.

4.4.3.2 Hydrogen Charging

For all experiments, hydrogen was introduced in the microstructure by means of cathodic polarization in aqueous solution on the polished samples. The electrolyte used was 0.1M sulphuric acid with 250 mg/L addition of $NaAsO_2$ for hydrogen recombination poisoning [19,20] . Samples were polarized with a galvanostat (ACM Instruments) imposing a cathodic current of 20 mA/cm^2 for 48 hours. The solution was kept at 80 °C (±2 °C) with a heating plate and agitation of the solution was assured by nitrogen bubbling. Hydrogen ingress was limited to one face of the sample by masking the rest with lacquer.

In order to assess whether the parameters used were suitable to cause embrittlement of the alloy also in reference conditions, a tensile sample of the parent material has been charged in the same way. All the sides of the gauge however where exposed, in order to observe the effects of diffusion in different directions on the fracture behaviour. The depth of embrittlement measured on this sample was used to introduce the concept of a "damage effective" diffusion coefficient. The sample has been used also to show, for reference, the typical cracking behaviour of hydrogen embrittlement of annealed duplex stainless steel.

Noticeable microstructural changes induced on the surface by the hydrogen charging process were observed. Therefore, a dedicated sample from the parent material was charged in these condition and investigated by means of SEM imaging of the surface combined with EBSD characterization of the defects in cross-section.

4.4.3.3 Hydrogen-Enhanced Cracking in the Heat Affected Zone

The preferred cracking path in the HAZ microstructure has been investigated in two different ways.

- In one sample, the HAZ has been EBSD mapped before hydrogen charging; after the cathodic polarization, the sample has been ex-situ strained to failure and EBSD maps of the crack profile were acquired on one of the two parts. In both cases, the step-size used was 1μm. By comparison of the two sets of EBSD maps, the location of the crack path has been reconstructed;

- Another sample has been investigated by means of SEM in-situ straining; in this case, after hydrogen charging the sample has been quickly re-polished to remove the hydrogen-induced surface defects - removing ca. 100 um of material - and then immediately strained in the SEM. Straining has been applied at 1% strain increments. Images of the crack initiation were produced and the sample was later strained to failure allowing for fractographic inspection. EBSD maps across the crack in the initiation location have been also acquired.

In both experiments, the strain was applied using a 5 kN mini-tensile rig from Deben. The strain rate used was 1.9×10^{-4} s^{-1}. The SEM in-situ straining was performed in a FEI Quanta 650 FEG-SEM.

4.4.4   Results

4.4.4.1 Characterization

The weld microstructure shows features typical of DSS welds. Of particular interest in this work are the austenite fraction and morphology in the surrounding of the fusion line, where the melted filler material in the weld pool blends with the welding piece. The first

noticeable microstructural change is the variation in austenite content. In particular, while the weld and the low temperature HAZ show acceptable phase balance, the region surrounding the fusion line shows austenite content close or below 30% - threshold value for the duplex microstructure to show any beneficial effect on EAC resistance [67]. While the width of this region was relatively small (approximately 100um), this location offers an almost continuous path of ferrite surrounding the weld. A profile of the austenite content across the weld is shown in Figure 52.
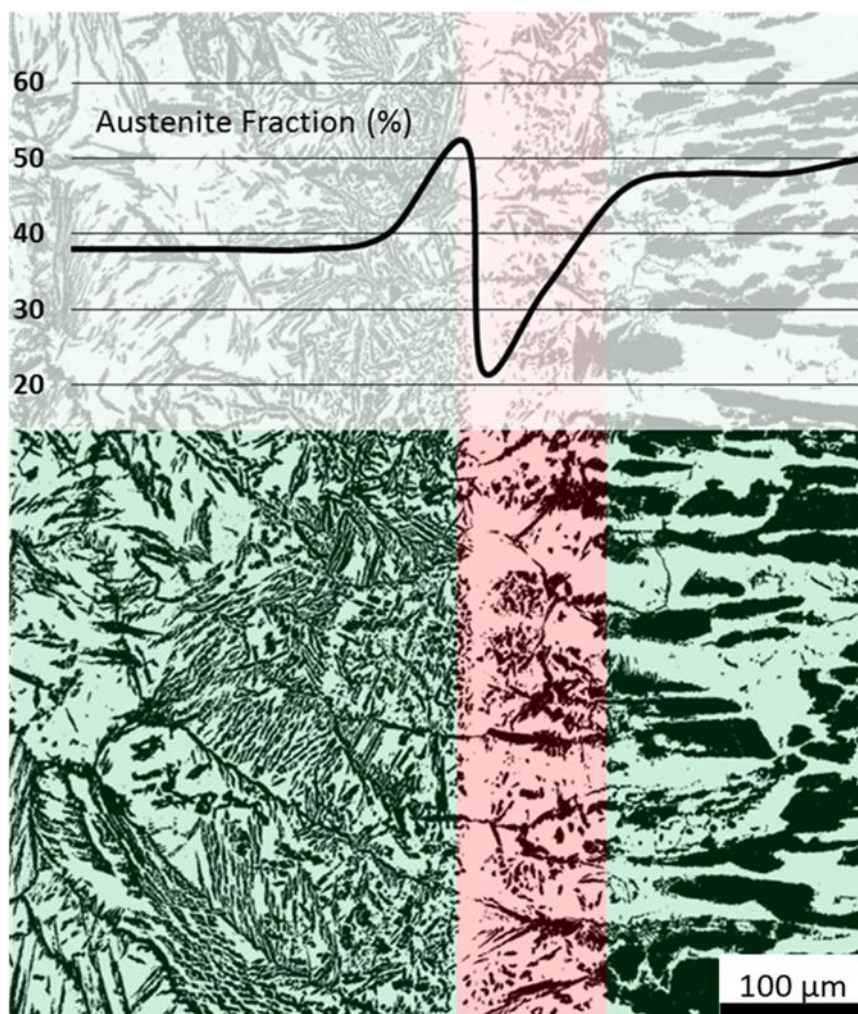
Figure 52 - Austenite fraction distribution in the high temperature HAZ. Austenite in black, ferrite in white.The austenite fraction is estimated with image analysis (method described in 4.1.1.2).

Austenite in the ferrite rich region showed different morphologies. In particular, the reformed austenite can nucleate either at the grain boundaries between ferritic grains

133

(grain boundary austenite, GBA) or within a ferrite grain (intragranular austenite, IGA). Due to the location where it forms, GBA has the characteristic of breaking the continuity of adjacent ferrite grains while IGA, in the form of small isolated plates within a single ferritic grain, does not form a continuous structure. Examples of these morphologies are shown in figure Figure 53.
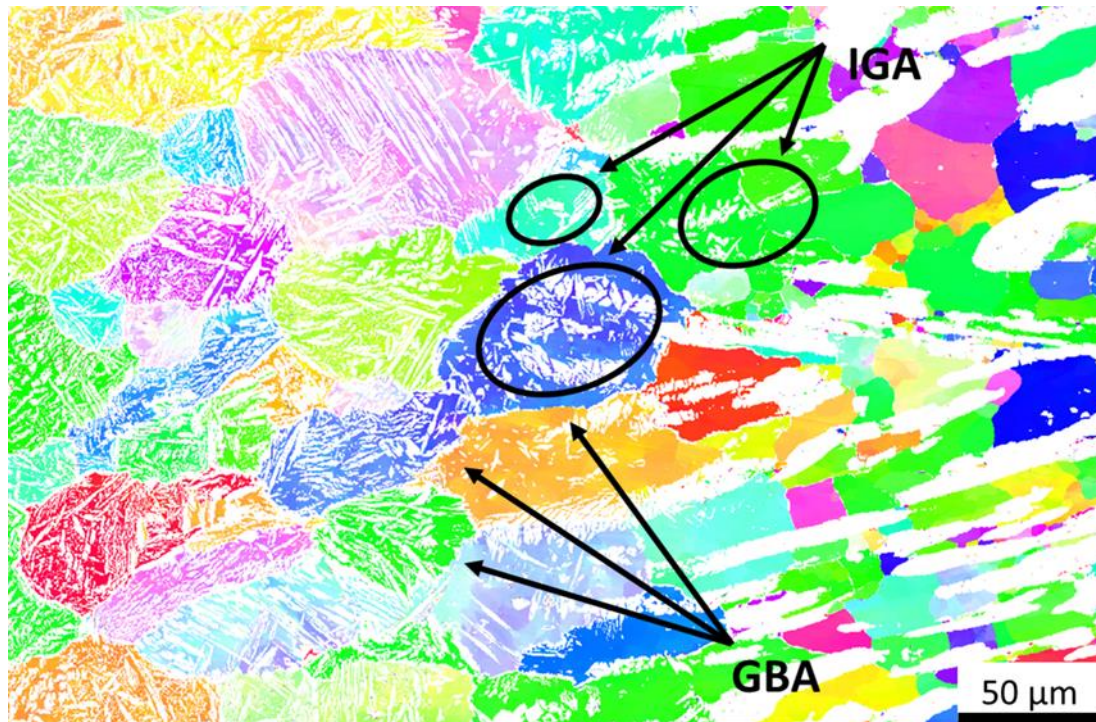
Figure 53 - Austenite morphologies in the HAZ. Austenite in white, Ferrite in IPF colours.

4.4.4.2 Hydrogen-Induced Surface Defects

After charging in these conditions, the surface of the material presented with several new features. In particular two types of damage were found. In the austenite, surface cracks were found. Relieved protrusions, sometimes associated with minor cracks, were found in the ferrite. An example of surface after charging is shown in Figure 54. Phases were identified by means of EDX-S spectroscopy, relying on the chromium and molybdenum enrichment in the ferrite.
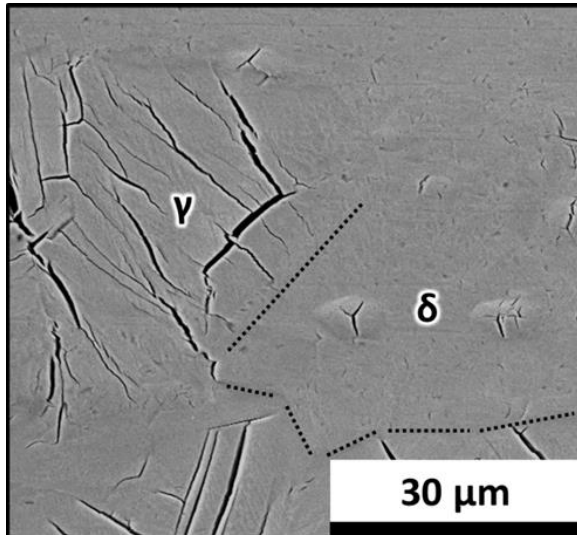
Figure 54 - DSS surface after hydrogen charging (20mA cm^{-2}, 80°C, 01.M H_2SO_4 + 250 mgl^{-1} $NaAsO_2$, 48hrs).

A cross section of the parent material was used to explore the depth of the defects. These were found only in the initial 20-30 um below the surface. EBSD maps of the cross section showed that the defects are confined to the surface grains, which are directly exposed to the hydrogen ingress/desorption, and to the interphases underneath.

Cross-section observation revealed that the austenite after charging developed several cracks in the grains exposed to the surface – see Figure 55
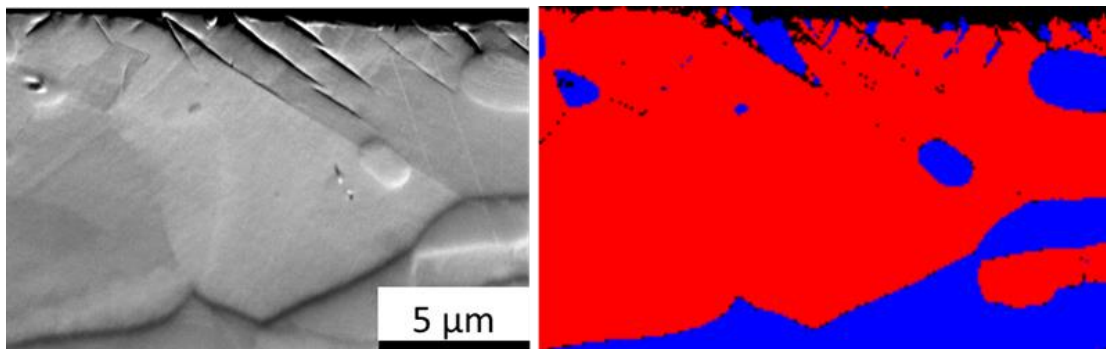
Figure 55 - Cross section of damage in hydrogen charged DSS surface (left) and EBSD phase map of the same location (right).Austenite in red, ferrite in blu.

The EBSD maps in the surrounding of the cracks showed the formation within the austenite of small lathes of a tertiary BCC phase. The two phases show a Kurdjumov-Sachs type

lattice relation "within" 10 degrees of error from the theoretical orientation, compatible with the formation of BCC martensite, as shown in Figure 56.
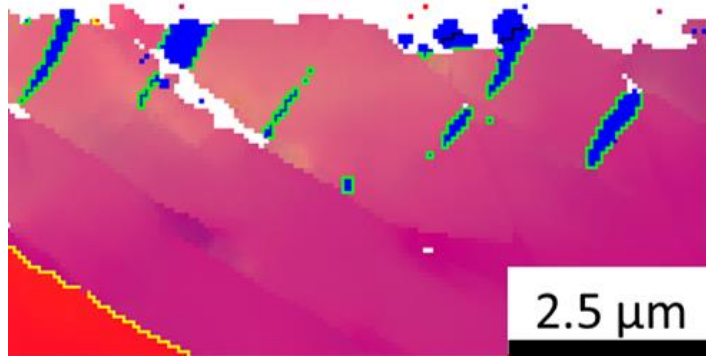
Figure 56 - Detail of the cross section EBSD map. In blu, the BCC martensite lathes. K-S phase boundaries in green.

The nature of the defects in ferrite was different. In particular, the main characteristic was the formation of blisters at the interphase between the ferrite exposed to the environment and the underlying austenite – see Figure 57. The volume expansion at the interphase was compensated by deformation of the ferrite.
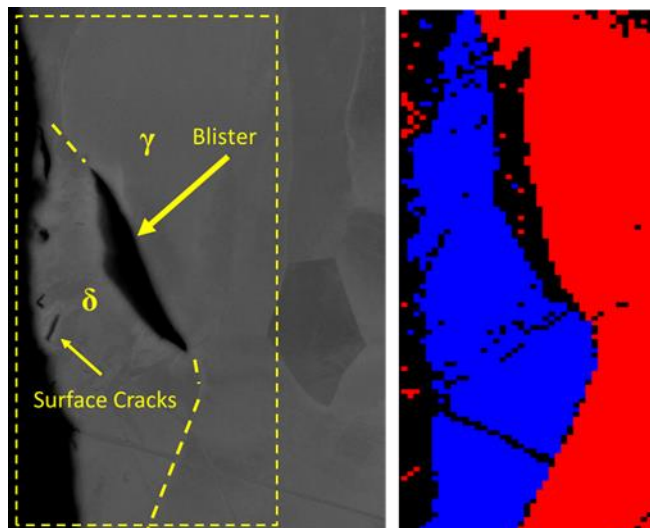
Figure 57 - Cross section micrograph showing one blister at the ferrite:austenite interphase (left) with EBSD phase map (right).

The deformation was accompanied with the formation of sub-grains in the ferrite, showing a 60deg misorientation with the original grain, suggesting deformation twinning occurred [21] – as shown in Figure 58.
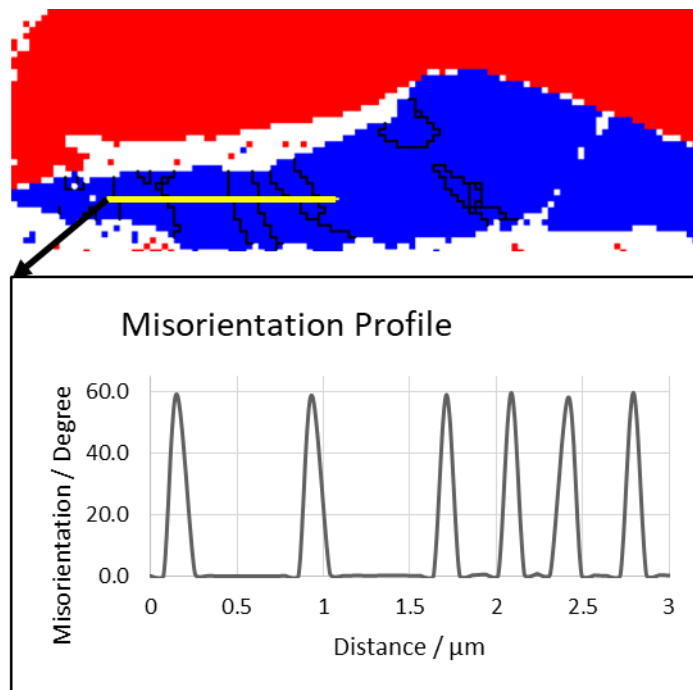
Figure 58 - Misorientation line-scan across the subgrains in the deformed ferrite, showing the twin boundaries at 60deg misorientation

4.4.4.3 Hydrogen embrittlement in the parent material

The hydrogen charging conditions used promoted significant embrittlement of the microstructure in the tensile sample of the base metal. This can be observed in the fracture surface after strain-to-failure, where the ductile failure at the core of the sample is surrounded by a rim of material failed in a brittle fashion, as shown in Figure 59,where the average depth of embrittlement is alsoshown. The diffusion pathway oriented as the rolling direction (i.e. horizontal in the image) shows the deepest damage, consistent with the less tortuous hydrogen diffusion path - and therefore, higher hydrogen diffusion rate in this direction.
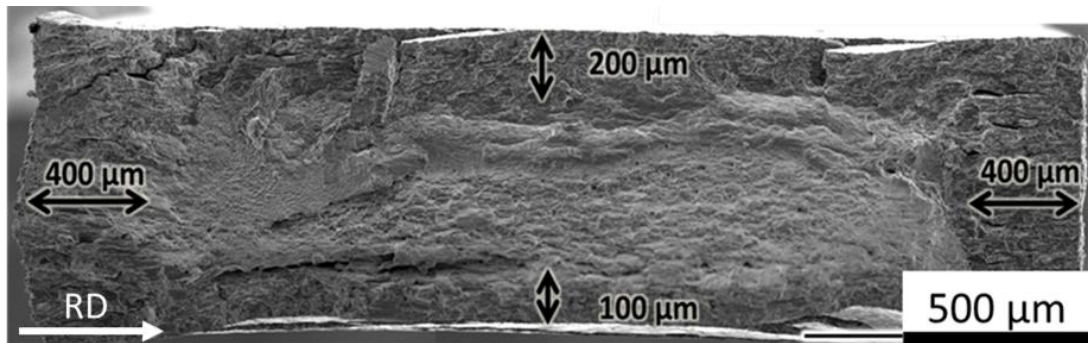
Figure 59 - Fracture surface of an hydrogen charged mini-tensile sample of the parent material. Average depth of the brittle failure shown in the picture.

Figure 60 shows an EBSD phase map for a region of the longitudinal cross section containing a secondary crack. This shows the typical behaviour of duplex stainless steels exposed to hydrogen, with the crack progressing through the embrittled ferrite and the elongated austenite showing the ability to deviate the crack progression until ductile tearing eventually occurs.
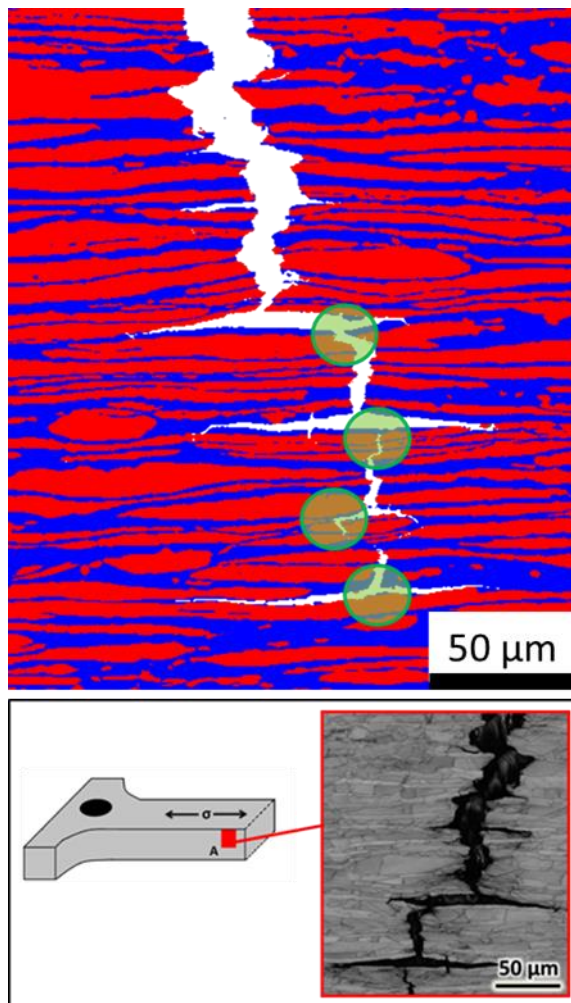
Figure 60 - - EBSD phase map of a secondary crack cross section (top). Position of the crack with respect to the tensile sample and strain direction (bottom).

4.4.4.4 Hydrogen embrittlement in the HAZ - Crack path

As expected, the crack developed in the HAZ of the hydrogen-charged mini-tensile sample. Despite the surface defects and the strain applied, sufficient indexing was achieved in the post-mortem EBSD scans, allowing reconstruction of the crack path with respect to the microstructure. The failure mode of the embrittled microstructure was clearly transgranular through the enlarged HAZ ferritic grains, while the position of the crack with respect to the austenite was not consistent. However, it was noticeable that the grain boundary austenite and the small intragranular austenite plates in the HAZ offered little or no opposition to the crack progression. Crack path is visible in Figure 61. Only in two points

austenite showed the ability to deviate the crack path. In both cases, austenite was coarser, with dimensions between 100 and 150 μm.
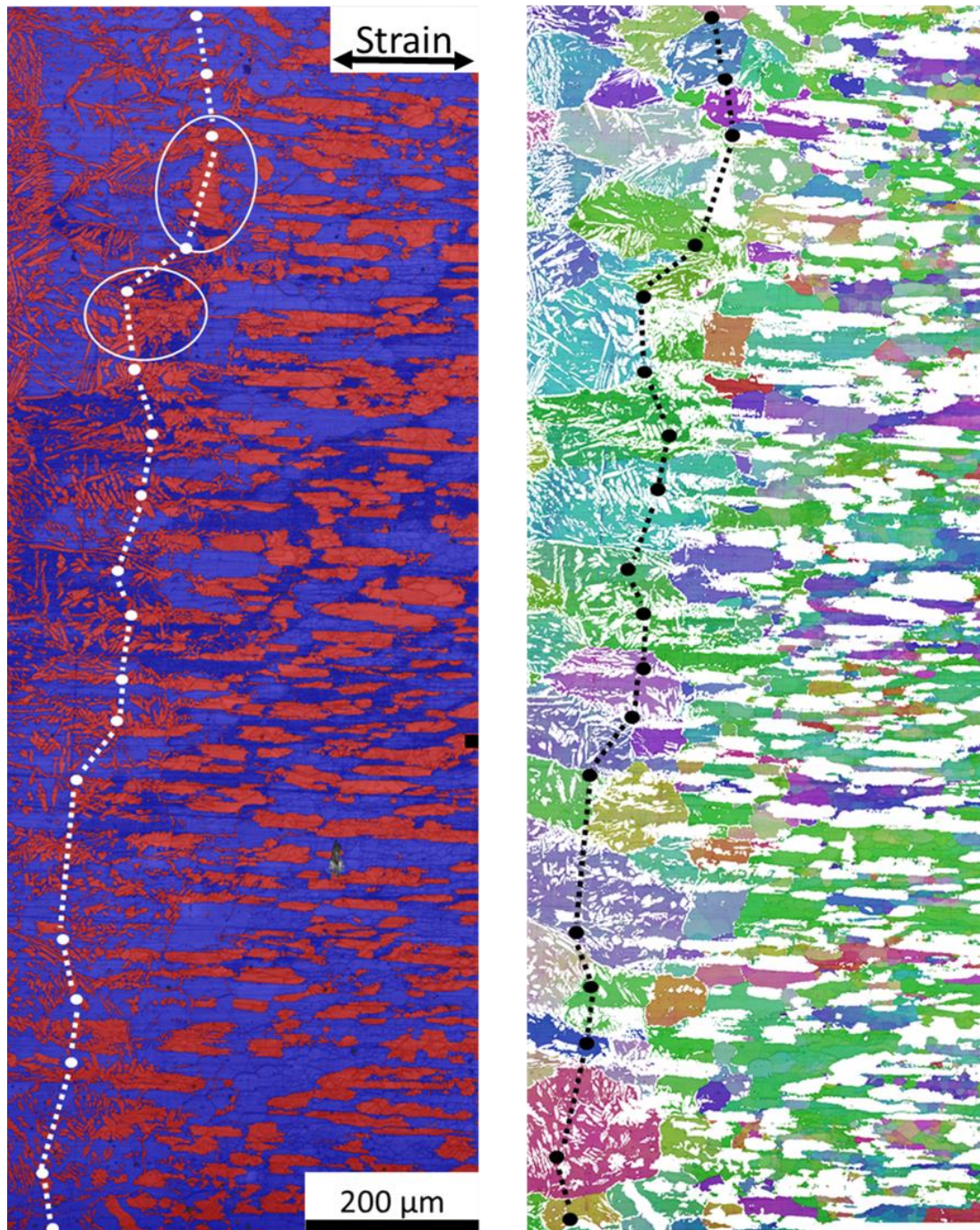
Figure 61 - Crack path reconstruction in the HAZ. Left: EBSD phase map, austenite in red and ferrite in blue. Locations where austenite deviated the crack path are circle in white. Right: austenite in white and ferrite in IPF colours.

4.4.4.5 Hydrogen embrittlement in the HAZ - Crack-initiation

In depth analysis of the crack initiation was used to describe the early stages of cracking. During the quasi in-situ test, the first crack was found to open at as little as 6% strain – see Figure 62.
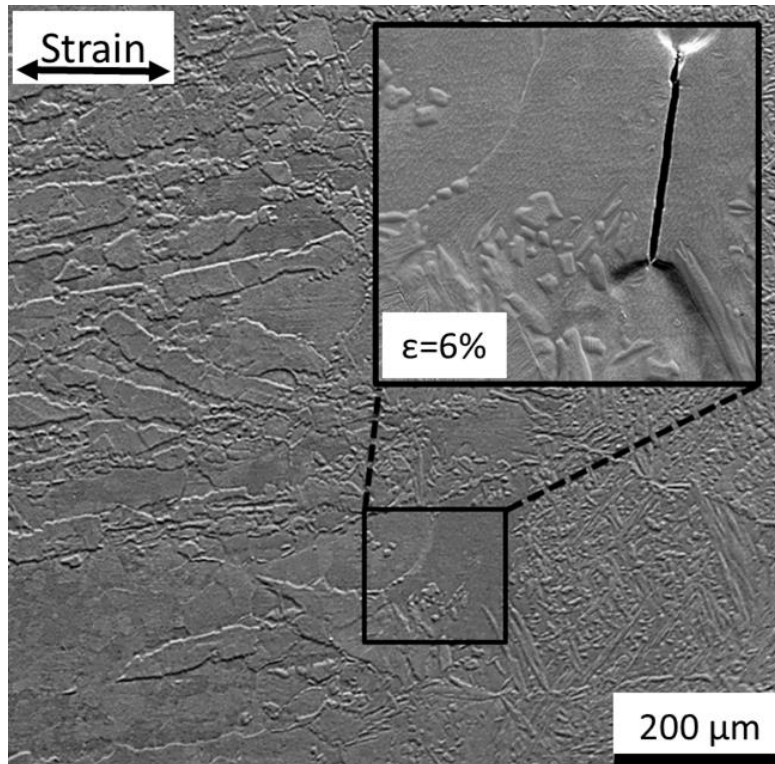
Figure 62 -Crack initiation in the quasi in-situ straining.

Also in this case, the crack showed a neat progression along the fusion line of the HAZ. From the micrographs, the crack seemed to initiate trans-granularly in the ferrite and did not show correspondence with the austenite:ferrite boundaries. More complete information was obtained by observing the EBSD map of the region (shown in Figure 63) and the fracture surface.
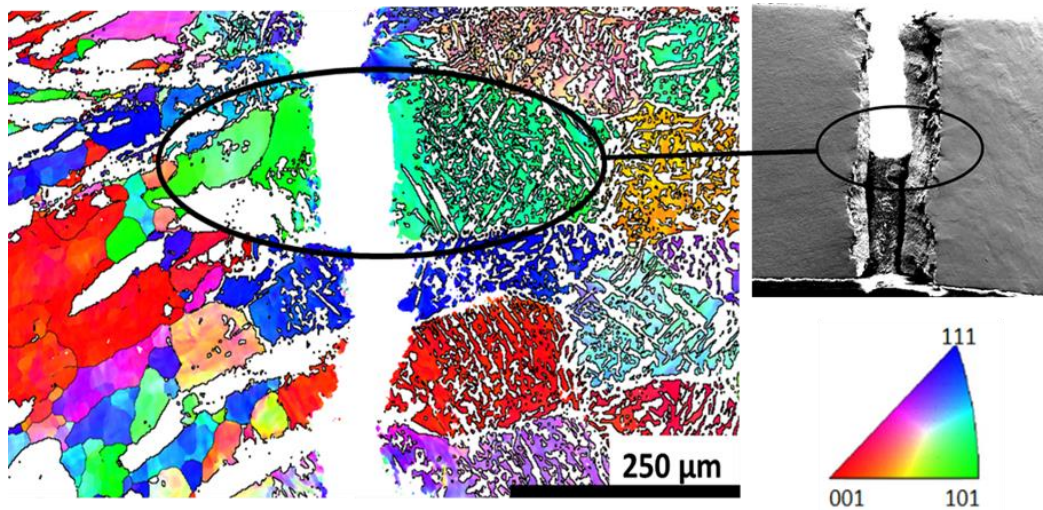
Figure 63 - Post-mortem EBSD on the quasi in-situ strained sample showing the ferite distribution (IPF colours).

In particular, the two faces of the fractured surface have been matched – as well as possible - and an EBSD map of the crack initiation location has been acquired across the crack. The two sides of the crack initiation region were ferritic on both sides; further, the misorientation across was approx. 5deg, suggesting that the crack initiated within the same ferritic grain. In fact, the small misorientation, could identify a low-angle grain boundary (LAGB) but can also be an artefact attributable to the difficulty of manually re-aligning the two parts of the sample on the aluminium stub. Nonetheless, observing the morphology of similar grains in the HAZ region, the occurrence of LAGBs was not noticeable anywhere else, suggesting that the second explanation is the most likely and that the crack initiation was indeed intragranular.

4.4.4.6 Hydrogen embrittlement in the HAZ - Fractography

In the fractography, it was possible to see a clear difference in failure mode between the side of the sample exposed to hydrogen, which clearly underwent brittle failure, and the opposite side showing features typical of ductile failure, consistent with the longer diffusion path for the hydrogen to reach the opposite side of the section – Figure 64.
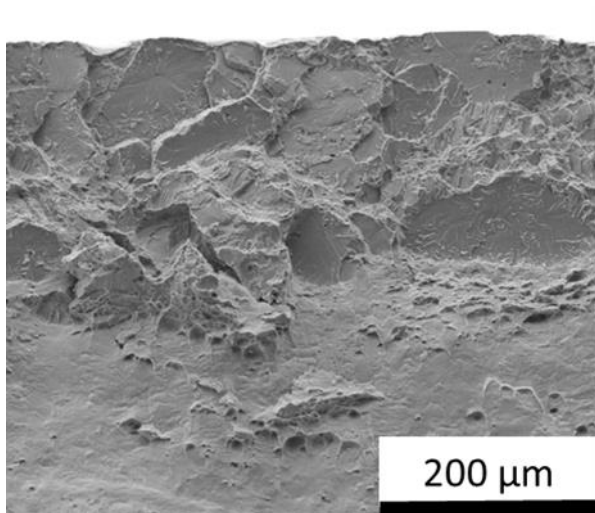
Figure 64- Details of the fracture surface, showing the embrittled region and the brittle to ductile transition

The surface of the grain where the crack initiated – shown in Figure 65- showed an almost completely ferritic region, confirming what observed with micrographs and EBSD. The fracture surface presented with river-like marks typical of quasi-cleavage, failure mode characteristic of embrittled BCC steel.
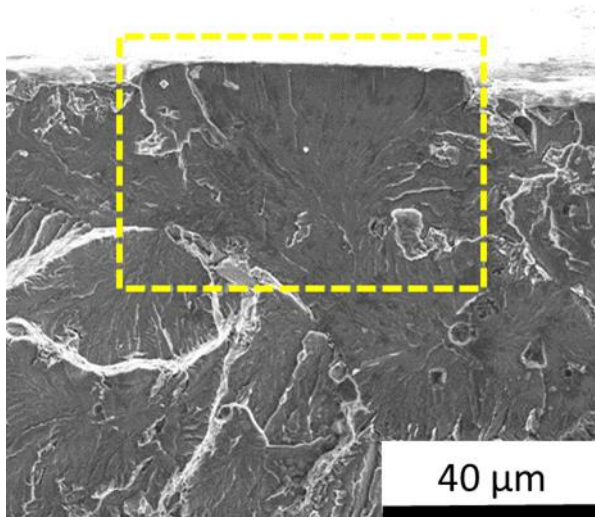
Figure 65 - Fractography of the crack initiation ferrite grain with the position of the first crack opening marked.

The failure mechanism of the austenite grains in the surrounding of the region was less clear. Some grains in the embrittled region showed a faceted surface, suggesting the failure mechanism was not purely ductile, as shown in Figure 66 (left). The effect of the diffused

hydrogen on this phase was also noticed at the austenite: ferrite phase boundaries, where signs of fcc:bcc decohesion were found. Phase boundary decohesion was found in the surrounding of austenite grains that looked almost intact, potentially indicating that complete detachment from the ferrite occurred, as shown in Figure 66 (right).
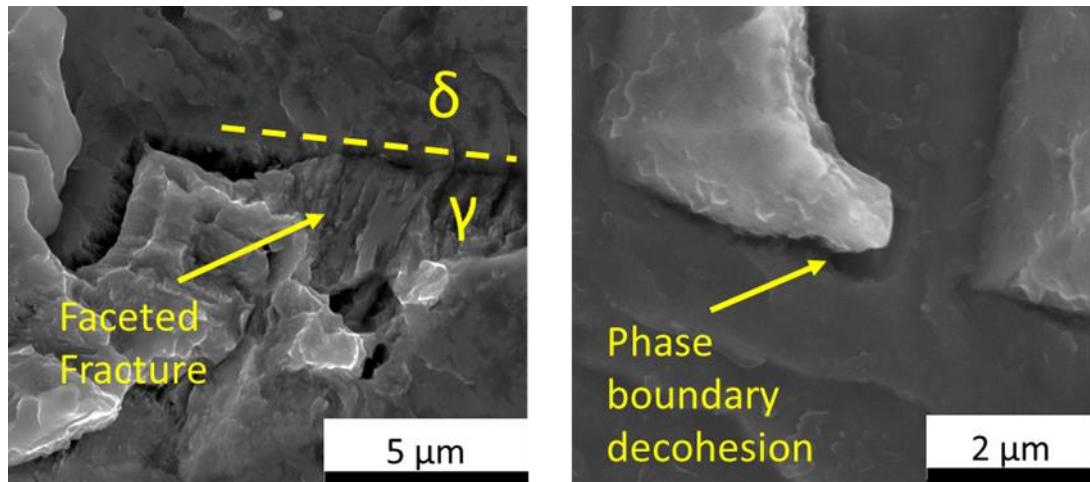
Figure 66 - Details of the austenite fracture behaviour. Faceted brittle-like failure of austenite (left) and austenite:ferrite phase boundaries decohesion (right).

4.4.5 Discussion

The fundamental mechanism of hydrogen embrittlement have been studied by several authors and are nonetheless still matter of debate [22]. While a mechanistic understanding of hydrogen damage in duplex stainless steel has still to be achieved, several factors affecting their macroscopic cracking resistance have been identified. With respect to the microstructure, higher ferrite fractions and larger ferrite grains are recognised as detrimental to DSSs hydrogen embrittlement resistance. These two conditions are often found in the HAZ of welded microstructure, where the alloy is heated above the solvus temperature and then quickly cooled. While modifications in the ferrite microstructure are largely responsible of the higher susceptibility of the HAZ, the role of the austenite morphology was the main focus of this work. The elongated plates typical of the annealed microstructure are replaced by a combination of intragranular austenite and grain

boundary austenite in the surrounding of the fusion line, with the local austenite fraction significantly lower than the ideal 50%.

This work's aim was to investigate the ability of the types of austenite found in the HAZ to deviate or stop the crack progression in hydrogen charged microstructures subjected to tensile straining. Three stages of hydrogen induced damage have been investigated, covering the effects of hydrogen diffusion on the microstructure, the role of austenite in crack initiation and austenite ability to influence the crack progression path.

(i) Hydrogen charging and Surface Damage

Hydrogen ingress affects both phases in a very different way. Austenite fcc microstructure has higher hydrogen solubility and can therefore accommodate more hydrogen in the lattice. However, once the solubility limit is reached, hydrogen cause strain in the microstructure and this is accommodated by following a sequence of phase transformations. In first place, an instable hydrides phase forms, acting as an intermediate step toward formation of HCP (ε) martensite within the austenite grain [22-24]. HCP martensite, however is a metastable phase and is replaced by BCC martensite allowed sufficient time. The higher diffusion rate in ferrite, causes different type of damage in this phase. Ferrite is not directly affected by the hydrogen ingress until hydrogen reaches an underlying austenite phase boundary. Here the fast diffusion reaches a sudden stop, due to the high binding energy of the phase boundary and to the slow diffusion through austenite [19,25]. As a result of the atomic hydrogen build up in this location, hydrogen recombination occurs and the pressure build-up due to the larger volume of molecular hydrogen causes plastic deformation in the ferrite, with deformation twins formed during the process.

While significant, these defects interest only the surface of the duplex steel and they are not found in the deeper layers of the alloy. This can be explained considering both

hydrogen concentration and physical properties of the surface. The concentration of the diffusing specie in a solid where diffusion is occurring reaches its maximum at the entry surface, where the saturation concentration is maintained by the continuous provision of the diffusing element from the environment. In the case of hydrogen electrolytic charging, the applied cathodic current provides atomic hydrogen adsorbed on the surface through water electrolysis and acidity reduction reactions. As a result, the concentration of hydrogen is maximum in this location and decreases exponentially deeper in the alloy. Further, the phase transformations induced by hydrogen during ingress/outgas in austenite and the blistering in ferrite involve significant volume changes. The lower mechanical constraint of the grains at the surface contributes to explain why these transformations are observed only here.

 (ii) Crack initiation and progression

Ferrite is the hydrogen embrittlement susceptible phase in duplex steels, with transgranular quasi-cleavage being the typical failure mode of this phase [8,22]. In annealed duplex grade, where the austenite is distributed in elongated plates, macroscopic crack progression occurs through ductile tearing of this phase, while embrittlement of the austenite is not generally observed. The higher solubility of hydrogen in austenite, in fact, allows this phase to accommodate higher amount of interstitial hydrogen with respect to a bcc microstructure.

Observation of the crack initiation on the surface and from the suggested that cracking initiated within an individual ferritic grain. The fracture surface of the severed grain, showed almost no austenite in the crack opening location. Upon further straining, the austenite found in the HAZ did not show the same ability to block crack progression as in the annealed state, with the crack following the fusion line almost unaffected by the austenite found on its path.

Looking at the fracture surface, it was noticed that some of the austenite grains in the embrittled region showed signs of brittle failure. Austenite is not per se immune to embrittlement, given sufficient concentration of hydrogen in this phase is reached. Austenite embrittlement in duplex is not normally observed due to the higher susceptibility of ferrite, causing hydrogen induced failure to originate in the latter before a sufficient concentration of hydrogen can be reached in the austenite. The austenite fraction in the HAZ is locally lower than the ideal 50%, whit the larger fraction of ferrite allowing for a larger hydrogen diffusion front to cross this region. At the same time, most of the austenite grains in the HAZ are smaller and isolated (IGA), suggesting that the local concentration of hydrogen in these grains, due to their smaller volume, could raise to levels that would not be observed in the normal duplex. Some austenite grains also showed signs of phase boundary decohesion, suggesting that the accumulation of hydrogen at the phase boundaries could weaken the bond between austenite and ferrite. This observation is confirmed by the presence on the fracture surface of grains that seemed completely detached from the ferrite on the fracture plane rather than crossed by the crack. It is worth to mention also the importance of the hydrogen charging conditions used for these experiments. The cathodic current applied to the sample was chosen to accelerate the effects of a severe cathodic overprotection. At the same time, the temperature used and the addition of hydrogen recombination poison also contributed to faster hydrogen diffusion kinetics. While this situation is particularly harsh for the alloy, the natural occurrence of hydrogen recombination poisonous elements - a notable example is sulphur in H_2S environment – justifies the study of hydrogen embrittlement in extremely detrimental conditions.

Austenite did not show univocal behaviour, but some correlation between cracking behaviour and austenite morphology can be drawn considering the crack path over a wider area. The crack path over the entire HAZ of the minitensile sample showed quite clearly

that the least resistant path for cracking is represented by the enlarged ferrite grains along the fusion line, which are crossed in a trans-granular mode. This is also the region characterized by a prevalence of intragranular and grain boundary austenite. The crack progression in the HAZ was almost unaffected by the presence of GBA and IGA, with the path clearly driven by the ferrite morphology. On the other end, coarser austenite grains (or clusters of grains) on the crack path showed the ability to influence the crack path. In other words, this type of austenite seemed to retain some of the properties of austenite in annealed conditions.

It is difficult to separate the contribution of the two phases in promoting cracking susceptibility in the HAZ, given that the ferrite and austenite morphological changes happen simultaneously in the welding process. What can be gathered is that IGA and GBA do not show any significant effect in opposing hydrogen enhanced cracking, despite being assimilated to the other forms of austenite in the qualification of a welding procedure. The outcomes of this work suggest that excluding GBA and IGA from the austenite count during the welding procedure qualification could offer a more realistic prediction of the weld resistance to HAC.

4.4.6   Conclusions

(1)   Increased ferrite content, larger ferritic grain and a mix of intragranular and grain boundary austenite types characterize the fusion line of the HAZ, which is the region with the highest susceptibility to hydrogen-assisted failure;

(2)   Hydrogen electrolytic charging in poisoned acidic environment caused different damage at the surface in both phases; despite significant, these were found only in the first layers of the material and the phase transformation involved were not noticed deeper in the microstructure;

(3)   Surface cracks in the austenite where noticed after hydrogen charging in these conditions. These cracks were affecting only the surface austenite grains, with no progression through the depth of the microstructure noticed;

(4)   The cracking path of hydrogen charged welds during strain-to-failure was mainly driven by the ferrite distribution in the region, with the IGA and GBA showing little or no influence on the crack propagation;

(5)   Austenite in this region showed multiple failure modes, with signs of embrittlement noticed also in this phase. Austenite:ferrite decohesion at the phase boundaries also contributed to the HAZ cracking;

(6)   Only in two points the crack path was affected by austenite. In these location, coarser austenite plates seemed to have an effect on deviating the crack path, similar to what happens in annealed microstructures.

4.4.7   References

[1]   R.N. Gunn, Developments, grades and specifications, Duplex Stainl. Steel. Microstruture, Prop. Appl. (1997) 1–13. doi:10.1533/9781845698775.1.

[2]   J.O. Nilsson, Overview Super duplex stainless steels, Mater. Sci. Technol. 8 (1992) 685–700.

[3]   N.R. Baddoo, Stainless steel in construction: A review of research, applications, challenges and opportunities, J. Constr. Steel Res. 64 (2008) 1199–1206. doi:10.1016/j.jcsr.2008.07.011.

[4]   R.A. Cottis, R.C. Newman, Stress Corrosion Cracking Resistance of Duplex Stainless Steels, Health and Safety Executive - Offshore Technology Report, 1993.

[5]   W.-T. Tsai, S.-L. Chou, Environmentally assisted cracking behavior of duplex stainless steel in concentrated sodium chloride solution, Corros. Sci. 42 (2000) 1741–1762. doi:10.1016/S0010-938X(00)00029-9.

[6]   D.L. Engelberg, C. Örnek, Probing propensity of grade 2205 duplex stainless steel towards atmospheric chloride-induced stress corrosion cracking, Corros. Eng. Sci. Technol. 49 (2014) 535–539. doi:10.1179/1743278214Y.0000000205.

[7]   S.-L. Chou, W.-T. Tsai, Hydrogen embrittlement of duplex stainless steel in concentrated sodium chloride solution, Mater. Chem. Phys. 60 (1999) 137–142. doi:10.1016/S0254-0584(99)00077-2.

[8]   L.W. Tsay, M.C. Young, C.-S. Shin, S.L.I. Chan, Hydrogen-enhanced cracking of 2205 duplex stainless steel, Fatigue Fract. Eng. Mater. Struct. 30 (2007) 1228–1236. doi:10.1111/j.1460-2695.2007.01191.x.

[9]   BS-EN-ISO, Specification and qualification of welding procedures for metallic materials — Welding procedure test —, (2012) 1–32.

[10]   H. Sieurin, R. Sandström, Sigma phase precipitation in duplex stainless steel 2205, Mater. Sci. Eng. A. 444 (2007) 271–276. doi:10.1016/j.msea.2006.08.107.

[11]   S. Edition, Metallurgy Second Edition Welding Metallurgy, Structure. 822 (2003) 466. doi:10.1016/j.theochem.2007.07.017.

[12]   A. Bahrami, P. Woollin, Hydrogen Induced Stress Cracking of Duplex Stainless Steel Subsea Components, 112 (2010) 1–10.

[13]   D.N. Veritas, Design of Duplex Stainless Steel Subsea Equipment Exposed To Cathodic Protection October 2008, Computer (Long. Beach. Calif). (2008).

[14]   A. Turnbull, R.B. Hutchings, Analysis of hydrogen atom transport in a two-phase alloy, Mater. Sci. Eng. A. 177 (1994) 161–171. doi:10.1016/0921-5093(94)90488-X.

[15]   S.-L. Chou, W.-T. Tsai, Effect of grain size on the hydrogen-assisted cracking in duplex stainless steels, Mater. Sci. Eng. A. 270 (1999) 219–224. doi:10.1016/S0921-5093(99)00174-4.

[16]   C. Örnek, P. Reccagni, U. Kivisäkk, E. Bettini, D.L. Engelberg, J. Pan, Hydrogen embrittlement of super duplex stainless steel – Towards understanding the effects of microstructure and strain, Int. J. Hydrogen Energy. 43 (2018) 12543–12555. doi:10.1016/j.ijhydene.2018.05.028.

[17]   R.N. Gunn, Welding metallurgy, in: Duplex Stainl. Steels, w, Abington, England, 1997: pp. 110–132. doi:10.1533/9781845698775.110.

[18]   H.Y. Liou, R.I. Hsieh, W.T. Tsai, Microstructure and pitting corrosion in simulated heat-affected zones of duplex stainless steels, Mater. Chem. Phys. 74 (2002) 33–42. doi:10.1016/S0254-0584(01)00409-6.

[19]   O. Sobol, G. Holzlechner, G. Nolze, T. Wirth, D. Eliezer, T. Boellinghaus, W.E.S. Unger, Time-of-Flight Secondary Ion Mass Spectrometry (ToF-SIMS) imaging of deuterium assisted cracking in a 2205 duplex stainless steel micro-structure, Mater. Sci. Eng. A. 676 (2016) 271–277. doi:10.1016/j.msea.2016.08.107.

[20]   T. Zakroczymski, Z. Szklarska-Śmiałowska, M. Smialowski, Effect of Arsenic on Permeation of Hydrogen Through Steel Membranes polarized cathodically in aqueous solution, Mater. Corros. 26 (1975) 617–624. doi:10.1002/maco.19750260804.

[21]   T. Šmida, J. Bošanský, Deformation twinning and its possible influence on the ductile brittle transition temperature of ferritic steels, Mater. Sci. Eng. A. 287 (2000) 107–115. doi:10.1016/S0921-5093(00)00828-5.

[22]   T. Zakroczymski, a. Glowacka, W. Swiatnicki, Effect of hydrogen concentration on the embrittlement of a duplex stainless steel, Corros. Sci. 47 (2005) 1403–1414. doi:10.1016/j.corsci.2004.07.036.

[23]   M.J. Wozniak, a. Glowacka, J. a. Kozubowski, Magnetic properties of austeno-ferritic stainless steel after cathodic hydrogen charging, J. Alloys Compd. 404–406 (2005) 626–629. doi:10.1016/j.jallcom.2005.01.123.

[24]   A. Barnoush, M. Zamanzade, H. Vehoff, Direct observation of hydrogen-enhanced plasticity in super duplex stainless steel by means of in situ electrochemical methods, Scr. Mater. 62 (2010) 242–245. doi:10.1016/j.scriptamat.2009.11.007.

[25]   O. Sobol, Hydrogen Assisted Cracking and Transport Studied by ToF-SIMS and Data Fusion with HR-SEM, (2017) 142.

4.5 Manuscript 4 - Effect of Strain and Austenite Morphology on the Anodic Dissolution Behaviour of Ferrite Under Salt-Laden Deposits

P. Reccagni[a],*, Q. Lu[b], M. F. Gittos[b], D.L. Engelberg[a]

[a] Corrosion and Protection Centre, University of Manchester, UK

[b] TWI, Cambridge, UK

4.5.1 Abstract

Duplex stainless steels (DSSs) are widely used in the oil and gas industry, where the high strength and corrosion resistance makes them a viable choice for structural applications. The phase balance of this alloys is significantly affected by arc-welding, a joining technique commonly used to fabricate complex structures. The phase balance and morphology in the Heat Affected Zone of DSS weld is characterized by increased ferrite fraction and by enhanced susceptibility to Stress Corrosion Cracking (SCC). The active dissolution of the ferritic phase, in particular, is one of the forms of localised corrosion that can act as precursors for SCC exposed to chloride rich salt-laden deposits exposed to atmospheric conditions. The effect of austenite morphology on the selective dissolution of ferrite is investigated in this paper.

Mini-tensile samples of a multi-pass TIG weld have been used to investigate the anodic dissolution of the ferrite surrounding different austenite morphologies. The weld and the base metal were strained in a static tensile rig while being exposed to $MgCl_2$ droplets under controlled atmospheric conditions. The morphology of the corrosion attack was characterized using SEM-EBSD

4.5.2 Introduction

Duplex stainless steels have outstanding resistance to stress corrosion cracking in chlorides containing environments and are generally considered resistant to this type of failure at low and intermediate temperatures [1]. More recently, susceptibility to SCC of duplex steels under salt-laden deposits at temperatures below 100°C has been reported by different authors [2,3], prompting further investigations into their behaviour at low temperatures.

The HAZs of welded duplex structure – even in cases where the resulting microstructure is acceptable according to the current welding standards [4] – is often a region of reduced corrosion resistance [5.6]. While the detrimental effect of reduced austenite content in the HAZ is well known [1,7], limited attention has been addressed to the effects of austenite morphology [8].

The morphology of corrosion attacks in ferrite – that can act as precursors to stress corrosion cracks initiation – is the main interest of this paper. In particular, the relationship between ferrite dissolution morphology and austenite distribution with respect to the applied stress direction is investigated. Atmospheric exposure of a duplex stainless steel weld under $MgCl_2$-laden deposits at 80 °C is used to promote localised corrosion attacks. The morphology of the corrosion attacks in then characterized using SEM imaging and SEM-EBSD.

4.5.3 Methodology

4.5.3.1 Materials and Characterization

The material used was a duplex stainless steel grade 2205 (UNS S1803) in the form of a pipe (9.2 mm wall thickness) with chemical composition (in %wt.) of 22.0Cr, 5.2Ni, 2.75Mo,

1.48Mn, 0.02C, 0.18N and Fe (bal.). Two sections cut from the same pipe were joined with a multi-pass TIG girth weld (a detailed description of the welding process is provided in chapter 4.1). Mini-tensile sample were EDM cut from transversally across the weld, in order to expose all the regions of the weld and the base metal on both sides. The samples used for characterization were wet ground with SiC paper (up to 4000 grit) and polished with diamond paste (3 and 1 μm) followed by fine polishing in colloidal silica suspension (20-40nm) for 30 minutes. EBSD phase maps of the heat affected zone were acquired using a FEI Quanta650 FEG-SEM, equipped with a Nordlys EBSD detector from Oxford Instruments. Samples used for atmospheric exposure were prepared in a similar way, with the final silica polishing –required for EBSD characterization – performed after the corrosion attacks were produced.

4.5.3.2 Atmospheric-Induced Stress corrosion cracking

Atmospheric exposure under salt-laden deposits was used to promote AI-SCC attacks on mini-tensile samples of the weld. 1μL Droplets of 0.1M $MgCl_2$ - providing a deposition density of ca. 400 μgL-1 - were placed in different positions of the weld mini-tensile sample, exposing the parent material and the HAZ. The tensile sample was then exposed to constant strain in a static tensile rig [9], with an applied deformation of approximately 3% of the original dimensions (the strain has been estimated using optical images of the sample before and after closing the rig). The tensile rig was placed in a humidity chamber at 80 °C temperature and 30% relative humidity (deliquescence humidity of the $MgCl_2$ salt). Samples have been exposed for 3 months. The corrosion attacks have been characterised with the same techniques, after removal of the corrosion products by ultrasonic cleaning in 2M citric acid solution at 60 °C and fine polishing in colloidal silica. An image of the tensile rig with the sample and the applied droplets is shown in Figure 67.
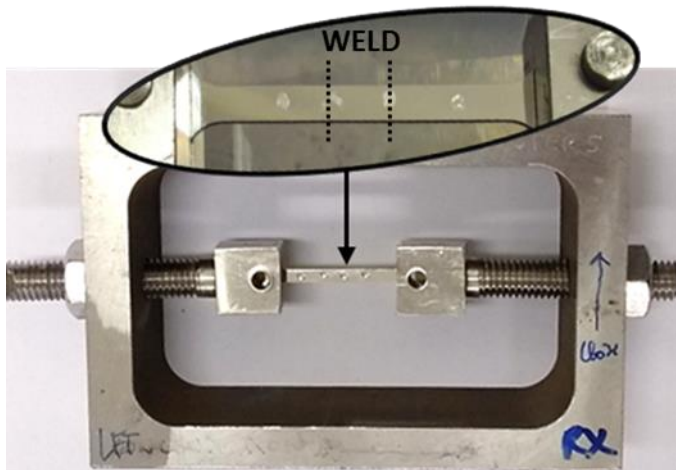
Figure 67 - Tensile rig with mini-tensile sample assembled and detail of the MgCl2 droplets.

4.5.4   Results

4.5.4.1 Materials

An EBSD phase map representative of the weld microstructure is shown in Figure 68. Typical features of DSS welds are visible, with the progressive change in morphology from the base metal approaching the fusion line (high temperature heat affected zone), followed by a completely different microstructure in the weld. The presence of sigma- and chi-phases was excluded in this region (i.e. these phases were not indexed by EBSD).
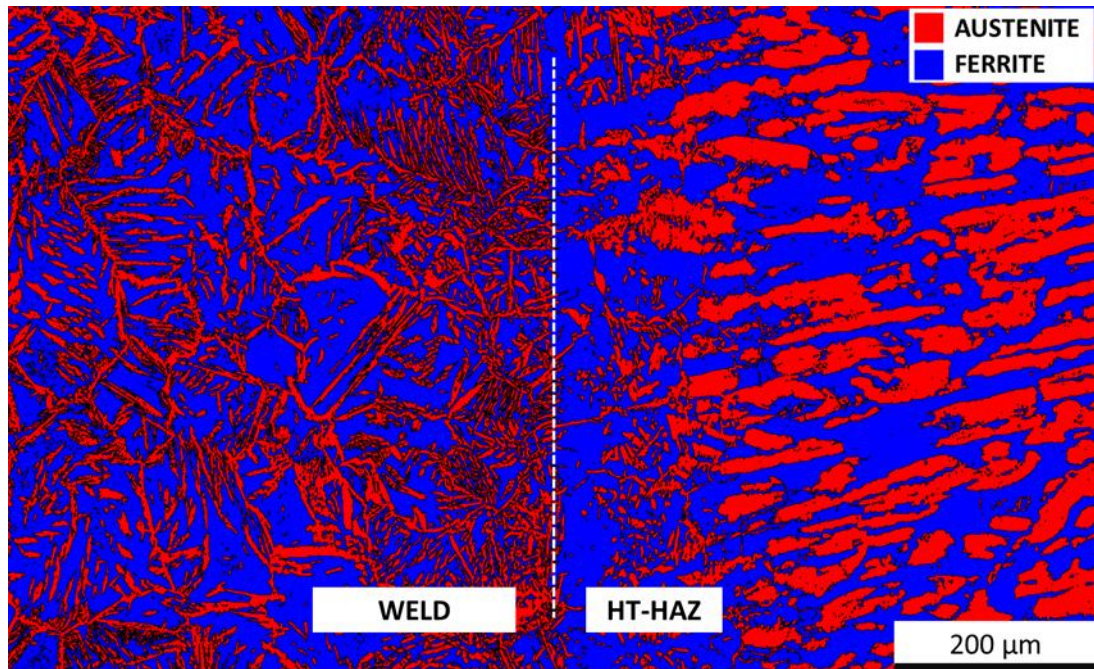
Figure 68 - Austenite and ferrite morphology in the weld, HAZ and base metal. EBSD phase map.

4.5.4.2 Atmospheric Corrosion

(i)   Parent Material

 The main constituent phases in the parent material were affected differently by the atmospheric exposure. Under the chlorides bearing deposit, corrosion in the ferrite occurred in the form of selective dissolution, which was confined by the adjacent austenite grains. In the austenite there was no evidence of uniform corrosion, while cracks were noticed on the surface. Cracks opened and progressed in direction perpendicular to the applied strain, as shown in Figure 69.
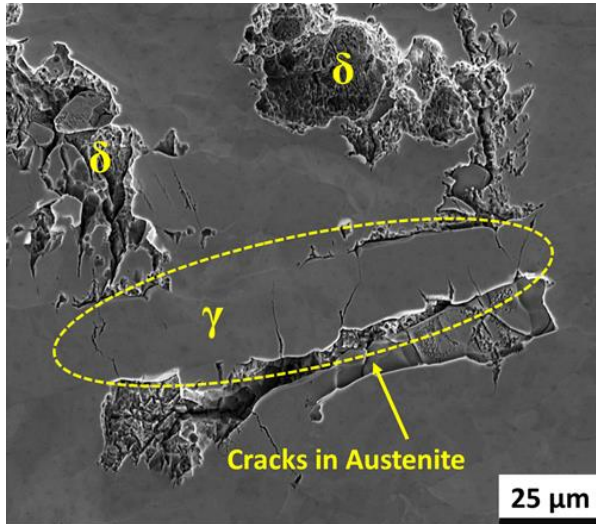
Figure 69 - Corrosion under the salt deposit in the base metal. Strain axis horizontal to the picture.

The initiation stage of the cracks in austenite was visible in some regions of the corrosion attack. Cracks initiated preferentially at the phase boundaries with ferritic grains where selective dissolution of this phase had occurred. A detail of crack initiation is shown in Figure 70.
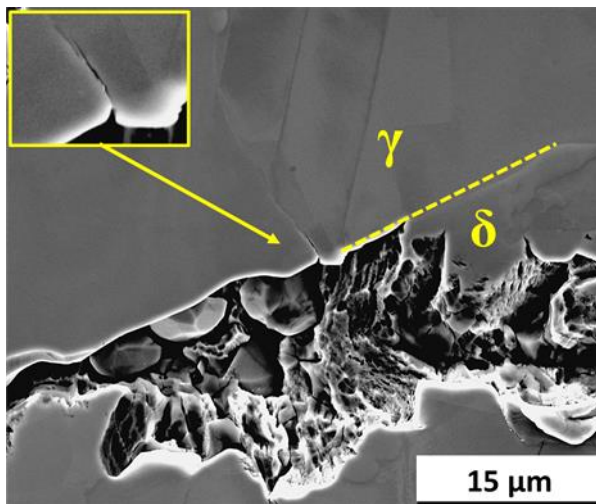
Figure 70 - Anodic dissolution of ferrite and crack initiation in austenite in the base metal.

The EBSD characterization of the crystallographic character of the cracks in austenite revealed both intergranular and transgranular cracks in this phase, suggesting a mixed-mode failure. An example is shown in Figure 71.
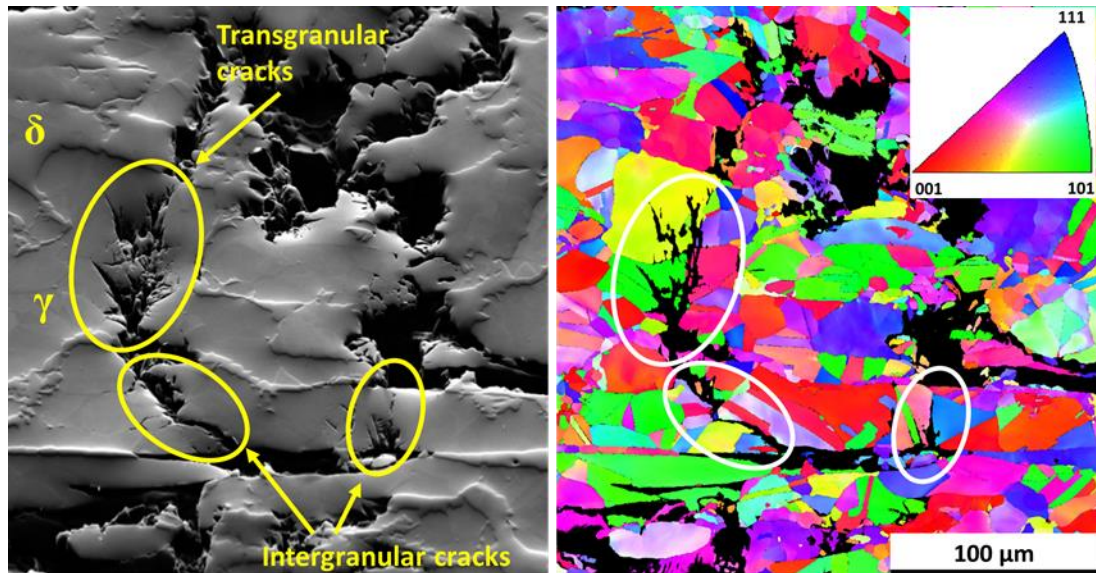
Figure 71 - Selective dissolution of ferrite and cracks in austenite in the base metal. IPF-Z grains map showing the mixed-mode nature of the cracks in austenite. Strain axis horizontal to the picture.

(ii)   WELD

The droplet placed on the weld and heat affected zone of the sample caused significant corrosion attack in the weld rather than in the heat affected zone – most likely caused by misalignment in the experimental setup. A sketch of the area covered by the droplet with respect to the sample etched macrograph is shown in Figure 72.
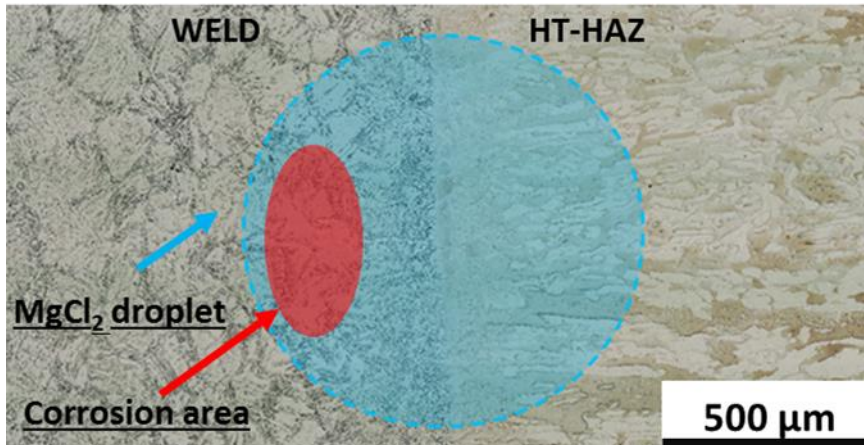
Figure 72 - Location of corrosion attack and salt-laden deposit (droplet) with respect to the weld microstructure. Strain axis horizontal to the picture.

Selective dissolution of the ferrite and cracks in austenite were the types of attack found also in this region. Similarly to what observed in the base metal, cracks perpendicular to the stress direction were found in the austenite plates elongated in the direction of the applied stress – an example is shown in Figure 73. Also in this case, ferrite dissolution was observed in the neighbouring regions.
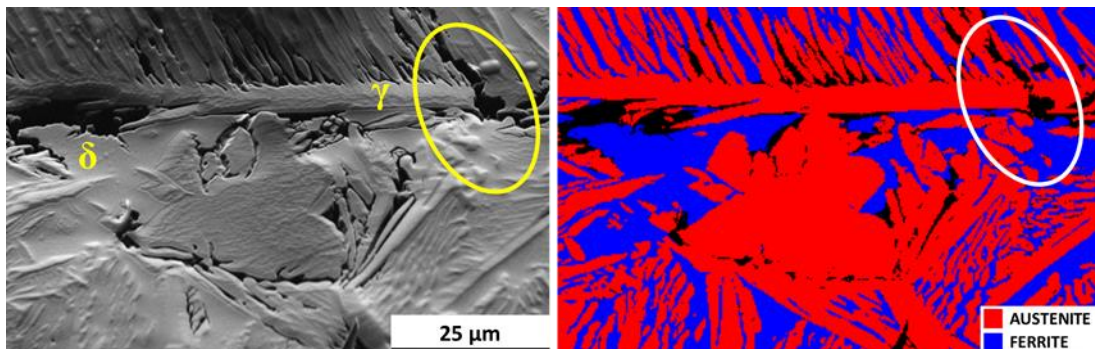
Figure 73 - Selective dissolution of ferrite and crack and cracks in austenite perpendicular to the strain direction .Strain axis horizontal to the picture.

In the weld metal, austenite is distributed homogeneously in all directions and it is possible to distinguish also grains with the longest dimension opposing the strain direction. Cracking in these plates did not occur, likely due to the unfavourable geometry. However, a different

morphology of ferrite dissolution was noticed at the phase boundaries of these grains – an example is shown in Figure 74.
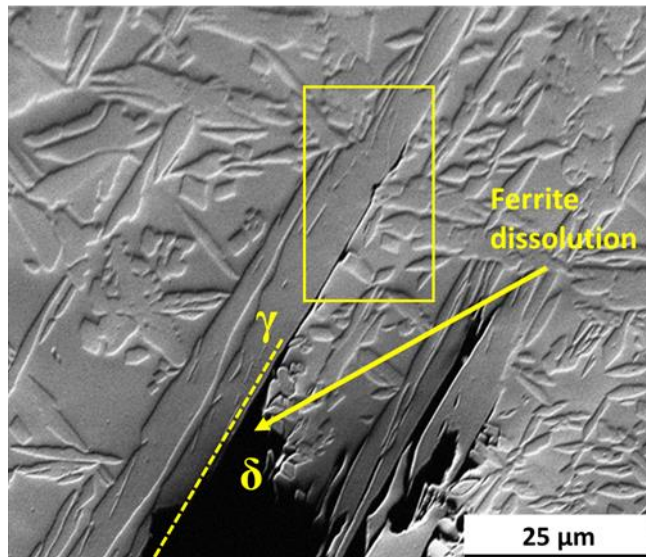
Figure 74 – Progression of selective dissolution attack in austenite following sharply the phase boundaries. Strain axis horizontal to the picture.

In these regions, the austenite plates are oriented in a way that results in significant tensile stress component normal to the phase boundaries. Under these conditions, the anodic dissolution of ferrite followed sharply the phase boundaries with austenite, rather than progressing uniformly in all directions. A details of the corrosion attack progression is shown in Figure 75, where the EBSD phase maps of the region confirms the preferential dissolution of ferrite at the phase boundary rather than in the adjacent ferritic grains.
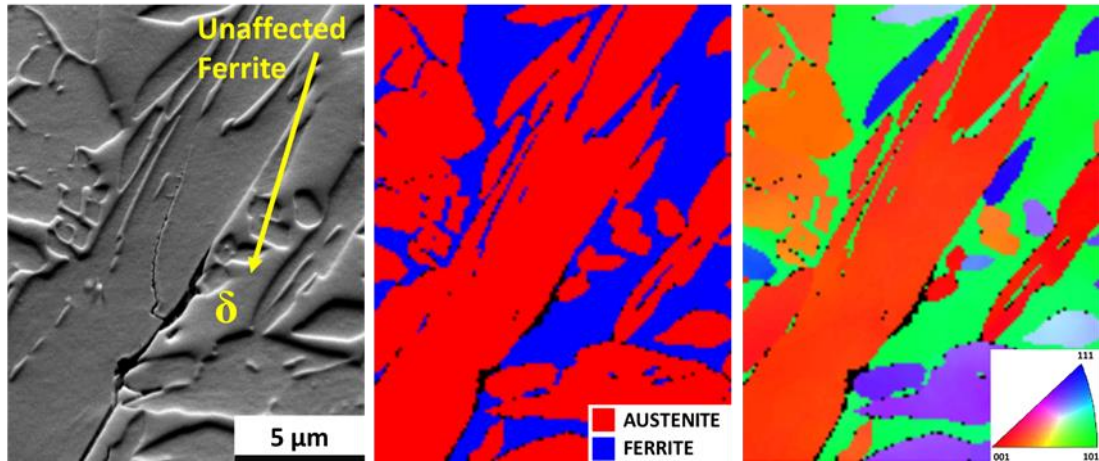
Figure 75 - Anodic dissolution of ferrite following the austenite:ferrite phase boundary. Strain axis horizontal to the picture.

4.5.5   Discussion

The anodic or cathodic character of DSS constituent phases is a property determined by the environment in which they are exposed[10]. In concentrated acidic and near-neutral chlorides rich solutions, ferrite assumes anodic behaviour with respect to the austenite and selective dissolution of the ferritic phase is routinely observed under chloride salts deposits in evaporative conditions [3,9,11,12]. In these environments, selective dissolution of ferrite can act as a precursor and participate in the initiation and progression of cracks through this phase [3,8]. In this work, the morphology of the ferrite dissolution under MgCl2 deposits under atmospheric exposure at the salt deliquescence humidity has been investigated in the base metal and in the high-temperature heat affected zone of a TIG welded duplex steel.

In the base metal, ferrite dissolution was the predominant corrosion mechanism observed, consistent with the anodic behaviour of the phase expected in these conditions. The cracks found in austenite initiated at the phase boundaries with areas of dissolved ferrite. The concentration of the anodic activity in the ferrite phase, due to the different nobility of the two phases, suggests that the formation of cracks in austenite is unlikely occur

163

simultaneously. Crack initiation in austenite is more likely a secondary effect, possibly aided by the replacement of the ferrite on the adjacent surface with corrosion products, altering locally the austenite:ferrite galvanic cell.

The corrosion attack in the weld developed following the same principles, with areas of corroded ferrite surrounding the grains of reformed austenite. The morphology of the ferrite dissolution, however, highlighted a strong dependence on the austenite morphology. The ferrite surrounding austenite plates elongated in direction (close to-) normal to the strain direction, in particular, showed propensity for the anodic dissolution to follow the phase boundaries and form narrow region of preferential corrosion.

This can be explained combining mechanical and electrochemical observations. When duplex microstructure are subjected to macroscopic strain, the load is shared differently by the two phases due to their different mechanical and crystallographic properties. As a result, heterogeneous strain field develop at the phase boundaries [13], which can act as regions of stress intensification and potentially enhance the rate of anodic dissolution [14,15]. Macroscopic deformation cause also the rupture and reformation of the passive film on the surface. The quality of the passive film reformed on strained DSS2205 grade offers lower corrosion resistance in acidic chlorides-rich electrolytes [16], with the difference in galvanic activity between the two phases also decreasing [17,18] . The combination of localised stress and deteriorated passive film quality in this region is consistent with the enhanced dissolution observed.

Grain boundary austenite has been shown by other authors to be a preferred path for stress corrosion cracking [8]. Grain boundary austenite forms in the heat affected zone and surrounds ferritic grains, forming path of thin austenite plates in all directions. The combination of stress direction and anodic activity can help explaining why the GBA phase boundaries show enhanced susceptibility.

4.5.6   Conclusions

- Austenite distribution has a significant role in defining the morphology of selective dissolution in ferrite;

- The combination of austenite morphology and stress direction showed increased corrosion rate of the ferrite surrounding the phase boundaries of austenite plates subjected to tensile stress components;

- The combined effect of stress and microstructure inhomogeneity, suggests that austenite:ferrite boundaries in this geometry becomes preferential path for corrosion attacks progression;

- The role of ferrite dissolution as a precursor to stress corrosion cracks formation suggest that the austenite morphology could play a significant role in SCC progression in the HAZ;

4.5.7 References

[1]   R.A. Cottis, R.C. Newman, Stress Corrosion Cracking Resistance of Duplex Stainless Steels, Health and Safety Executive - Offshore Technology Report, 1993.

[2]   C. Örnek, X. Zhong, D.L. Engelberg, Low-Temperature Environmentally Assisted Cracking of Grade 2205 Duplex Stainless Steel Beneath a MgCl 2 :FeCl 3 Salt Droplet, Corrosion. 72 (2016) 384–399. doi:10.5006/1888.

[3]   C. Lojewski, S. Le Manchet, T. Snauwaert, F. Maas, D. Thierry, E. Johansson, T. Prosek, A. Fanica, F. Dupoiron, B. Droesbeke, C. Canderyd, A. Le Gac, Low-Temperature Stress Corrosion Cracking of Austenitic and Duplex Stainless Steels Under Chloride Deposits, Corrosion. 70 (2014) 1052–1063. doi:10.5006/1242.

[4]   V.. Linton, N.. Laycock, S.. Thomsen, a Klumpers, Failure of a super duplex stainless steel   reaction   vessel,   Eng.   Fail.   Anal.   11   (2004)   243–256. doi:10.1016/j.engfailanal.2003.05.011.

[5]   V.A. Hosseini, K. Hurtig, L. Karlsson, Effect of multipass TIG welding on the corrosion resistance and microstructure of a super duplex stainless steel, Mater. Corros. 68 (2017) 405–415. doi:10.1002/maco.201609102.

[6]   A. Turnbull, A. Griffiths, B. Hawkins, L. Orkney, P. Francis, M. Ryan, A Novel Approach to Characterizing the Corrosion Resistance of Super Duplex Stainless Steel Welds, Corrosion. 58 (2002) 1039–1048. doi:10.5006/1.3280793.

[7]   W.A. Baeslack, D.J. Duquette, W.F. Savage, The Effect of Ferrite Content on Stress Corrosion Cracking in Duplex Stainless Steel Weld Metals at Room Temperature, Corros. Nace. 35 (1979) 45–54.

[8]   H.-Y. Liou, R.-I. Hsieh, W.-T. Tsai, Microstructure and stress corrosion cracking in simulated heat-affected zones of duplex stainless steels, Corros. Sci. 44 (2002) 2841–2856. doi:10.1016/S0010-938X(02)00068-9.

[9]   D.L. Engelberg, C. Örnek, Probing propensity of grade 2205 duplex stainless steel towards atmospheric chloride-induced stress corrosion cracking, Corros. Eng. Sci. Technol. 49 (2014) 535–539. doi:10.1179/1743278214Y.0000000205.

[10]   S.S.M. Tavares, V.G. Silva, J.M. Pardal, J.S. Corte, Investigation of stress corrosion cracks in a UNS S32750 superduplex stainless steel, Eng. Fail. Anal. 35 (2013) 88–94. doi:10.1016/j.engfailanal.2012.12.013.

[11]   W.-T. Tsai, M.-S. Chen, Stress corrosion cracking behavior of 2205 duplex stainless steel in concentrated NaCl solution, Corros. Sci. 42 (2000) 545–559. doi:10.1016/S0010-938X(99)00105-5.

[12]   W.-T. Tsai, S.-L. Chou, Environmentally assisted cracking behavior of duplex stainless steel in concentrated sodium chloride solution, Corros. Sci. 42 (2000) 1741–1762. doi:10.1016/S0010-938X(00)00029-9.

[13]   A. EL BARTALI, V. AUBIN, S. DEGALLAIX, Fatigue damage analysis in a duplex stainless steel by digital image correlation technique, Fatigue Fract. Eng. Mater. Struct. 31 (2008) 137–151. doi:10.1111/j.1460-2695.2007.01207.x.

[14]   T.P. Hoar, J.C. Scully, Mechanochemical Anodic Dissolution of Austenitic Stainless Steel in Hot Chloride Solution at Controlled Electrode Potential, J. Electrochem. Soc. 111 (2007) 348. doi:10.1149/1.2426120.

[15]   M. Sahal, J. Creus, R. Sabot, X. Feaugas, Consequences of plastic strain on the dissolution process of polycrystalline nickel in H2SO4 solution, Scr. Mater. 51 (2004) 869–873. doi:10.1016/j.scriptamat.2004.07.004.

[16]   J. Yang, Q. Wang, K. Guan, Effect of stress and strain on corrosion resistance of duplex stainless steel, Int. J. Press. Vessel. Pip. 110 (2013) 72–76. doi:10.1016/j.ijpvp.2013.04.025.

[17]   C. Örnek, D.L. Engelberg, An experimental investigation into strain and stress partitioning of duplex stainless steel using digital image correlation, X-ray diffraction and scanning Kelvin probe force microscopy, J. Strain Anal. Eng. Des. 51 (2016) 207–219. doi:10.1177/0309324716631669.

[18]   R.J. Wang, J.X. Li, Y.J. Su, L.J. Qiao, A.A. Volinsky, Changes of Work Function in Different Deformation Stage for 2205 Duplex Stainless Steel by SKPFM, Procedia Mater. Sci. 3 (2014) 1736–1741. doi:10.1016/j.mspro.2014.06.280.

5 SUMMARY AND CONCLUSIONS

The work presented in this thesis has been designed with the aim to increase the understanding of the relationships between welding heat input, microstructure morphology and EAC resistance of duplex stainless steel 2205 welds. The work followed two directions, with fundamental properties of the weld studied on simulated HAZs and the performance testing carried out on a real-scale multipass weld. Together, the chapters provide an overview of the microstructure evolution in welding and corrosion resistance of different austenite morphologies, with particular attention to SCC and Hydrogen Embrittlement.

The first part of the project focused on the manufacturing and the characterization of a reference weld. The material was used as a microstructure of reference and for all corrosion testing (manuscripts 3 and 4), where hydrogen embrittlement and selective ferrite dissolution have been investigated. In a second part, GLEEBLE simulated heat affected zones were used,offering the possibility to look at fundamental properties of HAZs produced with great control of the thermal history applied. A significant finding obtained using these microstructures – presented in Manuscript 2 – is the reduction in galvanic activity between austenite and ferrite in the HAZ. This forms a significant contribution to the electrochemical theory of stress corrosion cracking in duplex stainless steel and can, in part, explain why weldments with acceptable austenite content are still more susceptible to cracking in this regions. Owing to the homogeneity of the microstructures produced with the GLEEBLE simulator, the characterization of the electrochemical properties is not influenced by local variation of microstructure morphology within the investigated areas and the theory behind the results can be generalized.

The types of microstructure morphologies defined on the simulated microstructures in manuscript 1 were investigated in the context of hydrogen assisted cracking (HAC) on a real-scale weld in manuscript 3. This part of the project was developed using an extensive combination of test methods and characterization techniques. Findings showed the inferior HAC resistance of grain boundary austenite (GBA) with respect to coarser austenite islands. Considering these findings with GBA route of formation (manuscript 1), it seems that higher heat inputs would have preventative effects on HAC susceptibility. Sensitization by chromium (II) nitrides, however, is a threat that needs also to be considered in designing the welding procedure.

The early stages of atmospheric induced stress corrosion cracking have been investigated on a real-scale weld in manuscript 4. This part of the thesis presents a discussion on the synergic effects of stress and microstructure on the ferrite selective dissolution, which is often a precursor to AI-SCC cracks formation under the crevices formed by salt deposits. A direct correlation with the austenite morphologies described in manuscript 1 was not possible in this case but the manuscript forms a basis to explain the propensity of GBA phase boundaries to become cracking path found in literature. The main objective of this work was to provide an original observation of different microstructural features involved in the EAC of duplex stainless steel weldments. The outcome of this work, as a result, is an organized morphological description of austenite behaviour in different types of corrosion. In order to provide a comprehensive observation, different corrosion mechanisms and different characterization techniques have been used in the same project. As a result, this thesis offers an observation of the same microstructural descriptors in different contexts, providing a "big picture" of the relationship between welding, austenite morphology and corrosion resistance.

The breadth of the topic investigated resulted in a lack of statistical confirmation of the observations formulated. While this is an evident limitation of the thesis, the work carried out showed the potential for new research topics in the DSS welding, which was made possible by observing the multiple aspects of the EAC-microstructure relationship at the same time.

The results offer a promising indication that GBA is to some extent less protective than coarse austenite plates, suggesting possibly that this form of austenite – despite maintaining cathodic character with respect to the ferrite - should be accounted for differently in weld qualifications. In the case of hydrogen embrittlement attacks in the HAZ, the resistance to the crack path offered by this form of austenite is almost negligible. With respect to AI-SCC, only the role of austenite in ferrite selective dissolution – as a precursor to cracking – was investigated, showing that phase boundaries have the potential to act as pre-formed paths for cracking. Also in this regard, GBA is potentially detrimental due to its formation surrounding ferritic grains in all directions, including normal to tensile residual or external stresses.The main conclusions can be summarized as:

- Small heat inputs result in heat affected zone containing higher fractions of grain boundary austenite;

- GBA showed limited resistance to hydrogen assisted cracking attacks of the heat affected zone;

- Large heat inputs, which promote smaller fractions of GBA, are associated with precipitation of chromium(II) nitrides, limiting the choice of cooling times allowable;

- The galvanic activity between the two phases of a duplex steel is markedly reduced in the HAZ of the weld. This is inherently detrimental to stress corrosion cracking,

due to the reduction of the driving force for galvanic protection of one phase over the other;

- The presence of GBA or, in general, of elongated austenite plates has a potential to offer preferred cracking paths, due to the stress-assisted enhanced ferrite dissolution following the phase boundaries;

-

6 FUTURE WORKS

The overarching aim of the project was to improve the knowledge of how the welding process causes reduced EAC resistance in the heat affected zone of weldments. The research followed two main directions. Initially, fundamental properties of the heat affected zones have been studied using simulated microstructures. In a second part of the project, the behaviour of austenite morphologies in different types of corrosion attacks has been investigated.

The breadth of the field investigated with this research presents the opportunity to use some of the findings as foundation for future studies, given the opportunity to continue with this research. In particular, the following ways to expand the project have been identified.

(i) Further parameters affecting austenite evolution in the HAZ could be investigated. In particular, the effects of tensile/compressive stress - reproducing the thermal stress in a real weld HAZ – on the dynamic recrystallization of austenite during cooling should be investigated. This would constitute a significant addition to the description of the austenite morphology evolution in the HAZ.

(ii) The investigation on the effects of welding on the internal galvanic activity of the duplex alloy showed a clear reduction, confirmed with different techniques. A significant addition to the topic would be constituted by performing the same electrochemical characterization on different regions of an actual weld, in order to confirm the importance of the results for practical welds.

(iii)   The hydrogen assisted cracking study proposed in this thesis shows interesting indications on how the austenite morphology plays a relevant role in the weld HAC resistance. However, the hydrogen charging conditions used were significantly harsher than the the ones normally encountered in applications where cathodic protection is used. It would be potentially interesting to compare the cracking path found in this work with cracks promoted at more moderate overprotection potential in order to verify that the mild opposition to cracking provided by GBA is confirmed at lower disoolved hydrogen densities. In addition, the effcts of the strain rate have not been included in this project; an additional compariston with more conventional SSRTs test at the cathodic protection potential routinely used to assess and rank alloys HAC resistance could benefit the discussion.

(iv)   The assessment of the AI-SCC resistance performed on the reference weld did not allow to visualize directly the role of grain boundary austenite in stress corrosion cracks progression. Due to time limitation, it was not possible to vary the exposure condition or to perform FIB cross sectioning in order to look at the ferrite dissolution below the surface. Further, the exposure to salt-laden deposits within a realistic time-scale promotes cracks only in the near surface. A significant addition would be the SCC testing of the welds, both real and simulated, in environments producing more severe attacks – such as boiling salt solutions combined with testile strain. This would help to expand the understanding of the role of austenite:ferrite phase boundaries in stress corrosion cracks progression in macroscopic SCC cracks.

7 BIBLIOGRAPHY

[1]   R.N. Gunn, Developments, grades and specifications, Duplex Stainl. Steel. Microstruture, Prop. Appl. (1997) 1–13. doi:10.1533/9781845698775.1.

[2]   C.O.A. Olsson, D. Landolt, Passive films on stainless steels - Chemistry, structure and growth, Electrochim. Acta. 48 (2003) 1093–1104. doi:10.1016/S0013-4686(02)00841-1.

[3]   V.A. Hosseini, L. Karlsson, K. Hurtig, I. Choquet, D. Engelberg, M.J. Roy, C. Kumara, A novel arc heat treatment technique for producing graded microstructures through controlled temperature gradients, Mater. Des. 121 (2017) 11–23. doi:10.1016/j.matdes.2017.02.042.

[4]   R.N. Gunn, Welding metallurgy, in: Duplex Stainl. Steels, w, Abington, England, 1997: pp. 110–132. doi:10.1533/9781845698775.110.

[5]   BS-EN-ISO, Specification and qualification of welding procedures for metallic materials — Welding procedure test —, (2012) 1–32.

[6]   S. Edition, Metallurgy Second Edition Welding Metallurgy, Structure. 822 (2003) 466. doi:10.1016/j.theochem.2007.07.017.

[7]   R. Bernhardsson, A.M. Evaluating, A Method of Evaluating Polarization Curves for Stainless Steel via a Sinnple Passivation Model, (1981) 352–364.

[8]   R.F. Steigerwald, Effect of Cr Content On Pitting Behavior of Fe-Cr Alloys, Corrosion. 22 (1966) 107–112. http://www.corrosionjournal.org/doi/abs/10.5006/0010-9312-22.4.107?=.

[9]   M.H. Moayed, R.C. Newman, Evolution of current transients and morphology of metastable and stable pitting on stainless steel near the critical pitting temperature, Corros. Sci. 48 (2006) 1004–1018. doi:10.1016/j.corsci.2005.03.002.

[10]   A.L.. Schaeffler, Constitution Diagram for Stainless-steel Weld Metal. 2. Schaeffler DiagramNo Title, Met. Prog. 106(1) (1974).

[11]   D. Kotecki, T. Siewert, WRC-1992 constitution diagram for stainless steel weld metals: a modification of the WRC-1988 diagram, Weld. J. (1992) 171–178. http://www.aws.org/w/a/wj/supplement/WJ_1992_05_s171.pdf.

[12]   L. Gardner, The use of stainless steel in structures, Prog. Struct. Eng. Mater. 7 (2005) 45–55. doi:10.1002/pse.190.

[13]   Retained Austenite as a Hydrogen Trap in Steel Welds, (n.d.) 27–35.

[14]   R.N. Gunn, Microstructure, in: Duplex Stainl. Steels, Woodhead Publishing Limited, 1997: pp. 24–49. doi:10.1533/9781845698775.24.

[15]   M. Theofanous, L. Gardner, Testing and numerical modelling of lean duplex stainless steel hollow section columns, Eng. Struct. 31 (2009) 3047–3058. doi:10.1016/j.engstruct.2009.08.004.

[16]   R. a Perren, T. a Suter, P.J. Uggowitzer, L. Weber, R. Magdowski, H. Böhni, M.O. Speidel, Corrosion resistance of super duplex stainless steels in chloride ion containing environments: investigations by means of a new microelectrochemical method.II. In�uence of precipitates, Corros. Sci. 43 (2001) 727–745. 0824R%5Cn0823R.

[17]   I. Mészáros, P.J. Szabó, Complex magnetic and microstructural investigation of duplex stainless steel, NDT E Int. 38 (2005) 517–521. doi:10.1016/j.ndteint.2004.12.007.

[18]   R. Pettersson, O.S. Ab, Corrosion performance of welds in duplex , superduplex and lean duplex stainless steels Corrosion performance of welds in duplex , superduplex and lean duplex stainless steels, (2014) 1–8.

[19]   S. Atamert, J.E. King, Elemental partitioning and microstructural development in duplex stainless steel weld metal, Acta Metall. Mater. 39 (1991) 273–285. doi:10.1016/0956-7151(91)90306-L.

[20]   L. Weber, P.J. Uggowitzer, Partitioning of chromium and molybdenum in super duplex stainless steels with respect to nitrogen and nickel content, Mater. Sci. Eng. A. 242 (1998) 222–229. doi:10.1016/S0921-5093(97)00521-2.

[21]   Z. Zhang, H. Jing, L. Xu, Y. Han, L. Zhao, J. Zhang, Influence of microstructure and elemental partitioning on pitting corrosion resistance of duplex stainless steel welding joints, Appl. Surf. Sci. 394 (2017) 297–314. doi:10.1016/j.apsusc.2016.10.047.

[22]   K. Chan, S. Tjong, Effect of Secondary Phase Precipitation on the Corrosion Behavior of Duplex Stainless Steels, Materials (Basel). 7 (2014) 5268–5304. doi:10.3390/ma7075268.

[23]   a J. Ramirez, The Relationship between Chromium Nitride and Secondary\nAustenite Precipitation in Duplex Stainless Steels, Metall. Mater. Trans. A. 34A (2003) 1575–1597.

[24]   Handbook of Stainless Steel, Outukumpu, Outukumpu Oyj, Avesta, Sweden, 2013.

[25]   R.N. Gunn, Alloy design, in: Duplex Stainl. Steels, Woodhead Publishing Limited, Abington, England, 1997: pp. 14–23. doi:10.1533/9781845698775.14.

[26]   T.J. Mesquita, E. Chauveau, M. Mantel, R.P. Nogueira, A XPS study of the Mo effect on passivation behaviors for highly controlled stainless steels in neutral and alkaline

conditions, Appl. Surf. Sci. 270 (2013) 90–97. doi:10.1016/j.apsusc.2012.12.118.

[27]   D.M. Escriba, E. Materna-Morris, R.L. Plaut, a. F. Padilha, Chi-phase precipitation in a duplex stainless steel, Mater. Charact. 60 (2009) 1214–1219. doi:10.1016/j.matchar.2009.04.013.

[28]   D.M. Escriba, E. Materna-Morris, R.L. Plaut, A.F. Padilha, Intermetallic Phase Precipitation in Duplex Stainless Steels during High Temperature Exposition, Mater. Sci. Forum. 636–637 (2010) 478–484. doi:10.4028/www.scientific.net/MSF.636-637.478.

[29]   V. A. Hosseini, L. Karlsson, C. Örnek, P. Reccagni, S. Wessman, D. Engelberg, Microstructure and functionality of a uniquely graded super duplex stainless steel designed by a novel arc heat treatment method, Mater. Charact. 139 (2018). doi:10.1016/j.matchar.2018.03.024.

[30]   J. Michalska, M. Soza, Qualitative and quantitative analysis of σ and χ phases in 2205 duplex stainless steel, Mater. Charact. 56 (2006) 355–362. doi:10.1016/j.matchar.2005.11.003.

[31]   T.. Palmer, J.. Elmer, S.. Babu, Observations of ferrite/austenite transformations in the heat affected zone of 2205 duplex stainless steel spot welds using time resolved X-ray diffraction, Mater. Sci. Eng. A. 374 (2004) 307–321. doi:10.1016/j.msea.2004.03.037.

[32]   H. Sieurin, R. Sandström, Sigma phase precipitation in duplex stainless steel 2205, Mater. Sci. Eng. A. 444 (2007) 271–276. doi:10.1016/j.msea.2006.08.107.

[33]   J.S. Kaspert, The Ordering of Atoms in the Chi-Phase of the Iron-Chromium-Molybdenum System, Acta Metall. 2 (1954) 456–461.

[34]   E.M.L.E.M. Jackson, P.E. d. Visser, L. a. Cornish, Distinguishing between Chi and

Sigma phases in duplex stainless steels using potentiostatic etching, Mater. Charact. 31 (1993) 185–190. doi:10.1016/1044-5803(93)90061-Y.

[35]   X.Z. Liang, M.F. Dodge, W. Liang, H.B. Dong, Precipitation of chromium nitride nano-rods on lamellar carbides along austenite-ferrite boundaries in super duplex stainless steel, Scr. Mater. 127 (2017) 45–48. doi:10.1016/j.scriptamat.2016.09.004.

[36]   N. Sathirachinda, R. Pettersson, S. Wessman, J. Pan, Study of nobility of chromium nitrides in isothermally aged duplex stainless steels by using SKPFM and SEM/EDS, Corros. Sci. 52 (2010) 179–186. doi:10.1016/j.corsci.2009.08.057.

[37]   J.J. Shiao, C.H. Tsai, J.H. Huang, J.J. Kai, Phase transformations in ferrite phase of a duplex stainless steel aged at 500C, Scr. Metall. Mater. 29 (1993) 1451–1456. doi:10.1016/0956-716X(93)90335-P.

[38]   F. Iacoviello, F. Casari, S. Gialanella, Effect of "475 °C embrittlement" on duplex stainless steels localized corrosion resistance, Corros. Sci. 47 (2005) 909–922. doi:10.1016/j.corsci.2004.06.012.

[39]   C. Örnek, D.L. Engelberg, S.B. Lyon, T.L. Ladwein, Effect of " 475 ° C Embrittlement " on the Corrosion Behaviour of Grade 2205 Duplex Stainless Steel Investigated Using Local Probing Techniques, (n.d.) 2–6.

[40]   S. Hertzman, P.J. Ferreira, B. Brolund, An Experimental and Theoretical Study of Heat-Affected Zone Austenite Reformation in Three Duplex Stainless Steels, Metall. Mater. Trans. A. 28 (1997) 277–285.

[41]   V. Muthupandi, P. Bala Srinivasan, S.K. Seshadri, S. Sundaresan, Effect of weld metal chemistry and heat input on the structure and properties of duplex stainless steel welds, Mater. Sci. Eng. A. 358 (2003) 9–16. doi:10.1016/S0921-5093(03)00077-7.

[42]   A.J.W. Menezes, H. Abreu, S. Kundu, H.K.D.H. Bhadeshia, P.M. Kelly, Crystallography

of Widmanstätten austenite in duplex stainless steel weld metal, Sci. Technol. Weld. Join. 14 (2009) 4–10. doi:10.1179/136217108X341166.

[43]   H.-Y. Liou, R.-I. Hsieh, W.-T. Tsai, Microstructure and stress corrosion cracking in simulated heat-affected zones of duplex stainless steels, Corros. Sci. 44 (2002) 2841–2856. doi:10.1016/S0010-938X(02)00068-9.

[44]   G.S. Frankel, R.A. Cottis, Shreir's Corrosion, in: Vol. 2, Fourth Edi, Elsevier Science S.A., 2010.

[45]   B.E. Conway, G. Jerkiewicz, Thermodynamic and electrode kinetic factors in cathodic hydrogen sorption into metals and its relationship to hydrogen adsorption and poisoning, J. Electroanal. Chem. 357 (1993) 47–66. doi:10.1016/0022-0728(93)80373-P.

[46]   J.R. Galvele, Transport Processes and the Mechanism of Pitting of Metals, J. Electrochem. Soc. 123 (1976) 464. doi:10.1149/1.2132857.

[47]   J.W. Oldfield, W.H. Sutton, Crevice Corrosion of Stainless Steels, Br. Corros. J. 13 (1978)   13–22. http://scholar.google.com/scholar?hl=en&btnG=Search&q=intitle:Crevice+Corrosion+of+Stainless+steel#4.

[48]   L. Jinlong, L. Tongxiang, D. Limin, W. Chen, Influence of sensitization on microstructure and passive property of AISI 2205 duplex stainless steel, Corros. Sci. 104 (2016) 144–151. doi:10.1016/j.corsci.2015.12.005.

[49]   T. Amadou, H. Sidhom, C. Braham, Double loop electrochemical potentiokinetic reactivation test optimization in checking of duplex stainless steel intergranular corrosion susceptibility, Metall. Mater. Trans. A. 35 (2004) 3499–3513. doi:10.1007/s11661-004-0187-4.

[50]   a. Cook, N. Stevens, J. Duff, a. Mshelia, T.-S. Leung, S. Lyon, J. Marrow, W. Ganther, I. Cole, Atmospheric-Induced Stress Corrosion Cracking of austenitic stainless steels under limited chloride supply, 18th Int. Corros. Congr. 2011. 2 (2011) 1438–1449.

[51]   D. van Rooyen, Stress Corrosion Cracking, J. Electrochem. Soc. 107 (1960) 715. doi:10.1149/1.2427815.

[52]   D.R. Johns, K. Shemwell, The crevice corrosion and stress corrosion cracking resistance of austenitic and duplex stainless steel fasteners, Corros. Sci. 39 (1997) 473–481. doi:10.1016/S0010-938X(96)00126-6.

[53]   K. Sieradzki, R.C. Newman, Stress-corrosion cracking, J. Phys. Chem. Solids. 48 (1987) 1101–1113. doi:10.1016/0022-3697(87)90120-X.

[54]   D. a. Vermilyea, A Theory for the Propagation of Stress Corrosion Cracks in Metals, J. Electrochem. Soc. 119 (1972) 405. doi:10.1149/1.2404217.

[55]   H. Hänninen, Selective Dissolution (Dealloying) - Vacancy Creep Mechanism, in: J. Petit, P.M. Scott (Eds.), Compr. Struct. Integr., Elsevier, Oxford, UK, 2003: p. 15.

[56]   P. Aaltonen, T. Saario, J. Piippo, S. Tahtinen, Vacancy-Creep Model for EAC of Metallic Materials in High Temperature Water, in: NACE Int. Annu. Conf. Expo., 1996: pp. 81.1-81.12.

[57]   J.R. Galvele, A stress corrosion cracking mechanism based on surface mobility, Corros. Sci. 27 (1987) 1–33. doi:10.1016/0010-938X(87)90117-X.

[58]   S.P. Lynch, Mechanistics and fractographic aspects of stress-corrosion cracking (SCC), in: V.S. Raja, T. Shoji (Eds.), Stress Corros. Crack. Theory Pract., Woodhead Publishing Limited, 2011: pp. 3–89. doi:10.1149/1.2427815.

[59]   W. Dietzel, P. Bala Srinivasan, A. Atrens, Testing and evaluation methods for stress

corrosion cracking (SCC) in metals, in: Stress Corros. Crack., Woodhead Publishing Limited, 2011: pp. 133–166. doi:10.1149/1.2427815.

[60]   S.P. Lynch, Hydrogen embrittlement (HE) phenomena and mechanisms, in: Stress Corros. Crack., 2011: pp. 91–130.

[61]   S.P. Lynch, Progress towards understanding mehcanisms of hydrogen embrittlement and stress corrosion cracking, (2007) 1–55.

[62]   S. Lynch, Hydrogen embrittlement phenomena and mechanisms, Corros. Rev. 30 (2012) 105–123. doi:10.1515/corrrev-2012-0502.

[63]   D.H. Kang, H.W. Lee, Study of the correlation between pitting corrosion and the component ratio of the dual phase in duplex stainless steel welds, Corros. Sci. 74 (2013) 396–407. doi:10.1016/j.corsci.2013.04.033.

[64]   Z. Zhang, H. Jing, L. Xu, Y. Han, L. Zhao, C. Zhou, Effects of nitrogen in shielding gas on microstructure evolution and localized corrosion behavior of duplex stainless steel welding joint, Appl. Surf. Sci. 404 (2017) 110–128. doi:10.1016/j.apsusc.2017.01.252.

[65]   N. Llorca-Isern, H. López-Luque, I. López-Jiménez, M.V. Biezma, Identification of sigma and chi phases in duplex stainless steels, Mater. Charact. 112 (2016) 20–29. doi:10.1016/j.matchar.2015.12.004.

[66]   H.M. Ezuber, a. El-Houd, F. El-Shawesh, Effects of sigma phase precipitation on seawater pitting of duplex stainless steel, Desalination. 207 (2007) 268–275. doi:10.1016/j.desal.2006.05.021.

[67]   R.A. Cottis, R.C. Newman, Stress Corrosion Cracking Resistance of Duplex Stainless Steels, Health and Safety Executive - Offshore Technology Report, 1993.

[68]   R. Li, M.G.S. Ferreira, The thermodynamic conditions for hydrogen generation inside a stress corrosion crack, Corros. Sci. 38 (1996) 317–327. doi:10.1016/0010-938X(96)00130-8.

[69]   W.T. Tsai, J.R. Chen, Galvanic corrosion between the constituent phases in duplex stainless steel, Corros. Sci. 49 (2007) 3659–3668. doi:10.1016/j.corsci.2007.03.035.

[70]   X. Cheng, Y. Wang, X. Li, C. Dong, Interaction between austein-ferrite phases on passive performance of 2205 duplex stainless steel, J. Mater. Sci. Technol. 34 (2018) 2140–2148. doi:10.1016/j.jmst.2018.02.020.

[71]   X. Cheng, Y. Wang, C. Dong, X. Li, The beneficial galvanic effect of the constituent phases in 2205 duplex stainless steel on the passive films formed in a 3.5% NaCl solution, Corros. Sci. 134 (2018) 122–130. doi:10.1016/j.corsci.2018.02.033.

[72]   A. Turnbull, R.B. Hutchings, Analysis of hydrogen atom transport in a two-phase alloy, Mater. Sci. Eng. A. 177 (1994) 161–171. doi:10.1016/0921-5093(94)90488-X.

[73]   R. Silverstein, O. Sobol, T. Boellinghaus, W. Unger, D. Eliezer, Hydrogen behavior in SAF 2205 duplex stainless steel, J. Alloys Compd. 695 (2017) 2689–2695. doi:10.1016/j.jallcom.2016.11.184.

[74]   J. Yao, J.R. Cahoon, Experimental studies of grain boundary diffusion of hydrogen in metals, Acta Metall. Mater. 39 (1991) 119–126. doi:10.1016/0956-7151(91)90333-V.

[75]   J. He, X. Tang, N. Chen, Diffusion of Hydrogen in (alpha + gamma) Duplex Stainless Steel, (n.d.).

[76]   R.B. Hutchings, a Turnbull, a T. May, Measurement of Hydrogen Transport in a Duplex Stainless Steel, Scr. Metall. Mater. 25 (1991) 2657–2662.

[77]   R. Kaçar, Effect of solidification mode and morphology of microstructure on the

hydrogen content of duplex stainless steel weld metal, Mater. Des. 25 (2004) 1–9. doi:10.1016/S0261-3069(03)00169-9.

[78]   S.-L. Chou, W.-T. Tsai, Effect of grain size on the hydrogen-assisted cracking in duplex stainless steels, Mater. Sci. Eng. A. 270 (1999) 219–224. doi:10.1016/S0921-5093(99)00174-4.

[79]   K. Toshio, Role of Sigma Phase on Hydrogen Embrittlement of Super Duplex, Trans. JWRI. 34 (2005) 63–68.

[80]   A. Bahrami, P. Woollin, Hydrogen Induced Stress Cracking of Duplex Stainless Steel Subsea Components, 112 (2010) 1–10.

[81]   P. Woollin, W. Murphy, Hydrogen embrittlement stress corrosion cracking of superduplex stainless steel, in: 2001.

[82]   M.J. Wozniak, a. Glowacka, J. a. Kozubowski, Magnetic properties of austeno-ferritic stainless steel after cathodic hydrogen charging, J. Alloys Compd. 404–406 (2005) 626–629. doi:10.1016/j.jallcom.2005.01.123.

[83]   T. Zakroczymski, a. Glowacka, W. Swiatnicki, Effect of hydrogen concentration on the embrittlement of a duplex stainless steel, Corros. Sci. 47 (2005) 1403–1414. doi:10.1016/j.corsci.2004.07.036.

[84]   A. Barnoush, M. Zamanzade, H. Vehoff, Direct observation of hydrogen-enhanced plasticity in super duplex stainless steel by means of in situ electrochemical methods, Scr. Mater. 62 (2010) 242–245. doi:10.1016/j.scriptamat.2009.11.007.

[85]   a. Głowacka, M.J. Woźniak, G. Nolze, W. a. Świątnicki, Hydrogen Induced Phase Transformations in Austenitic-Ferritic Steel, Solid State Phenom. 112 (2006) 133–140. doi:10.4028/www.scientific.net/SSP.112.133.

[86] S.X. Mao, M. Li, Mechanics and thermodynamics on the stress and hydrogen interaction in crack tip stress corrosion : Experiment and theory, J. Mech. Phys. Solids. 46 (1998) 1125–1137. doi:10.1016/S0022-5096(97)00054-9.

[87] L.J. Qiao, J.L. Luo, X. Mao, Hydrogen Evolution and Enrichment Around Stress Corrosion Crack Tips of Pipeline Steels in Dilute Bicarbonate Solution, Corrosion. 54 (1998) 115–120. doi:10.5006/1.3284834.

[88] B. Gu, J. Luo, X. Mao, Hydrogen-facilitated anodic dissolution-type stress corrosion cracking of pipeline steels in near-neutral pH solution, Corrosion. 55 (1999) 96–106. doi:10.5006/1.3283971.

[89] M.Z. Yang, J.L. Luo, Q. Yang, L.J. Qiao, Z.Q. Qin, P.R. Norton, Effects of hydrogen on semiconductivity of passive films and corrosion behavior of 310 stainless steel, J. Electrochem. Soc. 146 (1999) 2107–2112. doi:Doi 10.1149/1.1391899.

[90] Q. Yang, J.L. Luo, Martensite transformation and surface cracking of hydrogen charged and outgassed type 304 stainless steel, Mater. Sci. Eng. A. 288 (2000) 75–83. doi:10.1016/S0921-5093(00)00833-9.

[91] H.K. Birnbaum, P. Sofronis, Hydrogen-enhanced localized plasticity—a mechanism for hydrogen-related fracture, Mater. Sci. Eng. A. 176 (1994) 191–202. doi:10.1016/0921-5093(94)90975-X.

[92] A. Barnoush, H. Vehoff, Recent developments in the study of hydrogen embrittlement: Hydrogen effect on dislocation nucleation, Acta Mater. 58 (2010) 5274–5285. doi:10.1016/j.actamat.2010.05.057.

[93] P. Sathiya, S. Aravindan, R. Soundararajan, a. Noorul Haq, Effect of shielding gases on mechanical and metallurgical properties of duplex stainless-steel welds, J. Mater. Sci. 44 (2008) 114–121. doi:10.1007/s10853-008-3098-8.

[94]   A. Gtaw, 3 Chemical Reactions in Welding, 2003.

[95]   C.S. Wu, M. Ushio, M. Tanaka, Analysis of the TIG welding arc behavior, Comput. Mater. Sci. 7 (1997) 308–314. doi:10.1016/S0927-0256(96)00048-1.

[96]   E.M. Westin, M.M. Johansson, L. a. Bylund, R.F. a Pettersson, Effect on microstructure and properties of super duplex stainless steel welds when using backing gas containing nitrogen and hydrogen, Weld. World. 58 (2014) 347–354. doi:10.1007/s40194-014-0120-4.

[97]   R.N. Gunn, Welding processes, in: Duplex Stainl. Steels, Woodhead Publishing Limited, Abington, England, 1997: pp. 133–145. doi:10.1533/9781845698775.133.

[98]   J. Verma, R.V. Taiwade, Effect of welding processes and conditions on the microstructure, mechanical properties and corrosion resistance of duplex stainless steel weldments—A review, J. Manuf. Process. 25 (2017) 134–152. doi:10.1016/j.jmapro.2016.11.003.

[99]   R.-I. Hsieh, H.-Y. Liou, Y.-T. Pan, Effects of Cooling Time and Alloying Elements on the Microstructure of the Gleeble-Simulated Heat-Affected Zone of 22% Cr Duplex Stainless Steels, J. Mater. Eng. Perform. 10 (2001) 526–536. doi:10.1361/105994901770344665.

[100] H.Y. Liou, R.I. Hsieh, W.T. Tsai, Microstructure and pitting corrosion in simulated heat-affected zones of duplex stainless steels, Mater. Chem. Phys. 74 (2002) 33–42. doi:10.1016/S0254-0584(01)00409-6.

[101] Y. Yang, B. Yan, J. Li, J. Wang, The effect of large heat input on the microstructure and corrosion behaviour of simulated heat affected zone in 2205 duplex stainless steel, Corros. Sci. 53 (2011) 3756–3763. doi:10.1016/j.corsci.2011.07.022.

[102] G.W. Fan, J. Liu, P.D. Han, G.J. Qiao, Hot ductility and microstructure in casted 2205

duplex stainless steels, Mater. Sci. Eng. A. 515 (2009) 108–112. doi:10.1016/j.msea.2009.02.022.

[103] J.M. Cabrera, A. Mateo, L. Llanes, J.M. Prado, M. Anglada, Hot deformation of duplex stainless steels, J. Mater. Process. Technol. 143–144 (2003) 321–325. doi:10.1016/S0924-0136(03)00434-5.

[104] H. Farnoush, A. Momeni, K. Dehghani, J.A. Mohandesi, H. Keshmiri, Hot deformation characteristics of 2205 duplex stainless steel based on the behavior of constituent phases, Mater. Des. 31 (2010) 220–226. doi:10.1016/j.matdes.2009.06.028.

[105] R.D. Doherty, D. a. Hughes, F.J. Humphreys, J.J. Jonas, D. Juul Jensen, M.E. Kassner, W.E. King, T.R. McNelley, H.J. McQueen, a. D. Rollett, Current issues in recrystallization: A review, Mater. Today. 1 (1998) 14–15. doi:10.1016/S1369-7021(98)80046-1.

[106] W. Reick, M. Pohl, A.F. Padilha, Recrystallization-Transformation Combined Reactions during Annealing of a Cold Rolled Ferritic-Austenitic Duplex Stainless Steel., ISIJ Int. 38 (1998) 567–571. doi:10.2355/isijinternational.38.567.

[107] A. Piñol-Juez, A. Iza-Mendia, I. Gutiérrez, δ/γ Interface bondary sliding as a mechanism for strain accommodation during hot deformation in a duplex stainless steel, Metall. Mater. Trans. A. 31 (2000) 1671–1677. doi:10.1007/s11661-000-0177-0.

[108] A. V. Crewe, D.N. Eggenberger, J. Wall, L.M. Welter, Electron gun using a field emission source, Rev. Sci. Instrum. 39 (1968) 576–583. doi:10.1063/1.1683435.

[109] D.A. Moncrieff, P.R. Barker, Secondary electron emission in the scanning electron microscope, Scanning. 1 (1978) 195–197. doi:10.1002/sca.4950010307.

[110] P.J. Goodhew, J. Humphreys, z Ps io le Pf r, (n.d.).

[111] Y. Yamamoto, H. Morita, H. Yamada, H. Takahashi, M. Takakura, N. Kikuchi, T. Nokuo, N. Erdman, The Study of "Window-less" EDS Detector With Low Voltage FE-SEM, Microsc. Microanal. 22 (2016) 640–641. doi:10.1017/s1431927616004050.

[112] Noran, Energy-Dispersive X-ray Microanalysis, Noran Instruments. (1999) 68. doi:10.1007/BF01567579.

[113] T. Maitland, S. Sitzman, EBSD technique and materials characterization examples.pdf, Scanning Microsc. Nanotechnology. Tech. Appl. (2007) 41–76.

[114] T. Maitland, S. Sitzman, EBSD technique and materials characterization examples.pdf-Notes, Scanning Microsc. Nanotechnology. Tech. Appl. (2007) 41–76. doi:0387396209.

[115] T.B. Britton, J. Jiang, Y. Guo, A. Vilalta-Clemente, D. Wallis, L.N. Hansen, A. Winkelmann, A.J. Wilkinson, Tutorial: Crystal orientations and EBSD - Or which way is up?, Mater. Charact. 117 (2016) 113–126. doi:10.1016/j.matchar.2016.04.008.

[116] H.H. Strehblow, C.M. Melliar-Smith, W.M. Augustyniak, Examination of Aluminum-Copper Films during the Galvanostatic Formation of Anodic Oxide, J. Electrochem. Soc. 125 (1978) 915–919.

[117] L.H. Guilherme, A.V. Benedetti, C.S. Fugivara, A Portable Electrochemical Microcell for Weld Inspection of Duplex Stainless Steel Tanks, Corrosion. 75 (2018) 340–348. doi:10.5006/3004.

[118] M.F. Hurley, C.M. Efaw, P.H. Davis, J.R. Croteau, E. Graugnard, N. Birbilis, Volta Potentials Measured by Scanning Kelvin Probe Force Microscopy as Relevant to Corrosion of Magnesium Alloys, Corrosion. 71 (2015) 160–170.

[119] M. Rohwerder, F. Turcu, High-resolution Kelvin probe microscopy in corrosion science: Scanning Kelvin probe force microscopy (SKPFM) versus classical scanning

Kelvin probe (SKP), Electrochim. Acta. 53 (2007) 290–299. doi:10.1016/j.electacta.2007.03.016.

[120] S. Trasatti, Work function, electronegativity, and electrochemical behaviour of metals. II. Potentials of zero charge and "electrochemical" work functions, J. Electroanal. Chem. 33 (1971) 351–378. doi:10.1016/S0022-0728(71)80123-7.

[121] C. Örnek, Performance Characterisation of Duplex Stainless Steel in Nuclear Waste Storage Environment, University of Manchester, 2015.

[122] A.B. Cook, Z. Barrett, S.B. Lyon, H.N. McMurray, J. Walton, G. Williams, Calibration of the scanning Kelvin probe force microscope under controlled environmental conditions, Electrochim. Acta. 66 (2012) 100–105. doi:10.1016/j.electacta.2012.01.054.

[123] C. Örnek, D.L. Engelberg, Correlative EBSD and SKPFM characterisation of microstructure development to assist determination of corrosion propensity in grade 2205 duplex stainless steel, J. Mater. Sci. (2015). doi:10.1007/s10853-015-9501-3.

[124] K.B. Small, D. a. Englehart, T. a. Christman, Guide to etching specialty alloys, Adv. Mater. Process. 166 (2008) 32–37.

[125] ASTM, A262 Standard Practices for Detecting Susceptibility to Intergranular Attack in Austenitic., ASTM. (2014) 1–17. doi:10.1520/A0262-13.

[126] ASTM, A923 Standard Test Methods for Detecting Detrimental Intermetallic Phase in Duplex Austenitic / Ferritic Stainless Steels, (2014) 1–9. doi:10.1520/A0923-14.1.6.

[127] E.-05 ASTM, Standard Test Method for Determining Volume Fraction by Sistematic Manual Point Count, 64 (1996) 3–5. doi:10.1520/C1543-10a.2.

[128] W.S. Rasband, ImageJ, (n.d.).

[129] M. Campos, A. Bautista, D. Cáceres, J. Abenojar, J.M. Torralba, Study of the interfaces between austenite and ferrite grains in P/M duplex stainless steels, J. Eur. Ceram. Soc. 23 (2003) 2813–2819. doi:10.1016/S0955-2219(03)00293-0.

[130] L.Q. Guo, M.C. Lin, L.J. Qiao, A. a. Volinsky, Ferrite and austenite phase identification in duplex stainless steel using SPM techniques, Appl. Surf. Sci. 287 (2013) 499–501. doi:10.1016/j.apsusc.2013.09.041.

[131] K.R. Gadelrab, G. Li, M. Chiesa, T. Souier, Local characterization of austenite and ferrite phases in duplex stainless steel using MFM and nanoindentation, J. Mater. Res. 27 (2012) 1573–1579. doi:10.1557/jmr.2012.99.

[132] P.J. Bouchard, Validated residual stress profiles for fracture assessments of stainless steel pipe girth welds, Int. J. Press. Vessel. Pip. 84 (2007) 195–222. doi:10.1016/j.ijpvp.2006.10.006.

[133] M. Fitzpatrick, A. Fry, P. Holdway, F. Kandil, J. Shackleton, L. Suominen, Determination of Residual Stresses by X-ray Diffraction - Issue 2, Natl. Phys. Lab. (2005) 74. doi:10.1007/s00028-005-0194-y.

[134] J. Johansson, M. Odén, Load sharing between austenite and ferrite in a duplex stainless steel during cyclic loading, Metall. Mater. Trans. A Phys. Metall. Mater. Sci. 31 (2000) 1557–1570. doi:10.1007/s11661-000-0166-3.

[135] N. Mary, V. Vignal *, R. Oltra, L. Coudreuse, Finite-element and XRD methods for the determination of the residual surface stress field and the elastic–plastic behaviour of duplex steels, Philos. Mag. 85 (2005) 1227–1242. doi:10.1080/14786430412331333329.

[136] E. Owczarek, T. Zakroczymski, Hydrogen transport in a duplex stainless steel, Acta

190

Mater. 48 (2000) 3059–3070. doi:10.1016/S1359-6454(00)00122-1.

[137] S.-L. Chou, W.-T. Tsai, Hydrogen embrittlement of duplex stainless steel in concentrated sodium chloride solution, Mater. Chem. Phys. 60 (1999) 137–142. doi:10.1016/S0254-0584(99)00077-2.

8 Appendix

8.1 Conference Paper -Assessment of Microstructure Susceptibility to Hydrogen Embrittlement of TIG Welded Grade 2205 Duplex Stainless Steel (Eurocorr 2016)

P. Reccagni[a], C. Örnek[a], Q. Lu[b], M. F. Gittos[b], D.L. Engelberg[a]

[a]Corrosion and Protection Centre, School of Materials, The University of Manchester, Sackville Street, Manchester, M13 9PL, United Kingdom

[b]TWI Ltd, Granta Park, Great Abington, Cambridge CB21 6AL, United Kingdom

Abstract: The effects of hydrogen ingress on changes in the near-surface microstructure of a grade 2205 TIG weld have been investigated. Microstructural changes have been observed after cathodic hydrogen charging using SEM imaging, in both the parent material and the weld region. The austenite showed the development of slip bands, whereas regions of discrete microstructure contrast were observed in the ferrite. Extended cathodic charging of strained grade 2205 samples seemed to promote the development of microstructure features in the ferrite resulting in discrete microstructure protrusions.

These protrusions also seemed to be associated with local crack initiation sites in the weld region.

8.2 INTRODUCTION

Duplex stainless steel (DSS) grade 2205 are widely used in the energy sector because of their high strength and excellent corrosion resistance. Their outstanding resistance to Environment-Assisted Cracking (EAC) is a result of the dual phase microstructure, typically containing a balanced ratio of austenite (γ) and ferrite (δ). In particular, their resistance to Hydrogen Embrittlement (HE) makes them a viable choice for subsea application, where cathodic protection systems (CP) are often applied. Improper welding can alter the phase balance and produce tertiary phases and precipitates, for example, sigma-, chi-phase, and chromium nitrides (Cr_2N, CrN). The microstructure morphology in a weld also shows great differences compared to the parent material as a result of the thermal history.

Hydrogen diffusion in DSS is complicated, due to apparent properties of the dual phase microstructure. The ferritic phase shows high diffusion rate and low solubility, whereas diffusion in austenite is slower and the solubility greater[76,136]. The phase boundaries act either as fast diffusion pathways or trapping sites for hydrogen, with the latter due to their high binding energy [72]. As a result, the hydrogen uptake of DSS is dependent not only on the phase balance but also on the microstructure morphology.

The objective of this work is to investigate the effects of hydrogen on microstructure behaviour, aiming to identify whether microstructural changes can give information on the onset of hydrogen induced cracking (HIC) in DSS welds. The effect of hydrogen cathodic charging on a TIG welded grade 2205 DSS will be investigated. Miniature-tensile sample machined from a pipe girth-weld have been used to expose the welded microstructure to the cathodic charging environment, with the aim to observe differences in microstructure performance.

194

8.3 EXPERIMENTAL

Two pipe sections (9.2 mm thickness, 406 mm diameter) have been joined with a TIG multi-pass girth weld. The parent material and the filler material used for welding were both DSS grade 2205 with pure Argon used as shielding and backing gas. Miniature tensile samples containing the parent material, the heat affected zone (HAZ), and the weld have been EDM machined across the weld, shown in Figure 76.
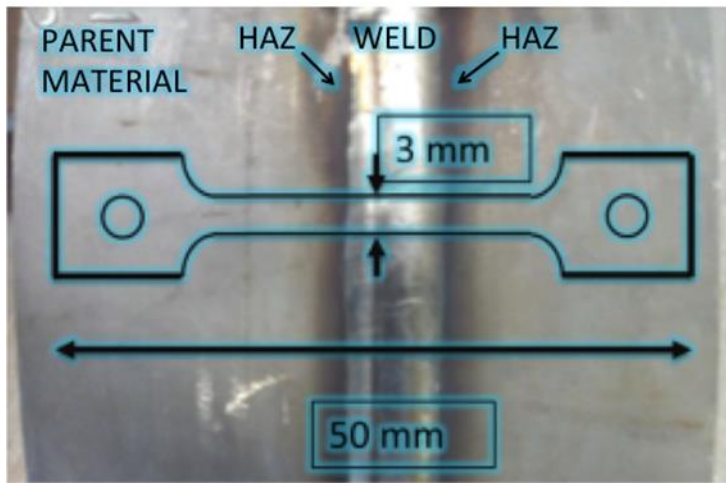

Figure 76 - Sketch of miniature tensile samples machined from the welded pipe.

The tensile sample surface was prepared by grinding to 4000 grit, followed by a diamond polish to 0.25 µm finish, and a fine polishing with colloidal silica. The microstructure was characterized in a FEI Quanta650 and FEI Quanta200 FEG-SEM (Field Emission Gun - Scanning Electron Microscope).

Hydrogen electrolytic charging of a miniature tensile sample has been carried out to introduce hydrogen into the near-surface microstructure. A current density of 20 mA/cm2, generated with an ACM Instruments galvanostat in a 0.1M H2SO4 electrolyte at room temperature was used for all experiments. The cathodic charging was paused after 2 and 6 hrs, the sample removed form the charging electrolyte and the surface imaged in the FEI Quanta 200 SEM. Phase identification was based on chemical element partitioning

measured with Energy-Dispersive X-ray (EDX) spectroscopy. Ferrite contained more ferrite forming elements (Cr, Mo), whereas austenite contained more austenite formers (Ni, Mn, N).

The effect of applied strain during charging of a tensile sample was also investigated, using a screw-loaded direct tension rig, with the total strain estimated by means of measuring the elongation of the gauge via optical micrographs acquired before and after tightening the screw. A total strain of 4% was applied. The gauge was then exposed to cathodic charging for 24 hrs using the same parameters as listed above. The sample was then unloaded, removed from the rig, and the surface imaged in the FEI Quanta 650 SEM.

8.4 RESULTS

The development of the grade 2205 parent microstructure response to the interrupted charging cycle after 2 and 6 hrs of cathodic exposure are shown in Figure 77. In the austenite, the hydrogen uptake has promoted the formation of slip bands. In the ferrite, needle-like features with a white contrast started to appear after 2hrs, which became more apparent after 6 hrs of charging. The same trend was also observed in the austenite regions, with more distinctive slip band contrast visible after 6 hrs of charging. A qualitative observation of the surface suggests that the amount of both features increased with hydrogen charging time, hence with the hydrogen content in the microstructure.
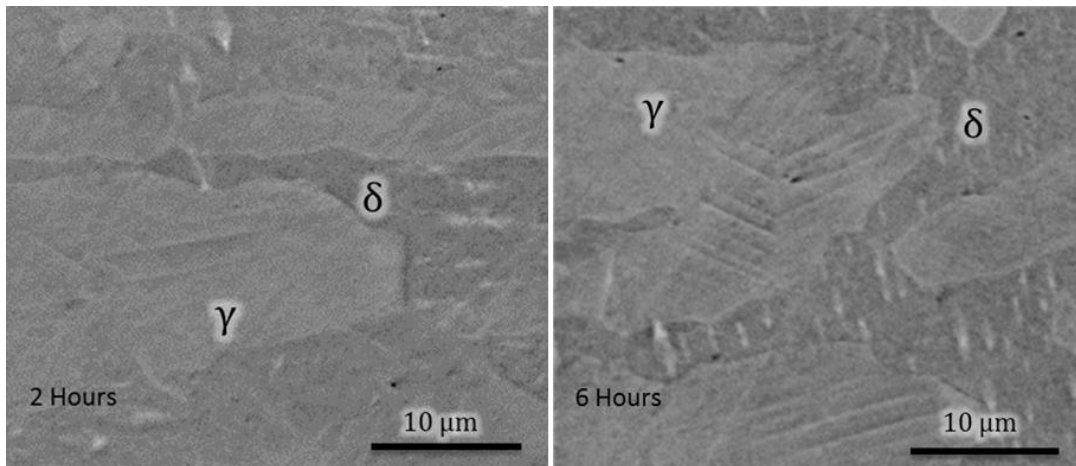
Figure 77 - Hydrogen induced changes in the near surface microstructure (left) after 2 hours and (right) after 6 hours of cathodic charging.

The effect of applied strain and longer exposure to cathodic hydrogen charging resulted in the formation of discrete microstructural changes, both in the parent material and inside the weld as shown in Figure 78. The applied strain promoted the development of local protrusions on the ferrite, which seemed to follow some sort of crystallographic relationships with ferrite grain orientations. These features were observed both in the parent material and in the weld. Interestingly, in the weld region the first signs of local decohesion located adjacent to these features were observed.

The ability of hydrogen to reduce the shear stress required for the activation of slip systems[84], in conjunction with 4% plastic strain applied, resulted in the presence of slip bands in the austenite. This effect was seen both in the weld and in the parent material. However, there was no sign of cracking or decohesion in the austenite.
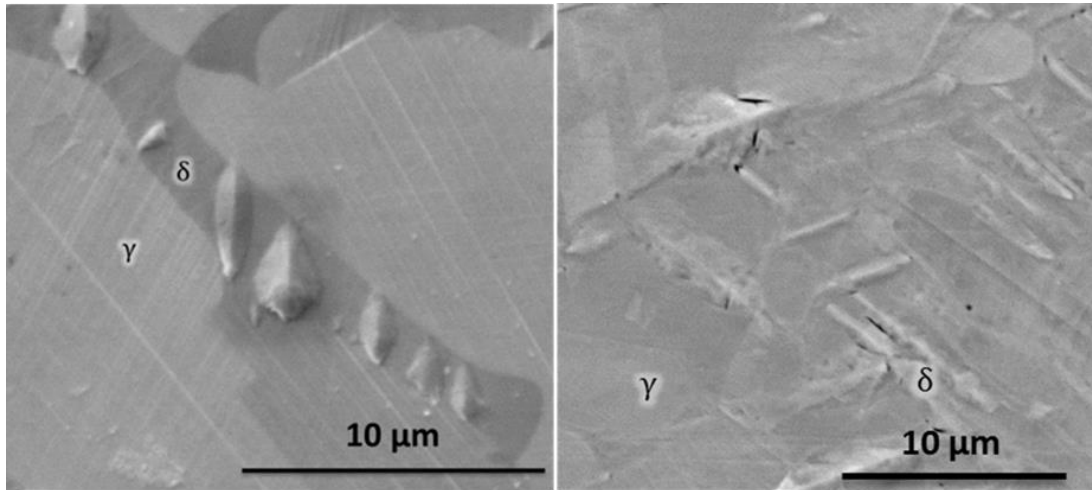
197

Figure 78 - Microstructural changes after 24 hours hydrogen charging under 4% applied strain. Parent material (left) and weld region (right).

8.5 DISCUSSION

Hydrogen induced microstructural changes have been reported in the literature by several groups [84,85,137]In austenite, the activation of new slip systems and the transformation in martensite have been described. In ferrite, the formation of twins has been suggested as a possible explanation for the needle-like microstructure relieves observed [85] However, the role of these changes in crack nucleation and propagation is not clear. HIC is known to affect mainly the ferrite [137], where hydrogen is less soluble.

Microstructural changes observed in the ferrite seem to promote local crack nucleation events. The distribution of the observed protrusions - see Figure 79 - suggests a strong crystallographic relationship with the parent ferrite grains. This relationship is far more evident inside the weld, where the ferrite grains are larger, as shown in Figure 4. The applied strain and longer charging interval resulted in larger protrusions. The sample without applied strain, shown in Figure 2, indicates that for the initial formation of these features the presence of applied strain is not necessary. Microstructural changes in the austenite, where the hydrogen solubility is higher, showed the activation of slip systems in

samples strained and without applied strain. However, it was not possible to identify the formation of any martensite lathe under the conditions used in this work.

The reported work is part of a larger effort to identify the role of duplex stainless steel microstructure in environmentally assisted cracking (EAC) with exposure to extreme environments.
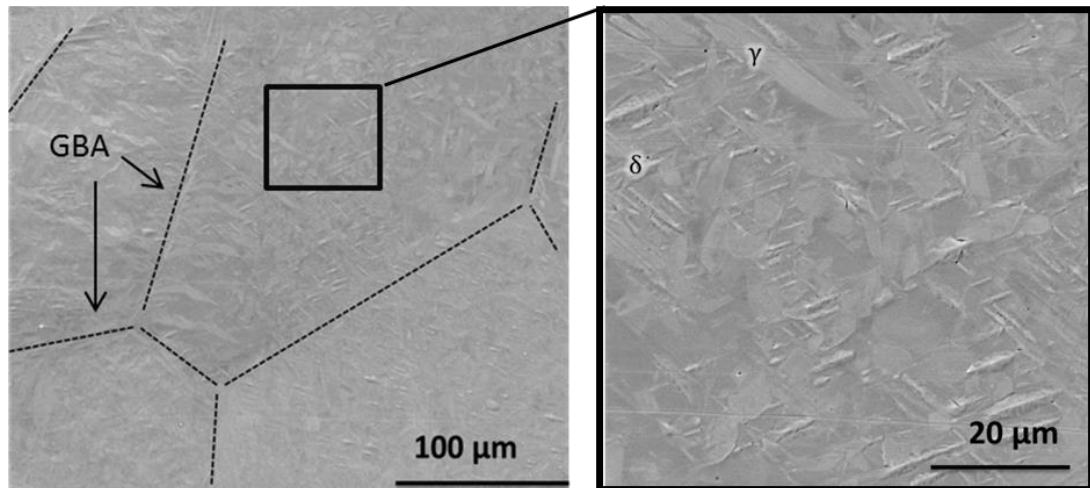

Figure 79 - Protrusions observed in the ferrite inside the weld. The network of grain boundary austenite (GBA) delimiting the ferritic grain is shown in the picture on the left. On the right, higher magnification image of a ferrite grain (square area in left image), highlighting the presence of a crystallographic relationship of these protrusions

8.6 CONCLUSIONS

• Cathodic hydrogen charging of DSS 2205 induced near-surface microstructure changes in both austenite and ferrite, with austenite resulting in the formation of slip bands, whereas the ferrite showed the formation of discrete protrusions.

• The application of strain and longer cathodic charging exposure promoted the development of discrete microstructure protrusions in the ferrite, indicating a crystallographic relationship to parent grain orientations, in both the weld region and parent material.

- In the weld, cracks associated with these features have been found, suggesting local decohesion reactions associated with these protrusions.